EPFL

Thèse n° 8221

Three-dimensional electrodes for dielectrophoretic applications

Présentée le 24 avril 2020

à la Faculté des sciences et techniques de l'ingénieur
Chaire Swiss-up en ingénierie - Laboratoire d'électronique pour les sciences du vivant
Programme doctoral en microsystèmes et microélectronique

pour l'obtention du grade de Docteur ès Sciences

par

Kevin KEIM

Acceptée sur proposition du jury

Dr G. Boero, président du jury
Prof. C. Guiducci, directrice de thèse
Prof. P. Dittrich, rapporteuse
Prof. N. Swami, rapporteur
Prof. Ph. Renaud, rapporteur

École polytechnique fédérale de Lausanne

2020

Für meine Mutter…

Acknowledgements

Creating a PhD is not an individual experience; rather it is very much function of the environment and the people which share the journey. EPFL has been a great place to work and learn, an inspiring environment with great possibilities and the resources for world leading research. I am grateful to have had the chance to be there.

First of all, I would like to express my sincere gratitude to my professor Carlotta Guiducci for the continuous support during my PhD, for her patience and motivation. She was always there when I needed advice, but also gave me the freedom to explore, to learn and to follow my own ideas. In addition, she gave me opportunities to grow even further through the management and exploration of many other projects.

Beside my professor, I would like to thank all the members of my thesis committee: Prof. Giovanni Boero and Prof. Philippe Renaud from EPFL, as well as the external experts Prof. Petra Dittrich from ETH-Zurich and Prof. Nathan Swami from the University of Virginia for their insightful feedback on the thesis and the discussion during the examination.

During my research work, we received funding from the Swiss National Science Foundation for the investigation of of arrayed electrorotation microcages, for which I am very thankful. A huge thank you as well to SCITAS, where we run some of the simulations and CMi where we fabricated our microfluidic chips. I really learned a lot from the great staff at CMi and they helped me whenever I had fabrication issues.

My sincere thanks also goes to the Tegenfeldt group from the University of Lund, Sweden, with whom the collaboration was very fruitful. I really enjoyed working with the group and I would like to thank Prof. Jonas O. Tegenfeldt, Dr. Jason P. Beech, Dr. Bao Dang Ho and Oskar Ström for their hospitality and discussion during my stays at Nano Lund.

I also would like to thank Prof. Mehmet Toner for the opportunity to join his laboratory at the Massachussets General Hospital and Harvard Medical School for three months as a visiting PhD student. I am both really thankful to my home lab for making this possible and for the hospitality of the lab in Boston. Thanks also to Dr. Baris Mutlu for the fruitful every day work together and to all the lab members, which made the time very pleasant and full of learnings.

Very importantly, I would like to thank all the students, who I had the pleasure to train and supervise during my PhD. It was great to see, how you improved your scientific skills over the time of your projects. You made it possible to get the insights which are presented in this thesis and all of you worked very hard and contributed to this story. Thanks to Mathilde Roige, Antonio Gonçalves, Sebastian Emery, Paul Éry, Aurélien Delattre, David Urban, Mohammed Z. Rashed, Widad Labichi, Giovanni Cappai, Gloria Porro and Till Ryser, as well as to our lab

technician Lilia Salimova, who helped for some time with the experiments.
Thanks to all my colleagues, namely Dr. Samuel C. Kilchenmann, Dr. Enrica Rollo, Dr. Enrico Tenaglia, Dr. Pietro Maoddi, Dr. Marco Letizia, Saurabh Tomar, Pierre-Emmanuel Thiriet, Dr. Erick Garcia and Loulia Kassem for the collaboration and for the time spent together. It was a great time with you and I really enjoyed it. I am looking forward for further fruitful projects with you and for great scientific output in the future.
Monica Suarez, our administrative assistant supported me with so much outside of science, organizing several stays at conferences, purchasing equipment and many more. Thank you for that.
Last but not least, I am thankful to my family for supporting me. First, my mother, Helga Keim, who raised me and made me the person I am today. Thanks as well to my father Reinhold Keim and my sister Nicole Keim, who I could always talk to. A special thanks goes to my wife Agathe Keim, who I could always talk to about successes and failures and who always cheered me up and got me back on track.

Lausanne, 16 January 2020 K. K.

Abstract

This thesis reports the use of metal-coated three-dimensional SU-8 electrodes for dielectrophoretic bio sensing and particle manipulation applications. Placing free standing three-dimensional electrodes in microfluidic channels, electric fields can be applied homogeneously over the complete height of the device. Due to this, at any vertical position in the channel, an equal dielectrophoretic force is created. These electrodes have been used to parallelize individual single-cell analysis by the mean of electrorotation and to tune the sorting size of deterministic lateral displacement devices by adding dielectrophoretic forces.

Electrorotation uses rotating electric fields to make cells spin and determine their dielectric properties from their speed of rotation at different electric excitation frequencies. Using a double array of individual connected three-dimensional electrodes placed in a wide microfluidic channel, individual cells can be selectively trapped and released in single-cell dielectrophoretic micro cages and analyzed in parallel by electrorotation. The parallel analysis of cells in individual electrorotation cages is demonstrated for the first time and the membrane capacitance of Henrietta Lacks, human embryonic kidney 293, and human T lymphocytes are found in agreement with literature. The membrane capacitance of M17 neuroblastoma is investigated and found to be $7.49 \pm 0.39 mF/m^2$. Additionally, membrane capacitance changes within a human embryonic kidney 293 cell population are observed with the system based on an osmolarity study and the viability is assured by monitoring the membrane functionality using an erythrosin B dye. Failure of the membrane sealing function is observed in real-time by a shift of the electrorotation spectrum and a drop in the membrane capacitance.

Deterministic lateral displacement uses shifted rows of posts in a microfluidic labyrinth to sort particles based on their size. The principle uses the deterministic behavior of particles in the device, particles below a certain size move straight through the device, while larger particles are displaced to the side. Replacing the passive posts by three-dimensional electrodes allows the creation of local dielectrophoretic forces. Applying voltages of up to $15 V_{pp}$ dynamically reduces the sorting size of the device from $6 \mu m$ to $250 nm$, enabling a device tunable for a specific sorting size. Nanometer sized particles can be separated in within micrometer structures reducing the problem of clogging. Additionally, this device could enable sorting of equal sized nanometer particles based on their dielectric properties.

These two examples show the applicability of metal-coated three-dimensional SU-8 electrodes for dielectrophoretic applications. They first enable the design of new devices, which could not be realized previously, as shown by the electrorotation device, and second traditional passive structures can be replaced by electrodes, which can help to improve their performance

or enable new functionalities.

Key words:
three dimensional electrodes, dielectrophoresis, electrorotation, deterministic lateral displacement, microfluidics, single-cell manipulation, particle sorting

Zusammenfassung

Diese Doktorarbeit berichtet über die Verwendung von metall-beschichteten dreidimensionalen Elektroden aus SU-8 für dielekrotrophoretische Anwendungen im Bereich von Biosensoren und der Manipulation von Partikeln. Platziert man feistehenden dreidimenisonalen Elektroden in mikrofluidischen Kanälen, können homogene elektrische Felder über die komplette Höhe des Chips erreicht werden. Für dielektrophoretische Anwendungen hat das den Vorteil, dass die gleiche Kraft an jeder vertikalen Position im Kanal erzeugt wird. Diese Elektroden wurden benutzt, um individuelle Einzelzellen Analyse per Elektrorotation zu parallelisieren und um die Sortiergrösse von deterministischen lateral Verschiebungschips mittels dielektrophoretischen Kräften zu varieren.

Elektrorotation benutzt rotierende elektrische Felder um Zellen zum rotieren zu bringen und bestimmt ihre dielektrischen Eigenschaften anhanden ihrer Rotationsgeschwindigkeit unter verschiedenen elektrischen Anregefrequenzen. Mit zwei parallelen Reihen aus individuell verbundenen dreidimensionalen Elektroden in einem breiten mikrofluidischen Kanal können einzelne Zellen selektiv in dielektrophoretischen Mikrokäfigen gefangen und losgelassen werde und parallel per Elektrorotation analisiert werden. Die parallele Zellanalyse mit individuellen Elektrorotationskäfigen wird hier zum ersten mal demonstriert und die Membrankapazität von Henrietta Lacks, menschlichen embrionischen Nierenzellen und T-Lympohzyten sind in Übereinstimmung mit den Literaturwerten. Die Membrankapazität von M17 Neuroblastoma wird erforscht und wurde auf $7.49 \pm 0.39 mF/m^2$ bestimmt. Zusätzlich werden die Membrankapazitätsveränderungen von menschlichen embrionischen Nierenzellen mittels einer Osmolaritätsstudie untersucht und die Funktionsfähigkeit der Membrane wird mit dem Farbstoff Erythrosin überwacht. Das Versagen der Membran kann durch ein Verschieben des Elektrotationsspektrums und einer Reduktion der Membran Kapazität live beobachtet.

Deterministische laterale Verschiebungs Chips benutzen verschobene Pfostenreihen in einem Mikrofluidischen Chip, um Partikel nach Grösse zu sortieren. Das deterministische Verhalten von Partikeln in dem Kanal sorgt darfür, dass Partikel unter einer gewissen Grösse sich gerade durch den Kanal fliessen, während grössere Teilchen zur Seite driften. Ersetzt man die passiven Pfosten durch dreidimensionale Elektroden, können lokale dielekrophoretische Kräfte erzeugt werden. Das Anlegen von bis zu $15 V_{pp}$ kann dynamisch die Sortiergrösse von $6 \mu m$ auf $250 nm$ reduzieren, was das Gerät stimmbar für eine spezifische Teilchengrösse macht. Nanometer grosse Teilchen können innerhalb von Mikrometer grossen Strukturen sortiert werden, was das Problem des Verstopfens reduziert. Zusätzlich könnte das Gerät das Sortieren

von gleichgrossen Teilchen aufgrund ihrer dielektrischen Eigenschaften ermöglichen.
Diese zwei Beispiele zeigen die Anwendbarkeit von metall-beschichteten dreidimensionalen Elektroden für dielektrophoretische Anwendungen. Sie ermöglichen zum einen das Entwickeln von neuen Geräten, die zuvor nicht möglich waren, wie am Beispiel an den Elektrorotationsgeräten gezeigt wurde, und zum anderen dass traditionell nicht-elektrische Strukturen durch Elektroden ersetzt werden können und somit ihre Leistung gesteigert werden oder neue Funktionalitäten ermöglicht werden können.

Schlüsselwörter:
dreidimensionale Elektroden, Dielektrophorese, Elektrorotation, deterministische lateral Verschiebung, Mikrofluidik, Einzelzellenmanipulation, Teilchensortierung

Résumé

Cette thèse décrit l'utilisation d'électrodes tridimensionnelles en SU-8 recouvertes de métal pour la détection biologique et la manipulation de particules par diélectrophorèse. En positionnant ces électrodes dans les canaux d'une puce microfluidique, des champs électriques peuvent être appliqués de manière homogène sur toute la hauteur de la puce. Ainsi, quelque soit la position verticale dans le canal, la force diélectrophorétique créée est la même. Ces électrodes ont été utilisées pour permettre l'analyse individuelle de cellules en parallèle au moyen de la technologie d'électrorotation ainsi que pour trier des particules en fonction de leur taille en exploitant la méthode du déplacement latéral déterministique associée aux forces diélectrophorétiques.

L'électrorotation utilise des champs électriques tournants pour faire tourner les cellules et déterminer leurs propriétés diélectriques en analysant leur vitesse de rotation à différentes fréquences d'excitation. En utilisant une matrice d'électrodes tridimensionnelles individuellement connectées et placées dans un large canal microfluidique, des cellules peuvent être piégées de façon sélective et libérées individuellement dans des micro-cages diélectrophorétiques et analysées en parallèle par électrorotation. L'analyse parallèle de cellules dans des cages d'électrorotation individuelles est démontrée pour la première fois et les capacités obtenues pour les membranes cellulaires de cellules de ligne de Henrietta Lacks, de cellules embryonnaire rénales humaines 293 et de lymphocytes T humains sont en accord avec les résultats déjà publié dans la littérature. La valeur de la capacité membranaire du neuroblastome M17 est étudiée et est de $7.49 \pm 0.39 mF/m^2$. De plus, à l'aide d'un système d'étude de l'osmolarité, les variations de capacité de la membrane cellulaire au sein d'une population de cellules rénales embryonnaires humaines 293 sont observées et la viabilité est contrôlée par un suivi à l'aide du colorant érythrosine B. La perte d'étanchéité de la membrane cellulaire est visible en temps réel grâce à un décalage du spectre d'électrorotation et à une baisse de la capacité de la membrane.

La technique de déplacement latéral déterministe utilise des rangées décalées de pilier dans un labyrinthe microfluidique pour trier les particules en fonction de leur taille. Le principe repose sur l'utilisation du comportement déterministe des particules dans l'appareil, les particules dont la taille est inférieure à une certaine valeur passent directement à travers le canal microfluidique, tandis que les particules plus grosses sont isolées à la périphérie de la puce. Remplacer les piliers habituellement passifs, par des électrodes tridimensionnelles permet de créer de forces diélectrophorétiques locales. Appliquer de façon dynamique une tension pouvant aller jusqu'à $15 V_{pp}$ permet de varier la sensibilité de tri de notre plateforme

pour des particules présentant un diamètre de $6\mu m$ à $250nm$, ce qui permet d'avoir une plateforme réglable pour une taille de tri spécifique. Des particules de l'ordre du nanomètre peuvent ainsi être séparées à l'intérieur d'un canal présentant des structures avoisinant le micromètre, réduisant le risque de formation d'agrégats qui pourraient bloquer le canal. De plus, ce dispositif pourrait permettre de trier des particules nanométriques de taille égale en fonction de leurs propriétés diélectriques.
Ces deux exemples montrent l'applicabilité des électrodes tridimensionnelles en SU-8 pour des applications diélectrophorétiques. Ces électrodes permettent tout d'abord de concevoir de nouveaux dispositifs, qui ne pouvaient être conçus auparavant, comme le montre le dispositif d'électrorotation, et peuvent remplacer les structures passives traditionnelles, afin d'améliorer les performances de leurs plateformes ou à rendre possible de nouvelles fonctionnalités.
Mots clés :
électrodes tridimensionnelles, diélectrophorèse, électrorotation, déplacement latéral déterministique, microfluidique, manipulation unicellulaire, tri des particules

Contents

Acknowledgements **v**

Abstract (English/Français/Deutsch) **vii**

List of figures **xiv**

Introduction **1**

1 On-chip manipulation and analysis of bio particles **5**
1.1 Population sorting 6
1.1.1 Based on size 8
1.1.2 Based on deformability 10
1.1.3 Based on dielectric properties 12
1.1.4 Based on surface markers 13
1.1.5 Combined size- and dielectric property based sorting by alternating-current deterministic lateral displacement 14
1.2 Single-cell arraying 17
1.2.1 Dielectrophoretic trapping 19
1.3 Non destructive time-resolved single-cell analysis 21
1.3.1 Based on optical properties 22
1.3.2 Based on mechanical properties 22
1.3.3 Based on electrical properties 24
1.4 Fabrication of three-dimensional electrodes and their advantage for dielectrophoresis 27

2 Simulations of arrayed negative dielectrophoretic traps to optimize the trap size and experimental conditions **33**
2.1 Theoretical background 33
2.1.1 Dielectrophoresis 34
2.1.2 Models for the Clausius-Mossotti factor 35
2.1.3 Microfluidic drag force 37
2.2 Simulations of the DEP trapping 38

3 Single-cell electrokinetics-based trapping and analysis by electrorotation 51
3.1 Theoretical background on electrorotation 51
3.2 A parallelized electrorotation setup 53
3.2.1 Toward a parallelized electroroation setup 53
3.2.2 Parallel acquisition of electrorotation spectra using alternating trapping and rotating signals allows to analyze the membrane capacitance of cell lines in flow 57
3.2.3 Investigation of the effect of osmolarity on the membrane capacitance and real-time analysis of the membrane integrity 79

4 Sub micrometer particles sorting by combined electrokinetic and microfluidic methods 85
4.1 Theoretical background on deterministic lateral displacement 85
4.2 Experimental methods for deterministic lateral displacement 87
4.2.1 Deterministic lateral displacement setup 87
4.2.2 Deterministic lateral displacement measurement procedure 88
4.3 Three dimensional posts enable local dielectrophoretic forces in deterministic lateral displacement devices 90
4.3.1 The critical size is changed by the applied voltage 90
4.3.2 The traveling mode depends on the applied voltage and the applied pressure 92
4.3.3 Equation for the crossover voltage 93
4.3.4 Sharp edged electrodes for sorting of smaller particles 95

5 Summary, Conclusion and Outlook 99
5.1 Summary 99
5.2 Conclusion 100
5.3 Outlook 101
5.3.1 Using parallelized electrorotation to investigate protein deposition in Alzheimer's disease 101
5.3.2 Active DLD posts to separate exosoms based on their dielectric properties 102
5.3.3 Trapping cells in flow to ensure encapsulation of multiple cells in droplets 102

Bibliography 118

Curriculum Vitae 119

List of Figures

1.1 Within the last twenty years different technologies to sort populations have been developed, their throughput is noted on the y axis. Additionally, their nature of analysis is noted: electrical=blue, optical=red, hydrodynamic=green, acoustic=orange. Figure reproduced from [10] with permission from John Wiley and Sons. 7

1.2 Particles of different size are flowing through a microfluidic spiral. Their equilibrium position of the inertia lift and the dean drag force determines at which position they leave the channel between the center of the channel and the channel side wall. Based on this they can finally be directed in separated channels. Figure reproduced from [12] with permission from the Royal Society of Chemistry. 9

1.3 Field flow fractionation is based on a flow in a wide microfluidic channel featuring a parabolic flow profile, which is combined with a cross flow vector, leading to a separation of particles. (a) The schematic layout of the device. (b) Cross section of the channel with the relevant flows. Figure adapted from [18] with permission from The American Association for the Advancement of Science. . 10

1.4 Two high velocity microfluidic streams are colliding and deforming the cell in the center of the channel. (a) Conceptional sketch. (b) Image series of recorded experimental video. (c,d) The cell initial diameter and its calculated deformability can be plotted in a diagram. Figure adapted from [25] with permission from PNAS. 11

1.5 Using three dimensional electrodes (a) in an electrical impedance-based setup, activated and non activated human T lymphocytes can be identified by their electric impedance (b). Figure adapted from [34] with permission from Elsevier. 13

1.6 Applying a $5V_{pk}$ signal of a frequency of $10MHz$ at interdigitaded, castellated electrodes, viable and non-viable yeast cells can be separated. The viable yeast cells accumulate on the edges of the electrodes, while dead yeast cells accumulate on top and in between the electrodes. Figure adapted from [37] with permission from Elsevier. 14

1.7 SEM micrograph of the nanosized DLD gaps. Exosoms can be sorted by size in this device. Figure reproduced from [44] with permission of Springer Nature. . 15

1.8 (a) The working principle of the virtual DLD posts is that the posts are replaced by electrodes which create a repulsive DEP signal. (b) Underlying interconnections for the electrodes are insulated with Si_3N_4 and they are opened at specific positions, where the virtual posts are created. Figure adapted from [46] with permission of the Royal Society of Chemistry. 16
1.9 Layout of a DLD device combined with DEP applying a voltage from the inlets to the outlet. Figure reproduced from [47] with permission from the Royal Society of Chemistry. 17
1.10 Applying the electric field from the side wall of a DLD device enables to create higher electric fields with the same voltage due to the reduced distance between the electrodes. Figure adapted from [50] with permission of the Royal Society of Chemistry. 17
1.11 Single cells can be isolate in parallel by wells, traps and patterns or continuously by flow confinement or droplets. Figure reproduced from [6] with permission from the American Chemical Society. 18
1.12 The planar electrode structure (A) supplied with a positive and negative voltage creates a strong DEP force due to the high electric field gradient illustrated by the square of the magnitude of the electric field (B). Figure adapted from [68] with permission from the American Chemical Society. 19
1.13 The intersecting signal lines of the pDEP trap, create the DEP signal to trap cell (A). When both signal lines are put to ground, there is no trapping force (B) and the trapped cell is released. Figure reproduced from [68] with permission from the American Chemical Society. 20
1.14 The three-dimensional electrodes are placed within a microfluidic channel and connected with underlying signal lines. The signal of every second electrode can be individually controlled. Figure reproduced from [69] with permission from the American Chemical Society. 20
1.15 Electric field cages are created by electrodes patterned at the bottom of a microfluidic chamber. Changing the applied configuration, beads and cells can be moved around in the chamber. Figure adapted from [70] with permission from IEEE. 21
1.16 Flowing a cell through a microfluidic channel placed on suspended. Figure adapted from [75] with permission from The Royal Society of Chemistry. 23
1.17 Flowing a cell through a microfluidic channel, which is place on suspended cantilever (a), the resonance frequency of the cantilever changes (b) and the change in the resonance frequency is proportional to the cells buoyant mass. Figure adapted from [83] with permission from AIP Publishing. 24
1.18 (a) Single cells are hydrodynamically trapped between a cell-culturing and a suction channel, a stimulus electrode is patterned in the cell-culturing channel and an individual recording electrode behind each trap. (b) The relative magnitude of the impedance signal at $1MHz$ is directly anti-proportional to the cell length. Figure adapted from [100] with permission from Springer Nature. 25

1.19 Three octopoles of different inter-electrode distance are positioned along a microfluidic channel. Cells are investigated in the differently sized octopoles, in which they are positioned using a single laser tweezer. Figure adapted from [124] with permission from Elsevier. 26

1.20 In order to achieve simultaneous nDEP trapping and electrorotation, the applied DEP and ROT signals are either alternated (a) or superposed (b). Figure (a) reproduced from [94] with permission of John Wiley and Sons. Figure (b) reproduced from [88] with permission of the Royal Society of Chemistry. 27

2.1 Dielectrophoresis is a phenomenon in which a net neutral particle is getting polarized in a gradient electric field. If the particle is more polarizable than the surrounding medium, as shown in (a), it moves towards high field regions. If the particle is less polarizable than the surrounding medium, as shown in (b), it moves toward the low field region. Figure reproduced from [140] with permission of Elsevier. 34

2.2 The single-shell model assumes a particle to consist out of a homogeneous sphere surrounded by a homogeneous shell. Figure reproduced from [142] with permission from John Wiley and Sons. 37

2.3 The flow profile as well as the forces acting on a particle in a microfluidic channel. Figure reproduced from [149] with permission from Marta Comino. 38

3.1 Cells placed in a rotating electric field, can either rotate in the direction of the rotating electric field if $Im[CM] < 0$ (red particle) or against the electric field if $Im[CM] > 0$ (green particle). Figure reproduced from [149] with permission from Marta Comino. 52

3.2 SEM micrograph of three dimensional-elecrodes integrated in a dielectrophoretic trapping array. The electrodes are connected by two underlying metal layers, which are insulated by a SiO_2 layer. The cross-bar structure of the metal allows to contact 64 electrodes with only four off-chip connections. Figure depicted from [152]. 55

3.3 (a)At a DEP traping frequency of 10 kHz and a voltage of 5 V, bubbles appear immediately at the electrodes. The red arrows point to the created bubbles. (b) Averaged electrorotation spectra of human immortalized T lymphocytes in media of different conductivity. 56

3.4 SEM micrograph of a DEP microcage array of three-dimensional electrode with individual connections for every electrode. Figure depicted from [153]. 57

3.5 Series of micrscope images showing the subsequential trapping of a cell (a-b), the analysis by electrorotation without flow (c-f), the retrapping after the analysis (g-h) and the release of the cell turning on the flow (i-j). Figure depicted from [153]. 58

4.1 Differently-sized particles are flown through a labyrinth featuring of microfluidic post. Due to there finite size and the shift of the rows, the particles are eventually colliding with the posts. Due to their radius, the center of mass of larger particles are further pushed away from the stream line than smaller particles. Figure adapted from [47] with permission from the Royal Society of Chemistry. 86

4.2 (a)Definition of the parameters for the DLD devices. (b) Small particles will follow the flow direction and flow in the zigzag mode at an angle of 0° while larger particles in the displacement mode go along the alignment of the posts under an angle to the average microfluidic flow. Figure adapted from [47] with permission from the Royal Society of Chemistry. 86

4.3 (a) The DLD setup connected the microfluidic chip under an inverted microscope to a pressure system and a frequency generator which were controlled by a computer. (b) close look to the microfluidic chip under the microscope. The microfluidic connectors are glued to the device and the electronic contacts are soldered on. 88

4.4 The chips with the three-dimensional electrodes have three inlets and one outlet. Subsequent rows of electrodes are connected to the opposite signal of a sinusoidal $10MHz$ AC signal. (A) Sketch of the device layout. The sample is injected in the middle inlet on the left and driven over the device, where subsequent rows are connected to opposite AC signals. (B) Picture of the device directly before using it. Tubes as reservoirs are glued on the chip and cables are soldered on the exposed metal to apply the AC signal. (C) SEM micrograph of the three-dimensional electrodes, which are connected from both sides, with the different electric signal. The color indicated, which signal is applied. Figure reproduced from [157] with permission of John Wiley and Sons. 89

4.5 Principle of investigation of the devices. (A) Beads below the critical size of the device are flown through the device in zigzag mode. They leave the device at outle number 7 and 8. (B) The same beads with an applied voltage. They displace and leave the device at outlet 14. (C) The different travelling modes of the beads through the device. Top: displacement mode. Middle: mixed mode with enlarged periodicity. Bottom: zigzag-mode. (D) The average outlet through which the beads leave the device depends on the travelling mode. In the zigzag mode the beads leave the device at outlet 8, in the mixed mode at outlet 10 and at the displacement mode at outlet 14. (E) The number of beads at each outlet are counted to evaluate the behavior of the beads at different conditions. Figure reproduced from [157] with permission of John Wiley and Sons. The microscope images where taken at NanoLund of devices produced at EPFL. 90

4.6 The averaged outlet position of beads of different sizes is plotted versus the applied voltage. The applied pressure is $0.3mBar$. (a) Characteristic curves for $200nm$, $500nm$, $1\mu m$ and $2\mu m$ diameter beads. (b) Zoom for $1\mu m$ and $2\mu m$ diameter beads. The cross-over voltages of $1.7V$ and $2.2V$is indicated by a vertical line. 91

4.7 The square root of the applied pressure versus the applied voltage is plotted, when reaching full displacement. The red line shows the linear fit with offset of $1.9V$, a slope of $0.6V/mbar^{0.5}$ and $R^2 = 0.98$. 92
4.8 For particles which are due to their size without electrical field applied in the zigzag mode, the viscous drag force is laterally competing with the DEP force. The critical voltage can be determined by comparing these two forces. Figure reproduced from [157] with permission of John Wiley and Sons. 93
4.9 Two-dimensional COMSOL models of the microfluidic stream lines (black lines) and the electric field square (colour code) for different electrode geometries. (a) round post shapes, which create more homogeneous and smaller electric fields. (b) teardrop shaped electrodes, with high gradient and high electric field squares. More importantly the electric field gradient is the highest, where the critical particles decide their trajectory, because of the separation of the microfluidic field lines. The red arrows point to the critical area. 95
4.10 SEM micrographs of different electrode shapes. (a) traditional round electrode shapes. (b) sharp edged teardrop shaped electrodes for smaller critical sizes. . . 96

Introduction

The idea of lab-on-a-chip (LOC) devices, or miniaturized total analysis systems, was first reported in literature by A. Manz, N. Graber and H. M. Widmer in 1990 [1]. Since then enormous efforts have been undertaken to realize systems which analyze automatized biological samples on a computer chip.

A very prominent example is the bio-tech startup Theranos, which raised more then US$ 700 million and had a US$ 10 billion evaluation. They claimed to have developed a technology which was able to perform blood analysis using volumes that could be taken from a little prick. Comparing their results to standard methods, researchers found an increased variability of their tests [2]. This variability was caused by the fact that they diluted their sample in order to have a sufficient volume to have them analyzed by third parties using standard laboratory blood testing methods. In fact, they did not apply their own method. Theranos was sued by their investors and eventually went out of business in 2018 [3].

This case shows the desire of biomedical industry for functional lab-on-a-chip devices. Lab-on-a-chip technologies may have enormous scientific and economic impacts. However, LOC devices need to be developed step by step, similarly to a sample which has to be treated in the lab step by step as well. First, the sample needs to be extracted and brought to the chip, then the sample needs to be purified before it can be analysed and the results can be read out. This combines research in various disciplines. An important component for these devices is the *debulking* and purification of the biological sample. This can be done based on various properties of the biological sample, such as for example size or shape of the particles. Some characteristics of a sample, which cannot directly be observed using a microscope, are the dielectric characteristics of the bio-sample. However, these properties can be used to distinguish and sort these particles.

Our laboratory has recently developed a technology which allows to implement three-dimensional electrodes in microfluidic channels [4]. These electrodes can be used to create homogeneous electric fields in microfluidic channels over the complete channel height. Using these fields, we can use dielectrophoresis to position, investigate and sort bio-particles based on their dielectric properties.

Using these electrodes, we designed and built two systems, which improve the performance

of simple microfluidics.

The first system uses a parallelization of electrorotation, a technology very sensitive to the dielectric properties of single cells, especially of the membrane. This method gathers information from the speed of rotation of particles in a rotating electric field. The capability of our system to keep cells trapped in suspension over time and continuously monitor their membrane properties, could be used to monitor the protein deposition on the membrane and gain a better understanding of the underlying mechanisms. This might be especially useful for insights in the development and spread of Alzheimer's disease, in which the deposition of amyloids, a neurotoxic protein, on the cell membrane might give indications about the disease process.

The second system uses these electrodes in an alternating-current deterministic lateral displacement system (AC-DLD). Plain DLD devices sort particles based on size, which is determined by the design layout. Adding additional forces in these devices can tune the specific size at which the particles are separated. Using three dimensional electrodes as posts in these DLD devices, applying AC electric fields on them can locally create dielectrophoretic forces, which tune the sorting size of the devices. Additionally this technology could be used to sort particle not only based on size, but based on their dielectric properties as well, since the dielectrophoretic force depends on the polarizability of the particles.

Dielectrophoresis is already used in some diagnostic and therapeutic devices. Three dimensional electrodes can be used to fine tune the performance of dielectrophoretic devices and create locally defined electric fields within microfluidic devices. By employing these electrodes to parallelize electrorotation analysis or to implement additional forces in DLD devices, we could show their potential for application. We demonstrated their functionality in analytical devices and these actuators and functions can now be added to the toolbox from which researchers and engineers can serve themselves in order to build lab-on-a-chip devices.

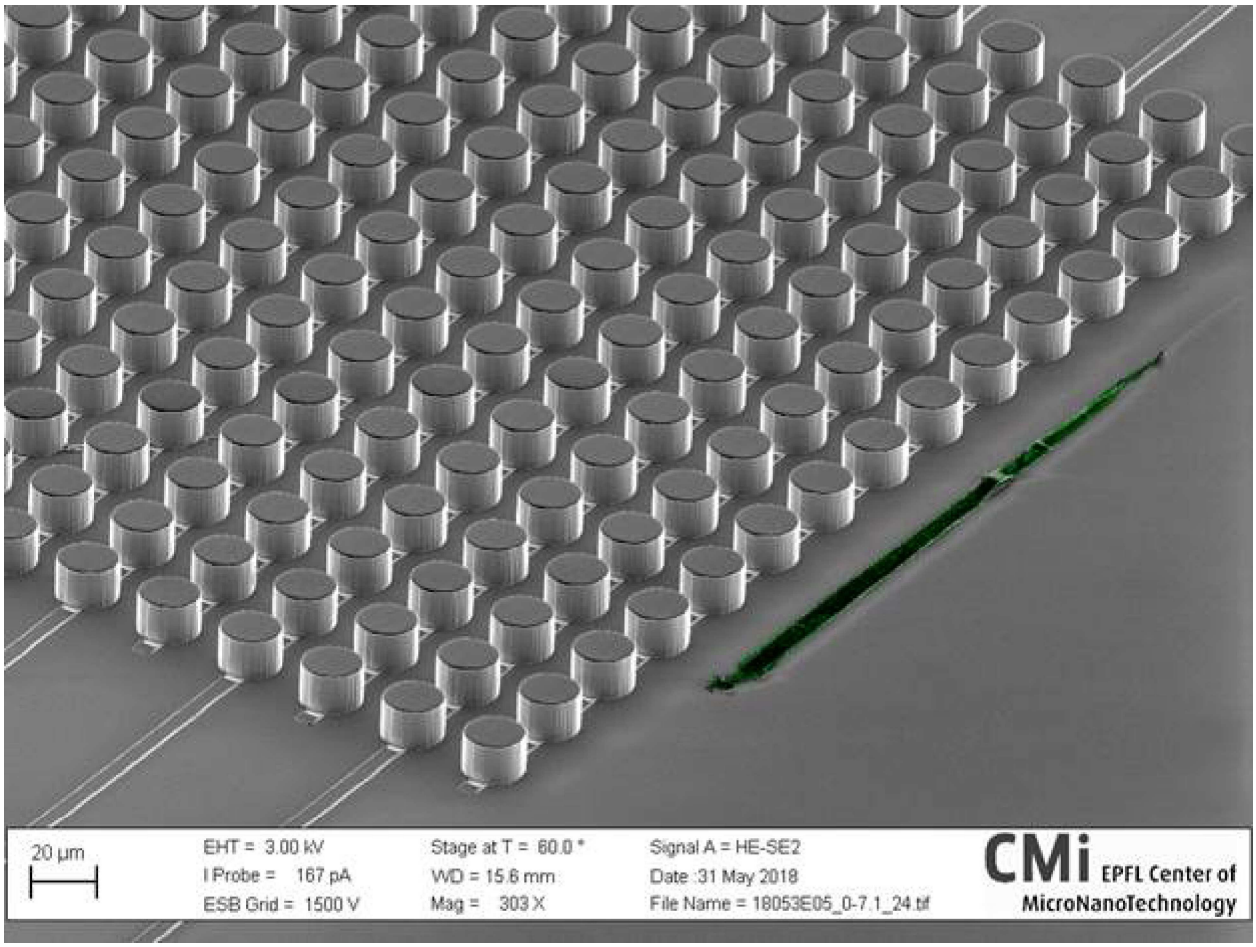
20 µm
EHT = 3.00 kV
I Probe = 167 pA
ESB Grid = 1500 V
Stage at T = 60.0 °
WD = 15.6 mm
Mag = 303 X
Signal A = HE-SE2
Date :31 May 2018
File Name = 18053E05_0-7.1_24.tif
CMi EPFL Center of MicroNanoTechnology

CMi Picture of the Month May 2018 Run up: Snake in DLD labyrinth

"This snake left its platinum skin in front of this deterministic lateral displacement (DLD) labyrinth out of metal covered SU-8 posts. Is it small enough after its shedding to get straight through the labyrinth or will it get displaced by a magic dielectrophoretic force hidden in the labyrinth?"

1 On-chip manipulation and analysis of bio particles

In order to analyze a biological sample directly on a chip, several subsequent tasks have to be performed. The sample has to be inserted in the chip and analyzed. However, not all particles in a biological sample are meaningful to analyze and will eventually create unnecessary noise in the analysis process. Therefore, in a first step a purification of the sample is needed. Usually several species of cells or particles are within the sample. These populations have to be sorted in order to perform a detailed analysis of a specific species or to find differences between samples.

In the following, several methods to sort one population of cells and bio particles from another one will be presented. The methods are classified in the fundamental property of the particles, based on which they are sorted. For each property, a few benchmark techniques are presented.

After the purification of a sample, one might be interested in analyzing a few or one specific cell. Eventually one single cell can give insights in the state of the whole organism [5], however in order to analyze multiple single cells, they first have to be separated for analysis. Several methods to separate single cells exist and they can in principle be distinguished between parallel single-cell isolation and continuous single-cell isolation [6].

After the separation of single cells, one might finally be interested in the specific properties of a single cell in order to compare it with the properties of the population. Therefore, one has to analyze one single cell at a time. Here we want to focus on label free and non-destructive single-cell analysis techniques, since they allow a continuous analysis over time or further downstream analysis. In the third section of this chapter, we present technologies which can continuously analyze an individual cell. The biomechanical properties of cells can be segmented in three types, the optical properties, the mechanical properties and the electric properties of the cell. We will present technologies to reveal each of this properties of the cell and present some of these techniques in detail.

In all these steps, dielectrophoresis can be used; for sorting, for arraying and for cell analysis. The dielectric forces depend on the electric field created in a microfluidic channel. Some

sorting devices show better functionality if homogeneous forces over the complete channel height are created. In order to create these, three-dimensional electrodes are advantageous, however, they can be challenging to fabricate. Therefore at the end of this chapter, existing fabrication technologies are presented, as well as the advantage of homogeneous fields is elaborated.

1.1 Population sorting

Population sorting is an important component in many diagnostic and therapeutic devices. In order to analyze a specific cell type for diagnostics it first has to be separated from the bulk of other cells, which is called debulking. At the same time for therapeutics specific cells have to be manifolded. In order to manifold only one cell type and no other cell, they have to be separated before culturing [7].

Microfluidic technologies for sorting of populations can be classified in three categories [7]

- fluorescent label-based
- bead-based
- label-free particle sorting

As the name implies, fluorescence label-based techniques, first put a fluorescent label on the cells or particles. Usually this is followed by a i) serial interrogation of the sample by a laser beam, ii) a real-time classification and a iii) rapid, command-driven sorting [7]. Fluorescence activated cell sorting (FACS) is a well established technique, which is able to screen thousands of cells per second [8].

Bead-based sorting, uses magnetic beads which are attached by a marker, usually an antibody, to the cell. In the next step a magnetic field is applied to the device, which retains the magnetic labeled cells or bio particles inside the device. In a consecutive step, the magnetic field is removed and therefore the targeted particles are released from the device. This technology is called magnetic activated cell sorting (MACS) [9].

Both, FACS and MACS, are well established and mature technologies. On the other side, label-free cell sorting has the advantage that a reduced sample preparation time is needed, because no prior labeling is needed for sorting, since the analysis/sorting is based on mechanical or dielectric properties of the cells or particles [10]. Additionally, they keep the cells in their original state without any modification, which might be advantageous for further downstream analysis or reculturing of the specific cell population. Since this technologies bare major interest for the future in biotechnology we will give in the following an insight in their functionality and principles.

Carey et al. give a classification of label free technologies for population sorting and measurements [10], in which they differentiate the read out principle in

- electrical
- optical
- hydrodynamic
- acoustic

additionally they evaluate the throughput of exemplary technologies in each of the read out methods as shown in Fig. 1.1.

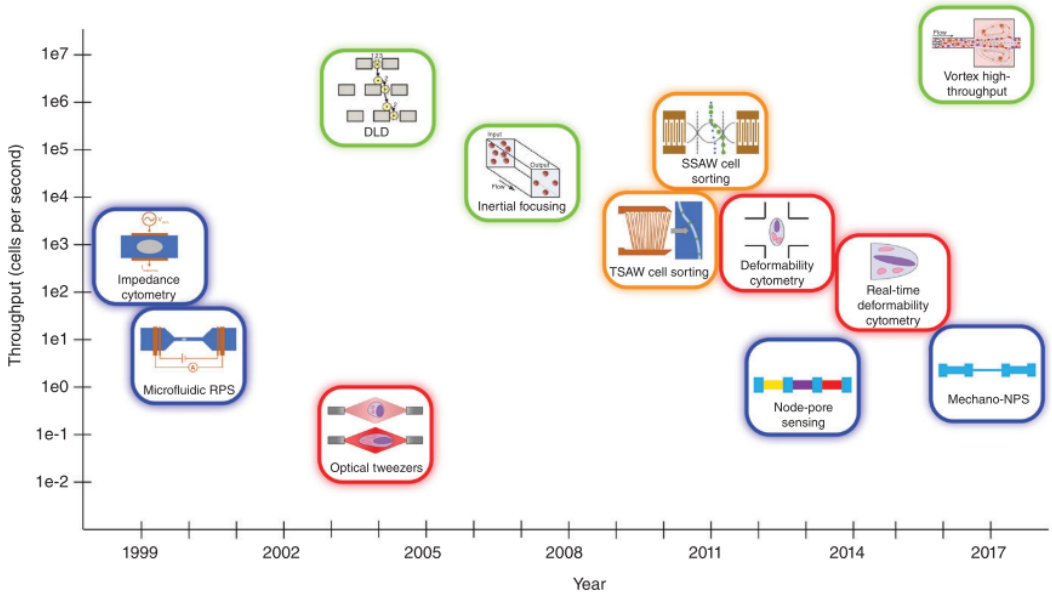

Figure 1.1 – Within the last twenty years different technologies to sort populations have been developed, their throughput is noted on the y axis. Additionally, their nature of analysis is noted: electrical=blue, optical=red, hydrodynamic=green, acoustic=orange. Figure reproduced from [10] with permission from John Wiley and Sons.

In my opinion, a better classification could be to segment the technologies based on the property which the population is sorted on

- based on size
- based on deformability
- based on electrical properties

- based on surface markers

Carey et al. [10] mention these criteria, but rather classify on the read out. Instead, in the following I will give some examples for realizations of the sorting mechanisms on each property.

1.1.1 Based on size

The size of a cell is an obvious difference between cell populations, which can directly be seen under the microscope. However, in order to sort particles based on their size, systems were developed, which can continuously sort them in-flow based on their size.

Inertial focusing enable to position particles of a specific size at a specific distance from the channel wall, which can be used to separate particles based on their size [11, 12]. Depending on their position at the outlet, the particles are guided into separate channels.

Another possibility to separate cells based on size is using a high throughput vortex chip. Blood or diluted blood is driven through small microfluidic channels, at some point the channel passes a wider rectangular chamber, in which flow vortexes are created. While smaller cells continue flowing through the chamber, larger cells are getting into the vortex stream and are getting trapped in the chamber [13, 14]. This system has a very impressive throughput of $8ml/min$ for 10 times diluted blood and is for example used to sort out CTCs [13].

Deterministic lateral displacement devices, which consist of slightly offset rows of pillars in microfluidic channels, can be used sort particles based on size [15, 16, 17]. Particles above a characteristic size of the device are guided by the direction of the posts, while smaller particles are guided by the microfluidic flow, which is under a slight angle to the posts.

Field flow fractionation in its original design is used to sort particles based on size, by means of a microfluidic stream crossed with a secondary perpendicular stream. Particles of different size are differently affected by the secondary stream and get driven to the bottom of the primary channel. Due to the parabolic flow profile and the corresponding flow velocity depending on their position in the channel, they accumulate at different positions of the primary channel and therefore are separated [18, 12, 19, 20].

Stranding surface acoustic waves can be used to separate particles of different sizes. An acoustic signal is applied over a microfluidic channel. Particles in suspension are flown through this microfluidic channel. The applied acoustic creates a standing wave over the microfluidic channel and creates pressure nodes. The cells speed towards the pressure node is proportional to the square of the cell radius. With this principle particles, especially cells of different sizes can be separated [21, 22]. For example, Nam et al. [22] could separate red blood cells from blood with a purity ratio of over 99% and platelets with a purity of 98%.

In the following we will briefly explain an example of inertia particle sorting and an example of field flow fractionation in more detail.

Inertia particle sorting in a long spiral

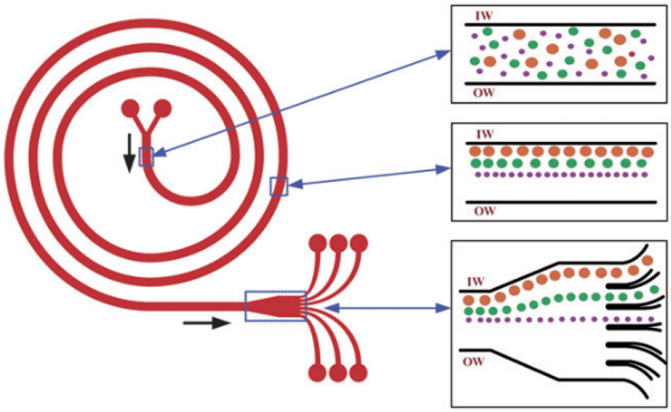

Figure 1.2 – Particles of different size are flowing through a microfluidic spiral. Their equilibrium position of the inertia lift and the dean drag force determines at which position they leave the channel between the center of the channel and the channel side wall. Based on this they can finally be directed in separated channels. Figure reproduced from [12] with permission from the Royal Society of Chemistry.

In order to sort particles based on their size, a sorting mechanism based on inertial microfluidics can be used. In a plane Poiseuille flow, a parabolic flow profile creates a shear gradient in the fluid. This gradient induces a inertial lift force, which drives the particle away from the center of the microfluidic channel towards the side wall. However, the drag force counteracts this force and drags the particle in the center of the channel. For each particle size their is an equilibrium of these forces at a specific position within the microfluidic channel, as shown in Fig. 1.2. A spiral channel can be used to build a long channel, at the end of which particles of different sizes leave the spiral at different positions within the channel. Separating the single channel into several separated ones allows to allocate particles of different sizes in separate channels [12].

Field flow fractionation

Field flow fractionation is a separation method to sort particles of different properties in suspension [18]. Particles in suspension are flown through a wide microfluidic channel. Due to the size of the device, the flow profile within the channel is parabolic. Therefore particles in the middle of the channel travel faster than particles at the top or the bottom of the channel. As shown in Fig. 1.3 (a), applying a perpendicular flow to the sample flow creates a vertical force on the particles. Due to the different size of the particles, the exerted force on them by the secondary flow is different, therefore their vertical position within the microfluidic channel and correspondingly their lateral speed due to the parabolic flow profile depends on their size. Particles which are strongly affected by the cross flow are further down in the

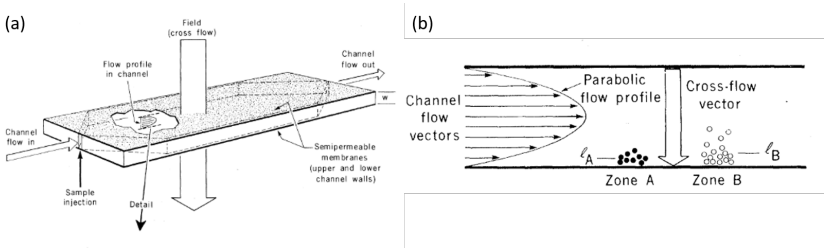

Figure 1.3 – Field flow fractionation is based on a flow in a wide microfluidic channel featuring a parabolic flow profile, which is combined with a cross flow vector, leading to a separation of particles. (a) The schematic layout of the device. (b) Cross section of the channel with the relevant flows. Figure adapted from [18] with permission from The American Association for the Advancement of Science.

channel and travel slower than particles which are less affected and remain more centered. Eventually, all particles will accumulate at the bottom of the channel. However, due to the different travel speed in the parabolic flow profile, they will accumulate at different zones, as illustrated in Fig. 1.3 (b). A semipermeable membrane is placed at the bottom of the channel, the particles can transverse this membrane and can be separated depending on their travel distance in the main channel and correspondingly their size [18].

The cross flow is not necessarily provided by a second microfluidic flow, it can be provided by any other force that drives the particles from the top or middle of the channel down to the bottom. The particles will eventually be separated laterally based on the effect of this force on the specific particle. The cross flow can be provided either by a thermal flow, pH gradient, electrophoresis, dielectrophoresis [23] or other techniques [24].

1.1.2 Based on deformability

Another property on which populations can be sorted is their deformability, which is an important cell property, since it can for example give an indication of higher pluripotency [25].

Using an optical stretcher, cells can be stretched into an ellipsoid within an optical trap. The deformability is determined by the aspect ratio of this ellipsoid [26, 27]. It can reveal information about the cytoskeleton of the cell and can alternate in many diseases, as for example in case of cancer [26].

A promising technology to separate cells based on their compressibility, which is closely related to deformability can be done by applying standing surface acoustic waves over a microfluidic channel [21]. Depending on their compressibility different cells will position at different lateral positions of the microfluidic channel and can therefore be separated.

Another approach testing the deformability of cells is by flowing them through a narrow channel. Their shape becomes bullet-like, due to the shear. The aspect ratio of this shape can

be observed under a microscope and investigated [28, 29, 30]. This can be used for *mechanical phenotyping* of the samples, based on their single-cell deformability [28, 31], or to distinguish between cell-cycle phases, to predict stem cell differentiation or to identify cell populations in whole blood depending on their mechanical properties [29].

Deformability can be accessed in-flow by an ad hoc cytometer. Two high-velocity fluid streams collide and deform a cell into an ellipsoid between them, the deformation of the cell gives and indication about its state [25] as explained in the following.

Deformability cytometer

The group around Dino Di Carlo developed a deformability cytometer and found that the deformability of cells can be an early biomarker to identification the differentiation of pluripotent stem cells. It is likely linked to nuclear structural changes. Additionally, observing the deformability of native populations of leukocytes and malignant cells, which were taken from pleural effusion, it can predict the immune activation of cancer patients with a sensitivity of 91% and a specificity of 86% [25].

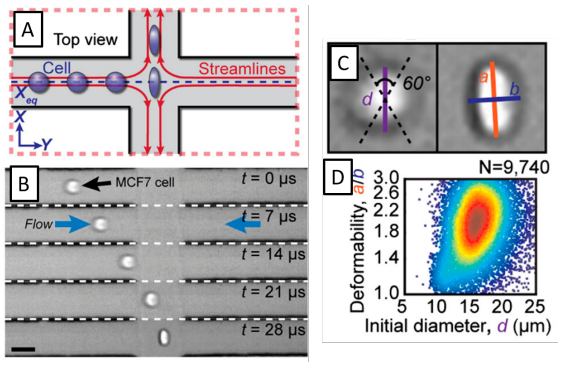

Figure 1.4 – Two high velocity microfluidic streams are colliding and deforming the cell in the center of the channel. (a) Conceptional sketch. (b) Image series of recorded experimental video. (c,d) The cell initial diameter and its calculated deformability can be plotted in a diagram. Figure adapted from [25] with permission from PNAS.

Two high-velocity microfluidic streams are colliding at a microfluidic intersection. Before cells are getting to the center of collision they are centered in the channel by inertial focusing. Once the cells are at the center of collision, they are getting deformed and following one of the outlets as shown in the sketch in Fig. 1.4 (a) or the experimental data in Fig. 1.4 (b). A high speed camera is used to capture pictures of the deformed cells and their deformability is analyzed as shown in Fig. 1.4 (c). The cells initial diameter d can be plotted versus its deformability a/b, as shown in Fig. 1.4 (d).

As already mentioned, based on this data the leukocytes from cancer patients can be identified. The system has a throughput of $2000 cells/s$ [25].

1.1.3 Based on dielectric properties

Another intrinsic property of cells are their dielectric properties, such as the cytoplasm and membrane conductivity or permittivity. They can be revealed by different methods and cell populations can be sorted based on these findings.

One of the most prominent example to reveal the dielectric properties is impedance spectroscopy. An alternating electric current signal is applied over a biological sample. The impedance of the sample is measured at different frequencies and reveals details about the dielectric properties [32, 33, 34, 35, 36]. In in-flow impedance spectroscopy usually the dielectric parameters at a few specific frequency are observed while the sample is passing the electrodes. Similar to FACS, subsequent sorting can be performed based on the analysis of the impedance signal.

Another possibility to separate particles based on their dielectric properties is dielectrophoresis. Applying an alternating current electric field via electrodes in a microfluidic channel creates high and low field regions, depending on the structure of the device and the dielectric properties of the sample, the conductivity of the surrounding medium and the applied frequency. The particles experience a force towards regions on the chip with high electric fields or low electric fields. Depending on their localization and the force towards or away from high and low field regions, particles can be separated [37, 38, 39, 40, 35, 41].

In the following we will present (i) one example of an impedance flow cytometer from our lab [34] and (ii) a dielectrophoretic population sorting device [37] in more detail.

In-flow impedance cytometer using three dimensional electrodes

Three dimensional electrodes are placed within a microfluidic channel, they separate a microfluidic channel in two sections as shown in Fig. 1.5 (a). The lock-in amplifier measures the impedance signal between the electrodes in a differential manner, meaning, the signal at one of the channel cross-sections is compared to the other one. When a cell passes through the impedance cytometer, the electric resistance at one of the channel sections is changing, in comparison to the other section where only buffer is present. The change in the electric signal depends on the dielectric properties of the cell. Observing the in-phase signal at $6MHz$ and the out of phase signal at $14MHz$, one finds that activated $CD69^+$ T lymphocytes can be distinguished from non-activated $CD69^-$ T lymphocytes, as shown in Fig. 1.5(b) [34]. Correspondingly Rollo *et al.* [34] could show a separation of activated and non-activated T lymphocytes based on their electric properties while flowing through a microfluidic channel using three dimensional electrodes.

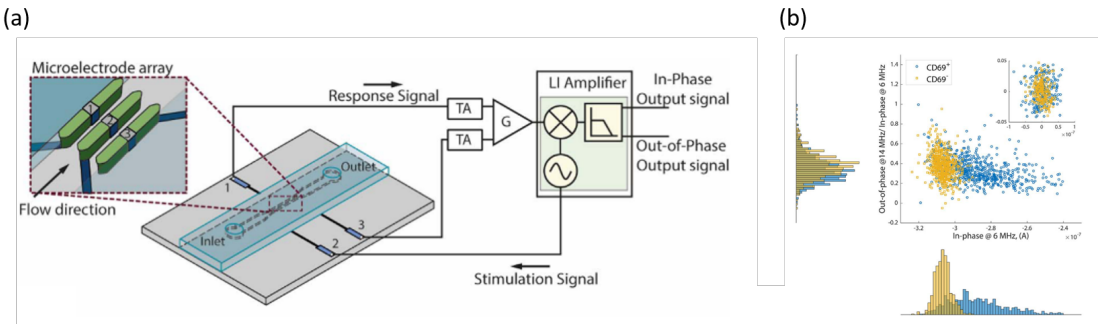

Figure 1.5 – Using three dimensional electrodes (a) in an electrical impedance-based setup, activated and non activated human T lymphocytes can be identified by their electric impedance (b). Figure adapted from [34] with permission from Elsevier.

Dielectrophoretic sorting

Cell populations can be sorted by dielectrophoretic trapping. The dielectrophoretic force which is exerted on the particles depends on the size of the cells as well as on its polarizability. If a population is homogeneous in size, the separation will depend solely on the polarizability of the particles, which depends on its dielectric properties. One example is the separation of viable and non-viable yeast cells[37]. Dead and alive yeast cells have the same average size. However, their dielectric properties are different. Viable and non-viable yeast cells can be separated by a system of patterned interdigitated electrodes at the bottom of a microfluidic channel, as shown in Fig. 1.6,. The viable yeast cells experience pDEP, since they are more polarizable than the surrounding medium, and thus move towards the edges of the interdigitaded, castellated electrodes, while the non-viable yeast cell experience nDEP, since they are less polarizable than the surrounding medium, and thus will move in between the electrodes or on top of them where the gradient of the electric field is the smallest as seen in Fig. 1.6, . A subsequent washing step, allows to wash away the non viable cells, which experience nDEP and are pushed away from the surface, while the viable yeast cells are trapped at the edges of the electrodes and therefore remain even after washing [37].

1.1.4 Based on surface markers

Label-free particle separation can be combined with surface markers analysis . A very interesting approach was presented by Balakrishnan *et al.*, where they coated specific regions in a narrow microfluidic channel with antibodies. Cells were flown over these regions coated with antibodies. Corresponding to the surface markers on the cell surface, the cells interacted more or less with the antibodies coated in the microfluidic channel and correspondingly their travel time over the coated region varies. The travelling time could be recorded by node-pore sensing and depending on the time in each region, the specific surface markers of each cell could be identified in-flow based on the travelling time over the specific antibody [42].

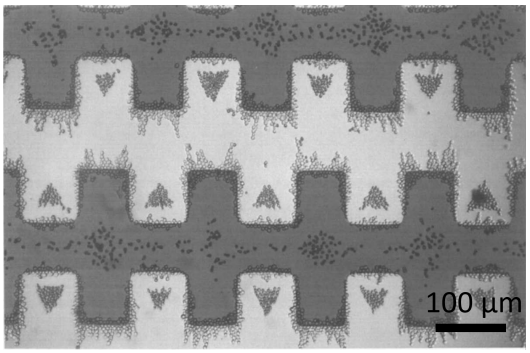

Figure 1.6 – Applying a $5V_{pk}$ signal of a frequency of $10MHz$ at interdigitaded, castellated electrodes, viable and non-viable yeast cells can be separated. The viable yeast cells accumulate on the edges of the electrodes, while dead yeast cells accumulate on top and in between the electrodes. Figure adapted from [37] with permission from Elsevier.

1.1.5 Combined size- and dielectric property based sorting by alternating-current deterministic lateral displacement

Deterministic lateral displacement (DLD) was fist described in 2004 by Huang et al. [15]. Since then, it was extensively studied and different pillar shapes and designs were used to sort particles not only based on size, but as well on shape, deformability and other properties [43].

Deterministic lateral displacement is used to sort particles by size. It consists of a microfluidic channel in a laminar flow regime. The channel features a regular pattern of posts/restrictions. Each consecutive row is shifted by a set distance to the previous [43].

The particles are driven through the post labyrinth by a fluid flow and their center of mass follows the microfluidic stream lines. Due to their finite size and the periodic shift of the rows, the particles will bump into the posts. The contact to the posts happens there, where the stream line they follow is less distant to the post wall then the particle radius. The interaction leads to a displacement of the center of mass and therefore the complete particle away from the post. The displacement for non-deformable particles is so big, that the center of is in the distance of the particles radius to the post wall. Consequently, larger particles are due to their size more often interacting with the posts, since their stream line can be further away from a post in order to have an interaction with the post and their displacement is larger, due to their larger radius. This leads to a different trajectory of larger and smaller particles through the labyrinth. Smaller particles are going in zigzag through the device and end up where the flow lines drive them, while larger particles displace with the device geometry and go toward the side of the device. This effect can be used to sort particles based on their size.

A goal of many sorting devices is to sort particles in the range of nanometers. Neglecting all side-effects like, for example, diffusion, theoretically, there is no lower size limit for deterministic lateral displacement devices. The structures simply have to be fabricated very small, which allows to sort very small particles. However, practically this leads to major fabrication

challenges. Recently, a group from IBM could fabricate gap sizes down to $25nm$, as shown in Fig. 1.7 [44]. Which allowed them to sort particles between $20nm$ and $110nm$ and successfully apply their technology to the size based sorting of exosoms. They showed the sorting of exosoms above $100nm$ particle size. For the device fabrication they used electron beam and deep-ultraviolet lithography to pattern the nano-DLD pillars and etch the structure with a reactive ion etching process. Sorting exosoms is valuable for liquid biopsy in the aim to purify the sample. However, the small gap size already requires a purified sample, since particles larger than the gap size will lead to clogging and to a failure of the device, additionally, the throughput due to the dimension of the device is small, because the small gap reduces the cross-section for the microfluidic flow.

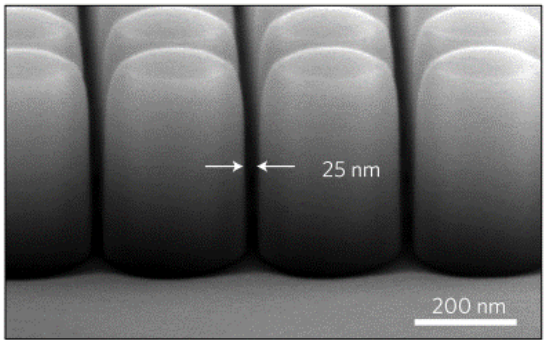

Figure 1.7 – SEM micrograph of the nanosized DLD gaps. Exosoms can be sorted by size in this device. Figure reproduced from [44] with permission of Springer Nature.

Combining deterministic devices with other forces, like for example mechanical strain [45] dielectrophoretic forces [46, 47], gravity [48] or in combination with surface acoustic waves [49] bears the potential to tune the devices according to the particle size, and allows at the same time to use other properties for the particle sorting.

In 2008 Chang *et al.*, the team presented a device where the PDMS posts are replaced by virtual posts coming from a repulsive nDEP signal at this location. The virtual electrodes are composed of an insulated metal layer, carrying the DEP signal, which is opened at the position of the virtual electrode. Applying an AC electric field at the electrodes at nDEP conditions creates a repulsive force from this region, which can replace the effect of a PDMS pillar, as shown in Fig. 1.8[46].

Another approach is to combine DLD devices with DEP that will have the effect to reduce the critical size of the DLD device. This was first done by Beech *et al.* in 2009 [47], who used electrodes in chip's inlet and outlet, as sketched in Fig. 1.9. The PDMS posts in the device act as restricting posts for microfluidic flow needed in the deterministic lateral displacement devices and at the same time, they shape the electric field inside the device. They act as insulating structures to give rise to an insulator based DEP (iDEP) configuration. Since the electric field is confined, high and low field regions are created between the posts. The additional DEP force can tip the trajectory of the particles flowing through the device. However, due to the

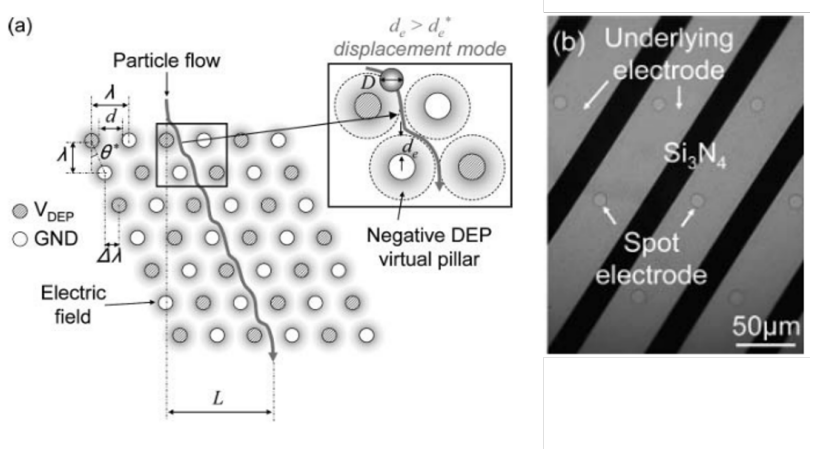

Figure 1.8 – (a) The working principle of the virtual DLD posts is that the posts are replaced by electrodes which create a repulsive DEP signal. (b) Underlying interconnections for the electrodes are insulated with Si_3N_4 and they are opened at specific positions, where the virtual posts are created. Figure adapted from [46] with permission of the Royal Society of Chemistry.

long distance between the inlet and the outlet of the device, high voltages are needed for these devices in order to create an electric field which is sufficient to change the trajectory of the particles. This limits the frequency range of the signals which can be applied.

A similar approach was recently presented by Calero *et al.* [50]. Instead of placing the electrodes in the inlet and outlet of the microfluidic channel, the electrodes are placed along the two sides, as sketched in Fig. 1.10. The electric field is now created over the width of the channel. This distance is usually much smaller then the length of the channel. Therefore, the applied voltage can be smaller in order to obtain the same magnitude of the electric field in the channel. However, the fundamental working principle of these two devices is different, since the electric fields are applied in one case along the channel and in the other case across the channel. Therefore the device with the electrodes placed at the in- and outlet creates the electric field confinement between the electrodes in the same row (perpendicular to the flow) and the displacement mode can be obtained using pDEP. The sidewall electrode device creates the confinement between the electrodes of the same column and therefore uses nDEP in order to change the trajectory of particles from the zigzag to the displacement mode.

This devices could reduce the needed voltage for changing the traveling mode of particles through the device from kV to several hundreds of V. However, operation with standard frequency generators and application of high frequencies is still not possible. Our approach, presented later on, using three-dimensional electrodes as microfluidic restrictions and therefore allowing to create the electric field inside the device with electrode distances of a few micrometers allows to create high fields and field gradients with a few V amplitude generated by a standard frequency generator and frequency up to several MHz. This enables to further reduce the sorting size and could enable additional sorting possibilities based on the dielectric properties of the particles flowing through the DLD labyrinth.

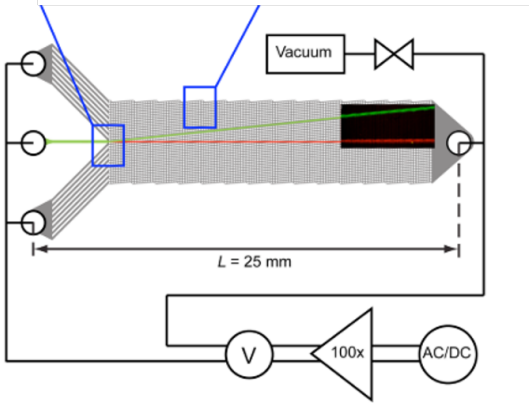

Figure 1.9 – Layout of a DLD device combined with DEP applying a voltage from the inlets to the outlet. Figure reproduced from [47] with permission from the Royal Society of Chemistry.

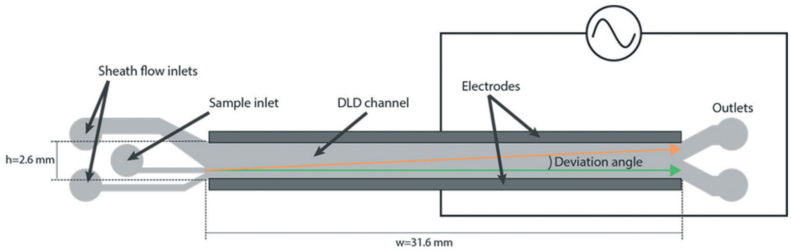

Figure 1.10 – Applying the electric field from the side wall of a DLD device enables to create higher electric fields with the same voltage due to the reduced distance between the electrodes. Figure adapted from [50] with permission of the Royal Society of Chemistry.

1.2 Single-cell arraying

Besides sorting a complete population, analysis of individual cells gives valuable insights on their pathology and give information about the state of the whole organism [5]. It gives the possibility to reveal the signal of a single cell, which otherwise would have been hidden in the bulk behavior [51]. In order to analyze multiple biological particles and therefore obtain statistical relevance, for example for single-cell analysis (SCA), they have to be isolated and arrayed [52]. Isolation for single-cell applications can be performed by micro devices using for instance micro-wells, patterns, droplets or traps [53]. As illustrated in 1.11, one can classify the separation of single cells in two types of methods [6]

- parallel single-cell isolation
- continuous single-cell isolation

While parallel single-cell isolation localizes the cells on a specific, fixed position on a microchip, by different possibilities which will discussed, continuous single-cell isolation separates the cells while moving [6].

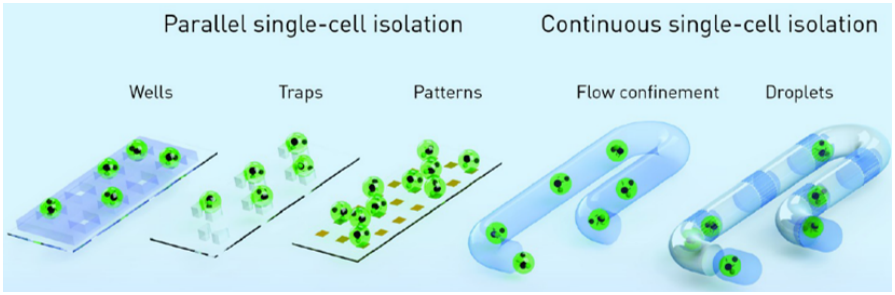

Figure 1.11 – Single cells can be isolate in parallel by wells, traps and patterns or continuously by flow confinement or droplets. Figure reproduced from [6] with permission from the American Chemical Society.

The parallel single-cell isolation can be done mechanically by physical boundaries such as well structures [54, 55, 56]. For micro-patterns the surface chemistry of the substrate is modified to make it cytophyllic (cell-friendly) or cytophobic (cell-repulsive) leading to the accumulation of the cells in the cytophyllic regions [57, 58, 59, 60]. A main advantage of this technique is that the cells can be easily supplied with nutrition or reagents. A further approach of isolation for SCA is trapping. Traps are categorized in mechanical, acoustic, magnetic, optical and dielectrophoretic traps [53]. For example, optical traps focus cells using a laser beam, the so-called optical tweezer [61]. The most common mechanical trap is the hydrodynamic trap, in which cells are immobilized in a side channel with a mechanical restriction [62]. Dielectrophoretic traps use non-uniform electric fields to exert forces on polarizable particles such as cells. According to the relative polarizability of the cells they are both pushed to and trapped at field maxima or minima [63]. The advantage over mechanical traps and well structures is that the trapping only depends on the application of the alternating electric field. When the signal is removed, the cells are released and are carried away with the flow. Studies have shown that short-term exposure has no effect on the survival, proliferation, or fate potential revealed by differentiation on neural stem cells and long time exposure mainly has an effect around the DEP cross-over frequency [64]. A more detailed explanation of DEP traps follows after the general explanation of the main principles of single-cell isolation. Yet another approach is to isolate cells by Quake valves [65]. Closing the valves completely isolates the cells in their micro-environment from the surround world. Opening the valve sets the cell free again. A disadvantage is that one cannot supply the cells with nutrition or exchange the medium while the valve is closed.

There is two major approaches to isolate cells in-flow by flow confinement and by droplets. The cells can then be investigated one after the other at a specific location in their flow path [6]. The separation of cells in low volume droplets (fL to nL) forming micro-environments is similar to micro-wells. The small volume facilitates analysis of single-cell secreted molecules [66, 67]. However, the exchange of the surrounding medium in droplets is hardly possible.

1.2.1 Dielectrophoretic trapping

In this thesis, we will used dielectrophoretic traps, to immobilize cells in special locations for consecutive analysis by electrorotation. In order to understand better the improvements of current systems by photolythographically fabricated three-dimensional electrodes, recent dielectrophoretic traps are presented.

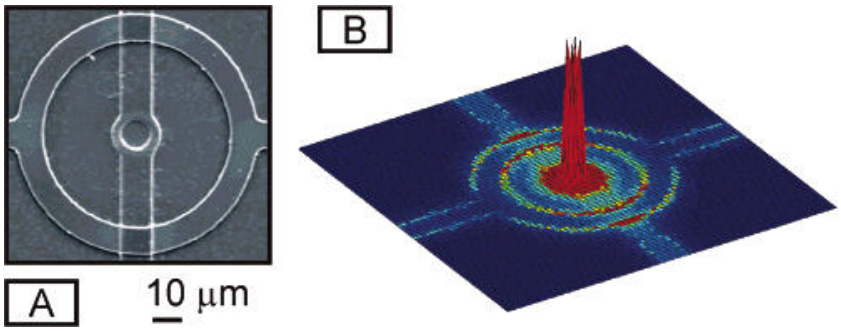

Figure 1.12 – The planar electrode structure (A) supplied with a positive and negative voltage creates a strong DEP force due to the high electric field gradient illustrated by the square of the magnitude of the electric field (B). Figure adapted from [68] with permission from the American Chemical Society.

DEP traps can be classified as positive dielectrophoretic (pDEP) and negative dielectrophoretic (nDEP) traps. Due to the maximal possible Clausius-Mossotti factor of +1 pDEP traps can be stronger then nDEP traps, whose minimal Clausius-Mossotti factor can only be -0.5. Since the electric field at the surface of the electrodes is always the highest and it usually diverges with the distance to the electrodes surface, pDEP traps, trap cells at the electrode surface. pDEP traps are used to array cells on the surface of a microfluidic chip [68], as shown in Fig. 1.12.

The structure consists of two arrays of signal lines, which are intersecting perpendicularly on the chip. The negative signal line is surrounding shaped in a large circle, when crossing the positive signal line. The positive line as well makes a small circle, at the middle of the intersection, as shown in Fig. 1.12 A. This creates a large pDEP holding force, as illustrated by the square of the magnitude of the electric field shown in Fig. 1.12 B. This structure allows to individually control the release from each trap, since the cells are released only if both signal lines are put to ground, as shown in Fig. 1.13.

In pDEP traps, the cells are immobilized on the electrode surface. This condition has two main disadvantages: (i) cells get in direct contact with the metal and (ii) the electric field is the highest in these regions. Conversely, nDEP traps trap cells away from surfaces at the areas of local electric field minima. nDEP trapping is often preferable to pDEP since it minimizes deleterious effects on the cell function or the viability since it pushes the cells away from hazardous high field strength regions [7]. One example is the dynamic array cytometer [69], developed by Joel Voldman *et al.*, shown in Fig. 1.14, in which they use three dimensional electrodes in a microfluidic channel to trap beads using nDEP. The beads can be individually

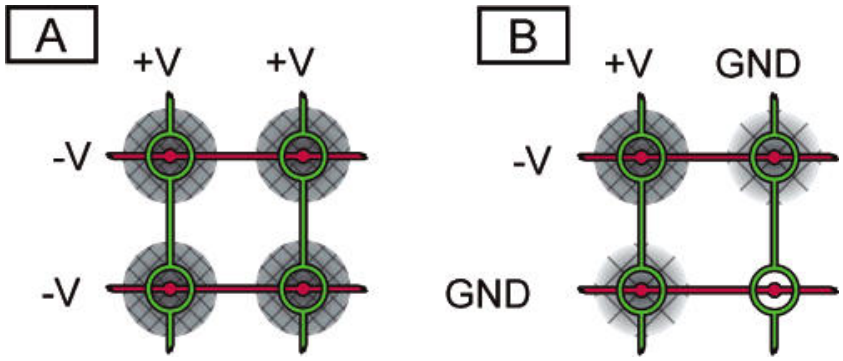

Figure 1.13 – The intersecting signal lines of the pDEP trap, create the DEP signal to trap cell (A). When both signal lines are put to ground, there is no trapping force (B) and the trapped cell is released. Figure reproduced from [68] with permission from the American Chemical Society.

released by switching off the signal at one electrode. This is a nice feature, which allows individual control of the trapping. However, the asymmetry of the array only allows trapping between every second pair of electrodes.

Trapping and label-free analysis of cells by electrorotation is not possible in that device, since the trapezoidal structure does not allow creating a consistently rotating electric field by 90° phase shifting the applied sinusoidal signals. Moreover, the common connection between two electrodes of each quadrupole forces them on the exact same signal, a configuration that allows DEP trapping, but not electrorotation.

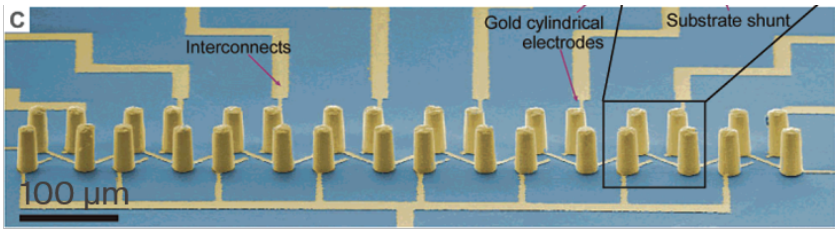

Figure 1.14 – The three-dimensional electrodes are placed within a microfluidic channel and connected with underlying signal lines. The signal of every second electrode can be individually controlled. Figure reproduced from [69] with permission from the American Chemical Society.

Another system, providing individual control of the cell handling was developed by *Silicon Biosystems s.r.l.* [70]. They use a chessboard pattern of electrodes at the bottom of a microfluidic chip in order to create a potential cage, in which cells or micro beads are trapped by nDEP, as shown in Fig. 1.15. Applying the signal to the neighboring electrodes allows to move around the cells and beads on the chip only using dielectrophoretic forces. However, the force exerted on the cells and beads varies, depending on the height at which they are in the channel.

All the presented systems can trap and control single cells in an arrayed or patterned way,

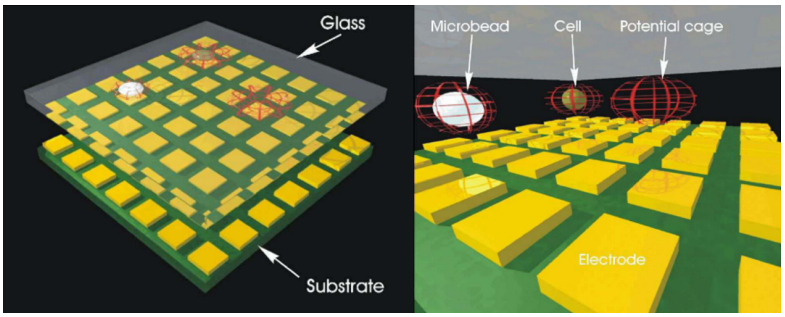

Figure 1.15 – Electric field cages are created by electrodes patterned at the bottom of a microfluidic chamber. Changing the applied configuration, beads and cells can be moved around in the chamber. Figure adapted from [70] with permission from IEEE.

however, none of them can trap cells against the flow and analyze them by electrorotation.

1.3 Non destructive time-resolved single-cell analysis

A good overview about destructive and non destructive single-cell analysis techniques is given by [6].

SCA referees to the analysis and the extraction of information from a single cell. A major technology is single-cell genomics [6], in which single cells are separated as described previously and usually PCR based analyzed. This technology reveals the genomic information of the cell, however, it is a one shot analysis technique, since the cell is destroyed in the process.

In this section, we are focusing on non destructive single cell analysis technologies which can retain cells over time and therefore enable continuous analysis and the potential for further downstream analysis. Therefore only properties which can be read out by an external signal triggered by the cell can be used.

In my opinion three cell properties in which we should classify are:

- optical properties
- mechanical properties
- electrical properties

In the following we will discuss possibilities to observe these cell properties and show how they can be used to give insights about the cells state or to distinguish them.

1.3.1 Based on optical properties

As other materials, cells have optical properties, they reflect and absorb light. The simplest case of optical analysis is the observation of cells under the microscope. However, one can reveal more information about the cell composition and therefore its state or about the interaction of its surface markers with a surface by analysing reflected or emitted light from the cell.

One example is surface plasmon resonance (SPR), in which light is falling on a surface, on which bio particle can be immobilized. The reflected light from the surface is recorded and analyzed. Depending on the surface plasmons, traveling charge density waves associated with the propagation of the electromagnetic field on a surface, which are created or absorbed on the surface, the reflected signal differs. It can observe changes in the angle of reflection, the wavelength, the intensity, the phase or the polarization of the reflected light [71, 72]. The modes of these plasmons depend on the material of the surface, as well as on binding of specific bio particles to the surface. The binding of single cells to the surface and therefore their specific interaction can be observed over time and evaluated [73]. Even this technology is not directly measuring the optical properties of the cell, it is an important optical SCA method an is therefore mentioned here.

Another method to analyze single cells by their optical properties is by Raman spectroscopy [74, 75, 76, 77]. It observes the vibrational, rotational and other low frequency modes and can be applied to single cell analysis [78]. A monochromatic light beam, as well called Raman excitation, is focused on the sample. This light interacts with the sample and vibrations, phonons or modes are excited or absorbed. The reflected light is detected and analyzed.

Raman spectroscopy of single cells

Casabella *et al.* [75] recently showed a setup which can automatically trap single cells optically, using a laser beam at a wavelength of $1064nm$. With this beam they localize cells in a microfluidic flow chamber. At the same time a Raman excitation of $532nm$ is exposed to the cell and the scattered Raman signal is recorded, which is less energetic than the original signal and therefore has wavelengths of $> 532nm$. A sketch of the setup is shown in Fig. 1.16 (a). Using this method, they can record multiple cell lines in an automated way. They can discriminate two cell lines, epithelial prostate cells and lymphocytes based on their Raman spectra, as shown in Fig. 1.16(b).

1.3.2 Based on mechanical properties

The mechanical cell properties vary between different cell lines as well as within a specific cell population, as we already mentioned in the section commenting on population sorting, where the deformability of cells was used to distinguished between cells in different states. The technologies deforming single cells in-flow and analyzing them [25, 26, 27, 28, 29, 30, 29] are actually single-cell analysis techniques, which were pushed to a level, on which complete

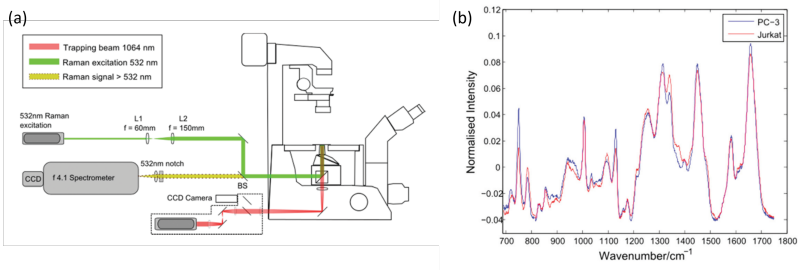

Figure 1.16 – Flowing a cell through a microfluidic channel placed on suspended. Figure adapted from [75] with permission from The Royal Society of Chemistry.

populations could be sorted.

Another technique analyzing the mechanical properties of cells, their molecular interaction with surfaces, as well as the real time monitoring of the cellular extraction is atomic force microscopy [79, 80, 81].

Koo *et al.* [79] used a hybrid binding domain-tethered tip to quantify the copy number of microRNAs on a single neuron and found that the number is increased upon cell activation.

Ruggeri *et al.* [80] showed with a label-free nanomotion sensor, which is basically an AFM, the cytotoxic effect of amyloids on single neuroblastoma cells, since the cellular membrane integrity is lost.

Guillaume-Gentil *et al.* [81] use an AFM to repetitively extract soluble molecules from the cell cytoplasm. Even if this technology is at the border to an invasive technology, its potential for single cells analysis is very high.

Besides the deformability and the interaction of the cell with surfaces, its buoyant mass can be used to monitor the growth of single cells of different cell lines [82]. In the following subsection, we will present this system which was developed by the Manalis group at MIT.

Cell distinguishing based on buoyant mass

A microfluidic channel is placed on an expended cantilever [82, 83], as shown in Fig. 1.17(a). This cantilever is oscillating with a specific resonance frequency. Cells are flown through the microfluidic channel on the cantilever. Depending on the position of the cell on the cantilever, the resonance frequency is changing, as shown in Fig. 1.17(b). The change in the resonance frequency when the particle is in the middle of the resonator is directly proportional to the particles buoyant mass. Optimizing a single cantilever, they could get a throughput of up to 2000 particles/min and with a parallelized setup of 16 resonators, they claim an approximate throughput of 6800 particles/min [83].

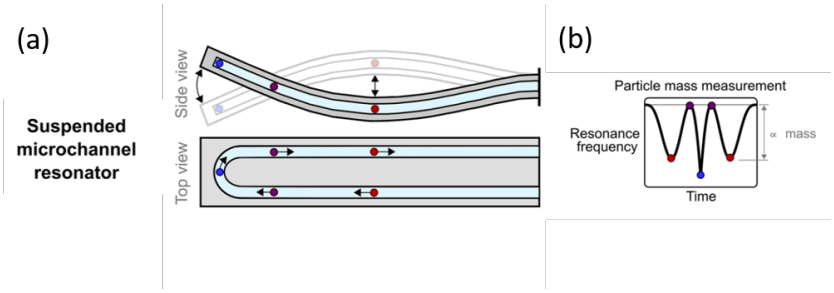

Figure 1.17 – Flowing a cell through a microfluidic channel, which is place on suspended cantilever (a), the resonance frequency of the cantilever changes (b) and the change in the resonance frequency is proportional to the cells buoyant mass. Figure adapted from [83] with permission from AIP Publishing.

1.3.3 Based on electrical properties

Another method to analyze single cells is based on their electric or more precisely dielectric properties. In order to access the dielectric properties of single cells, two approaches can be employed, namely, impedance spectroscopy and electrokinetic techniques, the latter are dielectrophoresis and electrorotation. These technologies have been employed for the label-feel sorting and characterization of cells [84, 85, 86]. The dielectric properties of the cell membrane, the cytoplasm or even the nucleus reflect the biophysics of the cell. It can give indication about the membrane morphology, the opening of ion channels, the intracellular ion flow, the cytoplasm conductivity and even the size of the nucleus [10]. Dielectric properties can be used to distinguish cell populations [87, 88] and cell sub populations [34, 89].

Electrorotation can be used to investigate the cells inherent parameters such as the cytoplasm conductivity [89] and the membrane capacitance [90]. A single cell or a cell population are positioned in a rotating electric field. The cell polarizes and, due to the rotation of the electric field, a torque acts on the cell leading it to rotate. Depending on the frequency of the applied electric field, the speed of rotation of the cells changes and is usually recorded by a bright field camera [63] or by an optical sensor [91]. Fitting the recorded rotational speed spectra to the so called single-shell model, one can find the dielectric properties of the cells.

Using this technology, different cell lines can be distinguished [88] or sub populations of one cell, for example when cells were modified by an electric impulse, making the cell membrane permeable [92], transfectants of cells [93], differences within a cell population due to the surrounding osmolarity [89] or cells treated by heat [94], could be recorded. A more detailed overview of recent electrorotation systems will be presented after the explanation of impedance spectroscopy.

In impedance spectroscopy an electric field is applied over a bio particle at different frequencies and the complex resistance is measured. Combining impedance spectroscopy using microelectrodes with hydrodynamic traps, allows to monitor the dielectric properties of cells over time [95, 96, 97, 98, 99, 100, 101].

Impedance spectroscopy can asses the cell viability and survival [102, 103, 104], cytotoxicity [105, 106], and cell growth [107, 108]. Within a population cell differentiation can be monitored [109, 110] or, as demonstrated by our group, the activation of T lymphocytes [34].

In the following, we will present one of these systems that can trap single cells and monitor their growth over time.

Single-cell impedance spectroscopy

Using two parallel microfluidic channels with integrated microfluidic traps in between, single cells can be hydrodynamically trapped and kept in culture over time [99]. A second inlet can supply the cells with fresh medium and therefore nutrition, which they need to continue growing. Using a stimulating electrode in the cell-culturing channel and a recording electrode behind the hydrodynamic trap, as shown in Fig. 1.18(a), the impedance signal of a single cell in culture can be recorded over time [100]. As shown in Fig. 1.18(b), the relative magnitude of the signal at $1MHz$ is directly anti-proportional to the cell length. Growth of the cells could continuously be monitored over several hours.

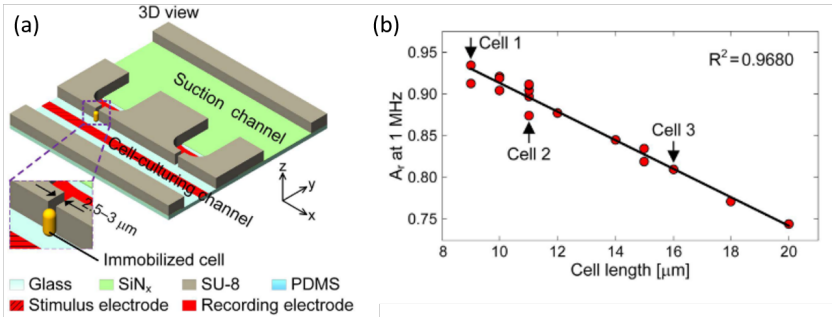

Figure 1.18 – (a) Single cells are hydrodynamically trapped between a cell-culturing and a suction channel, a stimulus electrode is patterned in the cell-culturing channel and an individual recording electrode behind each trap. (b) The relative magnitude of the impedance signal at $1MHz$ is directly anti-proportional to the cell length. Figure adapted from [100] with permission from Springer Nature.

Electrorotation

Dielectrophoresis analysis is normally used to separate cell populations. Additionally, fitting the response of the population at different frequencies of the electric field to the underlying model of the Clausius-Mossotti factor, the averaged dielectric properties of a complete cell population [111, 112, 113], as well as bacteria populations [114], can be obtained. Electrorotation places cells in rotating electric fields [115, 116] and observes the response of individual cells. It can be used to extract the specific membrane capacitance, the cytoplasm conductivity and the cytoplasm permittivity of cells. Compared to dielectrophoresis, electrorotation is more suitable to analyze the electric properties of a single cell, since it remains at a certain

position within the electric field and rotates [117]. It can be used to investigate changes in the cell membrane morphology [118, 119], induced apoptosis [120], changes in the membrane capacitance due to temperature, which determine the transformation of the cell [121]. The cytoplasm properties of cells can be investigated using electrorotation at higher excitation frequencies [122, 90]. The mentioned examples, mainly from the Gascoyne group, use electrorotation on populations of cells located together in chambers in absence of flow and therefore suffer from low parallel and noncontinuous operation.

Integrating electrorotation systems in microfluidic channels allows a successive injection of reagents to the location of the cells, however the cells have to be positioned in the area foreseen for the electrorotation and potentially kept there against flow.

One technology to position cells at a specific position during electrorotation analysis uses laser tweezers. These have already been used to keep cells in place in large electrorotation chambers [123, 124, 93]. Maintaining a constant position of the cells is crucial to keep the torque acting on the cell constant, [125], since cells at different positions experience different torques. Laser tweezers can be used in microfluidic channels for in-flow single-cell electrorotation too [124], as shown in Fig. 1.19, but suffer from low parallelization and require manual operation.

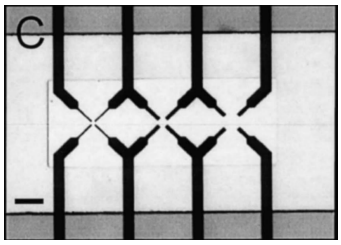

Figure 1.19 – Three octopoles of different inter-electrode distance are positioned along a microfluidic channel. Cells are investigated in the differently sized octopoles, in which they are positioned using a single laser tweezer. Figure adapted from [124] with permission from Elsevier.

Another approach is to trap the cells within a quadrupole using nDEP trapping. For this two approaches exist: in the first, nDEP signal and the electrorotation signal are alternated[94], as shown in Fig. 1.20 (a). For a fraction of a second the nDEP trapping signal is applied, followed by ROT signal, with a phase shift of 90° between the sinusoidal signals applied at neighboring electrodes. The trapping signal is applied for $20\mu s$ followed by $20\mu s$ of the rotation signal. Due to the fast alternation, the cell stays continuously trapped and rotating at the same time. The other option is to superpose the nDEP and the ROT signal [88, 92], as shown in Fig. 1.20 (b). The large amplitude signal centers the cell in the middle of the quadrupole/octopole and the superposed signal of smaller amplitude makes the cell rotate. Both methods allow to focus the cell by nDEP trapping in the middle of the quadrupole during the entire duration of the experiments. The neighboring electrodes have a phase shift of 180° creating an electrokinetic force towards the center of the quadrupole.

Using an octopole, which is built out of two slightly rotated quadrupoles, located at the top

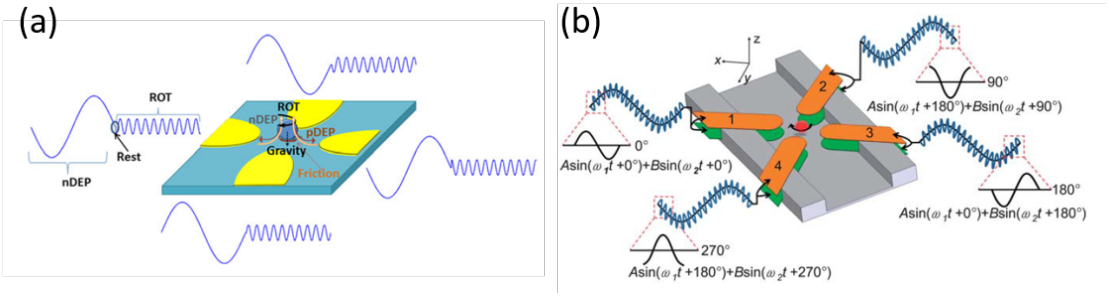

Figure 1.20 – In order to achieve simultaneous nDEP trapping and electrorotation, the applied DEP and ROT signals are either alternated (a) or superposed (b). Figure (a) reproduced from [94] with permission of John Wiley and Sons. Figure (b) reproduced from [88] with permission of the Royal Society of Chemistry.

and the bottom of the channel, allows to exert a rotational torque while trapping the particles and allows as well the electrorotation analysis [126].

These systems manage to operate electrorotation in flow, however they do not parallelize the analysis in single-cell electrorotation cages. The system built by Fuhr *et al.* [124], described in the previous paragraph, has three octopoles one after the other along a microfluidic channel and could therefore analyze three different cells at different positions in the channel or the same cell three times in different octopoles. However, parallel operation is not reported and the octopole of different size, as shown in 1.19, are clearly not built for parallel operation but to position the cell in the octopole that best matches its size.

To our knowledge, the parallel operation of electrorotation analysis in arrayed single-cell micro cages has not been demonstrated yet. Additionally, our system has the ability to selectively trap and release single cells and can therefore control their analysis and enable further cell handling.

1.4 Fabrication of three-dimensional electrodes and their advantage for dielectrophoresis

Due to the parabolic flow profile, the microfluidic drag force, which will be explained later on is the strongest in the middle of a microfluidic channel. Pairing microfluidics with electrokinetics, electrodes have to be integrated within microfluidic channels. Usually the strongest electric fields and the strongest electric field gradients appear on the interface to the electrodes. Using traditional planar electrodes on the bottom of a microfluidic channel, the electric field will be the strongest at the bottom of the channel and will decrease towards the top of the channel. Correspondingly a dielectrophoretic force will be the strongest at the bottom too.

In order to increase the throughput in microfluidic devices while keeping the footprint constant, the channel height has to be increased. The difference between the region of a strong

microfluidic drag force and a strong dielectrophoretic force becomes more dominant. Homogeneous electric fields over the complete channel height become desirable. One method to achieve this is by insulator based dielectrophoresis (iDEP). Researcher placed electrodes away from the active region of the devices, either at the device in- and outlets or the sides of the device. Due to the comparable long distance between the electrodes to the channel height, the electric field is in first approximation homogeneous in the vertical direction. This was for example used to concentrate bacteria in microfluidic restrictions [38, 127], to trap molecules or extracellular vesicles [128, 129], to concentrate cells in a microfluidic channel and form clusters [130] or to add dielectrophoretic forces to deterministic lateral displacement devices [47, 131]. However, in this approach much higher voltages are needed in order to create comparable electric fields, usually amplitudes in the order of kV are used for fields which could be created with our approach, which will be explain later on, using a few V.

Another approach to create a more homogeneous electric field would be to use top and bottom electrodes as done in the case of electrorotation for octopoles [126]. This has several advantages, for example is the cell trapped in the middle of the microfluidic channel, since a lateral force is applied to the cell too, focusing it to the middle of the microfluidic channel. However, using this layout for electrorotation experiments with an alternating dielectrophoretic trapping and electrorotation signal, this layout would need eight instead of four different signals, since the DEP signal has to be inverted from the bottom to the top electrode, while the electrorotation signal has to remain the same. The needed wiring increases the complexity of the system too. Additional the fabrication of these devices requires a manual alignment step of the top and the bottom layer. While precise methods exist for the alignment, it still needs manual alignment on a chip and not a wafer level. However, most importantly increasing the channel height of the device in order to increase the throughput, the electric field decreases in the middle of the microfluidic channel, where the drag force is the strongest. The top electrode reduces this effect, however the reduction of the electric field over the channel height still influences the device performance.

Especially for dielectrophoretic devices three dimensional electrodes provide the advantage, that they can provide a uniform electric field in z direction over the complete channel height [132]. These electrodes have advantages over planar electrodes, but go with sophisticated fabrication processes. First three dimensional electrodes haven been fabricated using electroplating [133, 134], then carbonating of SU-8 was used to fabricate conductive three dimensional structures [135]. However, the conductivity of these electrodes is quite high. Later, a mix between electroplating and etching was used to fabricate these structures [136], followed by metal ion implantation in PDMS [137] and electrodeless electroplating [138]. Lately insulating structures have been covered with metal sputtering and patterned by photolithography [139]. Our group has developed a fabrication process, in which three dimensional electrodes can be produced in any structure phototlithographically patterned in SU-8. Therefore SU-8 is patterned photolithographically and subsequently covered with metal by sputtering. The ejected atoms from the target in the gas phase are not in their thermodynamic equilibrium and will deposit on the wafer. Especially interesting is that the deposit as well on the wall of the SU-8

pillars. The sputtering is followed by directional ion beam etching, which allows to remove the planar covering of the metal but not the covering of the side walls [4]. The advantage of this process is that it can easily be combined with other microelectronic fabrication processes, as insulating metal lines in order to bring different electric signals everywhere on the wafer.

Due to the photolithographic precision of our fabrication process, we can fabricate three-dimensional electrodes with sharp edges which other fabrication methods are not able to.

These electrodes have so far been used for impedance spectroscopy [34], however, never for dielectropheretic applications. One of the main focuses of this thesis is to show the successful integration of these three-dimensional electrodes in dielectrophoretic devices in order to make a contribution to each of the three of particle separation, cell arraying and single-cell analysis mentioned before. This thesis shows, that the electrodes are functional and that they should be added to the toolkit of fabrication methods, from which researchers can serve themselves when designing new dielectrophoretic devices. Open questions are if the devices can be successfully built and if they are functional, as well as if they can support the increased currents compared to impedance measurements and if they function at lower voltages compared to iDEP devices.

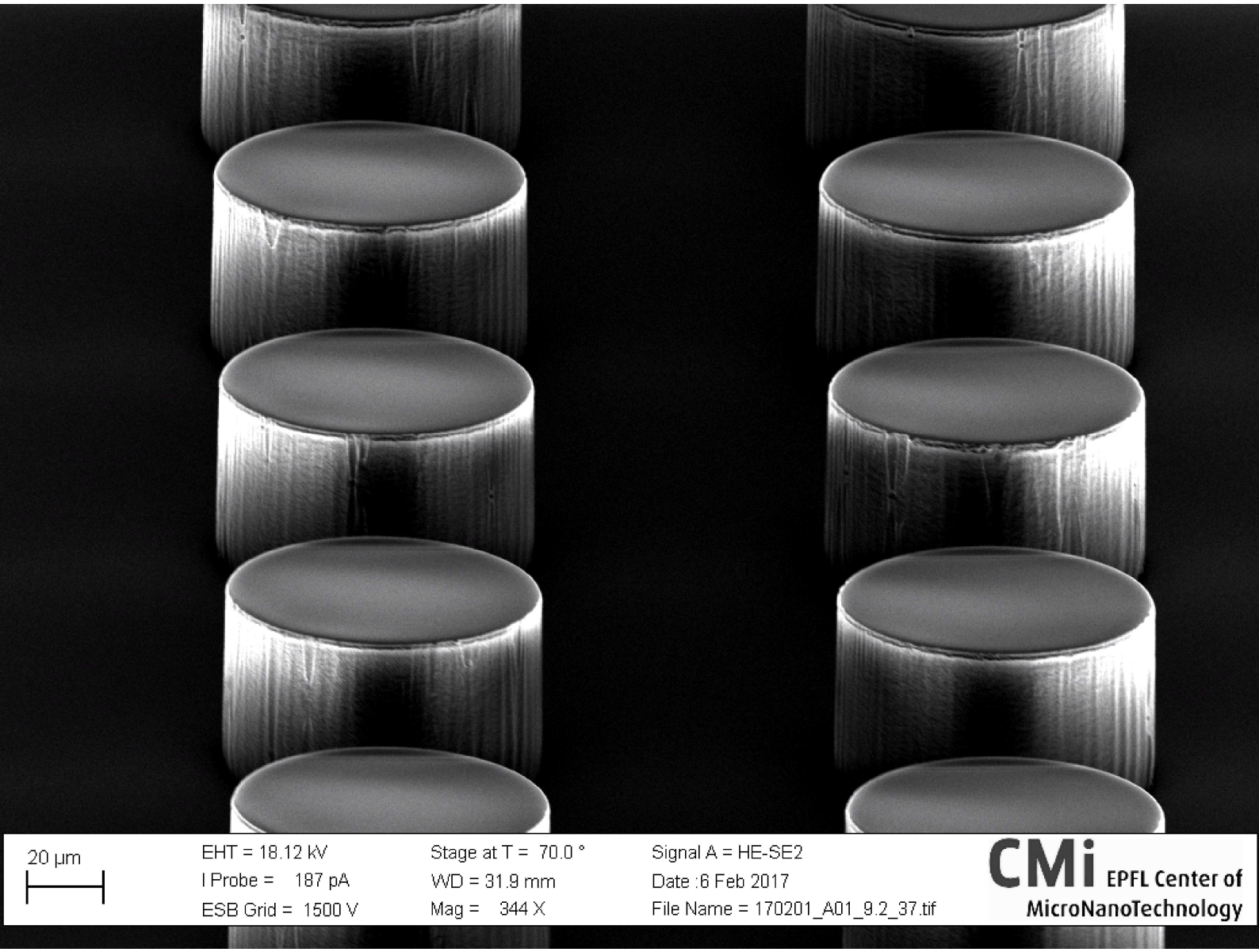
20 µm
EHT = 18.12 kV
I Probe = 187 pA
ESB Grid = 1500 V
Stage at T = 70.0 °
WD = 31.9 mm
Mag = 344 X
Signal A = HE-SE2
Date :6 Feb 2017
File Name = 170201_A01_9.2_37.tif
CMi EPFL Center of MicroNanoTechnology

CMi Picture of the Month February 2017: Micro-lego-brick

"These 3D electrodes were fabricated by covering SU-8 micro-pillars via metal sputtering. The metal on top and on the substrate was subsequently removed by ion beam etching. The irregular structure of the SU-8 below the metal breaks the symmetry of this artistic SEM micrograph. By increasing the contrast and observing under an angle of 70deg to the surface, the electrodes seem to appear out of nothing. This structure assembles a hundred times miniaturized lego-brick, fabricated and observed in EPFL CMi facilities."

2 Simulations of arrayed negative dielectrophoretic traps to optimize the trap size and experimental conditions

In this chapter, the finite element simulations to predict the trapping behavior of different cell types under varying conditions and chip design will be discussed.

First, a short summary about the theory of the dielectrophoretic force and the microfluidic drag force will be presented. Moreover, different models for the Clausius-Mossotti factor will be discussed.

Second, the simulated results will be discussed in detail. Five cell types are analyzed in different medium conductivities and at various electric field frequencies. For each cell type specific conditions are found, which enable the trapping of this type in the dielectrophoretic micro-cage array.

2.1 Theoretical background

In order to understand the following trap simulations, but as well for the experimental results presented in the following chapters, we present here briefly the principle of dielectrophoresis.

The Clausius-Mossotti factor is the main contribution to the dielectorophoretic force, besides determined device parameters like the electric field strength and the field gradient. It determines as well the speed of rotation of cells in rotating electric fields, which will be discussed in the next chapter. More simply, the Clausius-Mossotti factor is a measure of the polarization of a particle in the electric field compared to the surrounding medium. Two models are used in this thesis to describe the particles' Clausius-Mossotti factor, the homogeneous sphere and single-shell model.

After a description of dielectrophoresis, we will focus on the mechanical behavior of particles in microfluidic channels. In particular, we will briefly present the microfluidic drag forces acting on a particle in a flow.

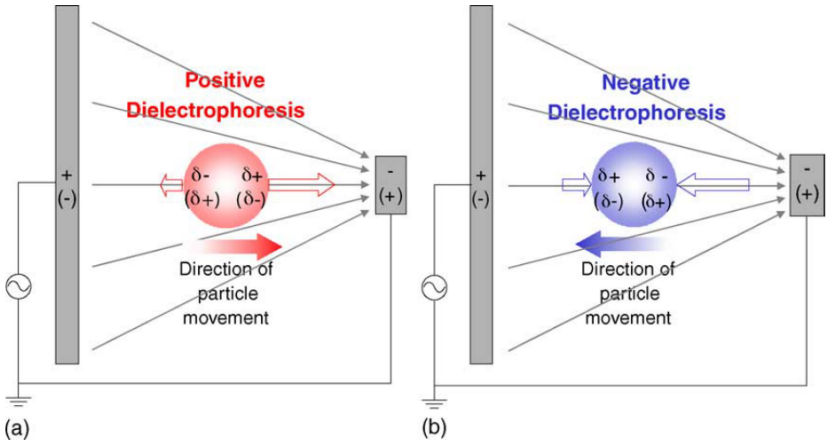

Figure 2.1 – Dielectrophoresis is a phenomenon in which a net neutral particle is getting polarized in a gradient electric field. If the particle is more polarizable than the surrounding medium, as shown in (a), it moves towards high field regions. If the particle is less polarizable than the surrounding medium, as shown in (b), it moves toward the low field region. Figure reproduced from [140] with permission of Elsevier.

2.1.1 Dielectrophoresis

Applying an electric field on an ionic solution, negative charges move to the positive pole, while positive charges move to the negative pole. This phenomenon is called electrophoresis and acts on charged particles. Uncharged particles do not experience a force in a uniform electric field.

However, particles with no overall net charge, but an internal charge distribution, like cells, are effected by electric fields too. While in an electric field, the cell polarizes, positive charges shift to one side of the cell, closer to the negative pole, while the negative charges shift to the other side, closer to the positive pole. The cell experiences forces from both charged regions. If the electric field remains homogeneous from one side of the cell to the other, the electrostatic forces balance out and no net force acts on the cell. If the particle is placed in a gradient electric field, the electric field at one side of the particle is stronger than on the opposite side. Since the particle has no net charge, the positive and negative charges are equal, but they accumulate according to the field and the net force on the particle arises. If the particle is more polarizable than the surrounding medium, it moves towards the high field region, as shown in Fig. 2.1(a). If the particle is less polarizable, the effect is inverted and the particle moves towards low field regions, as shown in Fig. 2.1(b).

In an alternating electric field (AC), static effects on net charges average out. However, the effect of dielectrophoresis, which depends on the polarizability and not the net charge, is still present [141, 115]. This allows to use dielectrophoresis as well for particles with a net charge; the only inherent parameter of the particle, in our case a cell, an extracellular vesicule or a bead is its polarizability.

The Clausius-Mossotti factor is a measure for the polarizablity of the particle in a specific surrounding medium. It is a complex number and has a real and an imaginary part, that can both range from -0.5 to +1.0. If its real part is positive, the particle is dragged toward high field regions (pDEP); if it is negative, the particle is dragged toward low field regions (nDEP). The dielectrophoretic force is described by [142]

$$\langle \mathbf{F}_{DEP} \rangle = \pi \epsilon_0 \epsilon_m R^3 Re[CM] \nabla E_{pk}^2 \tag{2.1}$$

where ϵ_0 is the absolute permittivity, ϵ_m is the relative permittivity of the medium, R is the particle radius, $Re[CM]$ is the real part of the Clausius-Mossotti factor and ∇E_{pk}^2 is the gradient of the square of the peak electric field.

2.1.2 Models for the Clausius-Mossotti factor

The Clausius-Mossotti factor enters linearly in the dielectrophoretic force (real part) and the electrorotation torque (imaginary part). It can vary between -0.5 and $+1$, depending on the particle's and the surrounding medium's dielectric properties, as well as on the frequency of the applied electric field. The sign of the real part of the Clausius-Mossotti factor determines whether a particle experiences negative or positive DEP, meaning if it is attracted toward higher or lower field regions. The value of this factor determines the strength of the force. In the case of pDEP, the maximal absolute value of the CM factor can be 1 and in the case of nDEP it can only be 0.5, positive dielectrophoresis can create stronger forces then negative dielectrophoresis.

The imaginary part determines if the particle rotates when placed in a rotating electric field. The rotation goes in the same direction when $Im[CM] < 0$, or in the opposite direction of the electric field when $Im[CM] > 0$.

There are different models for the Clausius-Mossotti factor, depending on the particle and its composition. In this thesis, we use two different models. The homogeneous sphere model, where the particle is modeled as a sphere made out of a single material. We use this model for latex beads. The other model is the single-shell model, in which a homogeneous material, as for example the cells cytoplasm, is surrounded by a shell, for instance the cell membrane. This model is used to model cells and extracellular vesicles.

In any model, the Clausius-Mossotti factor is given by [143]

$$CM = \frac{\epsilon_p^* - \epsilon_p^*}{\epsilon_p^* + 2\epsilon_m^*} \tag{2.2}$$

with ϵ_p^* and ϵ_m^* being the particles and the medium complex permittivity , where ϵ^* is defined as $\epsilon^* = \epsilon - j\frac{\sigma}{\omega}$. ϵ is the permittivity, σ is the conductivity and ω is the angular frequency of the applied electric field.

For the surrounding medium, one can simply use the literature values of the permittivity and the conductivity, while the complex permittivity of the particle depends on the underlying model, in our cases the homogeneous sphere and the single-shell model.

Homogeneous sphere model

The simplest model for a spherical particle in suspension is the homogeneous sphere model. The permittivity ϵ_p can simply be assumed to be the literature value of the bulk material properties.

However, the conductivity of the sphere is not only the bulk conductivity of the material. The surface conductance of the particles significantly influences the total conductivity of the particle σ_p. The smaller the particle, the higher the influence of the surface conductance on the total conductivity of the particle [144, 145, 146, 147].

The total conductivity of the particle can be described by

$$\sigma_p = \sigma_{p,bulk} + \frac{2K_S}{R} \tag{2.3}$$

with $\sigma_{p,bulk}$ the bulk conductivity of the material, K_S the surface conductance and R the particle radius. This model is based on the assumption that the particles we are working with have a significant small volume-to-surface ratio and that the charges on the surface of the particles contribute to the overall particle conductivity. This model is in our case sufficient to model the behavior of latex beads.

Single-shell model

For the single-shell model, one assumes the cell to be built out of a cell membrane and cytoplasm only, which are both homogeneous materials with inherent dielectric properties.

The Clausius-Mossotti factor is based on the same relation between the particle and the surrounding medium as in Eq. 2.2. However, instead of replacing the particles complex permittivity by a simple permittivity and conductivity, one takes into account the model of a sphere surrounded by a shell, as shown in Fig. 2.2, which is given by [90]

$$\epsilon_p^* = \epsilon_{mem}^* \frac{[(R+d)/R]^3 + 2[(\epsilon_{cyto^*} - \epsilon_{mem}^*)/(\epsilon_{cyto}^* + 2\epsilon_{mem}^2)]}{[(R+d)/R]^3 - [(\epsilon_{cyto}^* - \epsilon_{mem}^*)/(\epsilon_{cyto}^* + 2\epsilon_{mem}^*)]} \tag{2.4}$$

with the complex membrane permittivity ϵ_{mem}^* and complex cytoplasm permittivity ϵ_{cyto}^*, as well as the membrane thickness d.

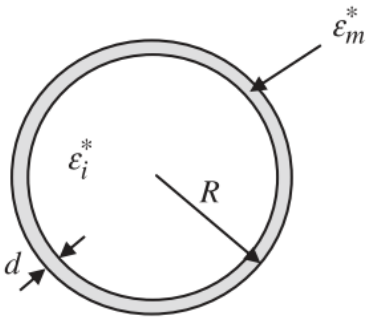

Figure 2.2 – The single-shell model assumes a particle to consist out of a homogeneous sphere surrounded by a homogeneous shell. Figure reproduced from [142] with permission from John Wiley and Sons.

Under the condition $d << R$, one can simplify this equation to [90]

$$\epsilon_p^* = C_{mem}^* \frac{3R\epsilon_{cyto}^*}{3\epsilon cyto^* + 3C_{mem}^* R} \tag{2.5}$$

with the complex membrane capacitance $C_{mem}^* = C_{mem} - j\frac{G_{mem}}{\omega}$ from the membrane capacitance C_{mem} and the membrane conductance G_{mem}.

The membrane conductance is defined as [142]

$$G_{mem} = \frac{A\sigma_{mem}}{d} \tag{2.6}$$

and the membrane capacitance is defined as

$$C_{mem} = \frac{A\epsilon_0\epsilon_{mem}}{d} \tag{2.7}$$

with the particles surface A.

2.1.3 Microfluidic drag force

In this thesis, we use AC electrokinetic forces to manipulate particles in microfluidic channels. However, the particles are always subjected to the mechanical forces exerted on them by the surrounding fluid. The most important is the drag force which takes into account the stream of the fluid in which the particle is located. The drag force acting on the particle is given by [111, 148]

$$F_{drag} = 6\pi\eta R\upsilon \tag{2.8}$$

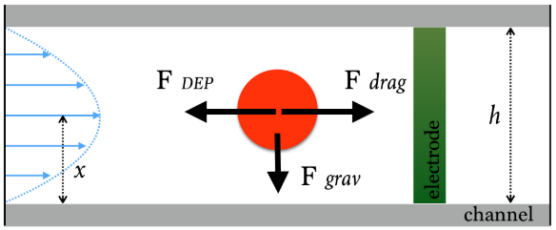

Figure 2.3 – The flow profile as well as the forces acting on a particle in a microfluidic channel. Figure reproduced from [149] with permission from Marta Comino.

with the fluid viscosity η, the particle radius R and the far-field relative velocity of the liquid v, relative to the particle.

This equation remains valid, as long as there is laminar flow, so in absence of turbulence. This is the case for low Reynolds numbers (Re), e.g. where $Re << 1$. In this case, the Navier-Stokes equation can be simplified, since there is negligible inertia of the particle.

Assuming a rectangular channel much wider than high, the flow can be approximated as one-dimensional. The flow profile is parabolic, as illustrated in Fig. 2.3, and the relative velocity of the particle in the channel, depends only on the height of the channel h and on the particle position x [148]

$$v = -6 < v > \frac{x}{h}\left(1 - \frac{x}{h}\right) \tag{2.9}$$

$< v >$ is the mean velocity of the flow given by

$$< v >= \frac{V}{wh} \tag{2.10}$$

with the nominal flow rate V and the width of the channel w.

2.2 Simulations of the DEP trapping

In order to find the optimal trap dimension for each specific cell type, as well as the correct experimental conditions to trap reliably, we performed finite element simulations using COMSOL Multiphysics. Different trap sizes, in which the size of the electrodes is always equal to the size of the trap, are tested. The trap configuration, which keeps a low entrance barrier generated by a $1V$ amplitude signal and an higher exit barrier by a $5V$ amplitude signal is maintained in all simulations.

The medium conductivity, the microfluidic flow and the frequency of the electric field are swept in order to find the optimal conditions for trapping.

One finding, which is later confirmed by the experiments, is that even if the Clausius-Mossotti factor due to the medium conductivity and the applied electric field frequency are very similar, some cell types are getting trapped in the array, while others are not. Since the dielectrophoretic force depends on the third power on the radius of the particle, smaller particles experience a much smaller trapping force.

The main finding of the simulations are to show how to find the optimal conditions to trap a specific cell type. The parameters such as medium conductivity, electric field frequency, trap size and pressure difference are tuned for each cell type. The findings from the simulations were used in order to trap cell types, especially human immortalized T lymphocytes, which previously could not be trapped due to non-optimized experimental conditions. Using the optimized parameters from the simulations presented, trapping of these cell type could be achieved and the cells electrorotation spectra could be acquired.

Our proceeding from the COMSOL conference held in Lausanne in 2018 with the title "Trapping of Single-Cells Within 3D Electrokinetic Cages" (Kevin Keim, António Gonçalves, Carlotta Guiducci)[150] explains in detail the trapping conditions for the different cell types.

The values used for the dielectric properties of the cells slightly vary from the ones found by our own experiments later on [151], however the general understanding of the influence of the cells dielectric parameters and size remains the same.

Contributions

Kevin Keim implemented the microfluidic structures and the forces in the COMSOL model. After some first proofs of principle simulations, António Gonçalves, ran the simulations at the different conditions during a semester project (228 hours), supervised by Kevin Keim and Carlotta Guiducci. The post-processing of the simulations to illustrate the results was done by Kevin Keim and António Gonçalves. Carlotta Guiducci, António Gonçalves and Kevin Keim analysed the results. The first draft of the manuscript was written by Kevin Keim with the support of António Gonçalves. All author edited and approved the manuscript.

Trapping of Single-Cells Within 3D Electrokinetic Cages

Kevin Keim[1], António Gonçalves[1], Carlotta Guiducci[1]

1. École Polytechnique Fédérale de Lausanne - Laboratory of Life Sciences Electronics (Guiducci Lab), Station 17 CH-1015 Lausanne, Switzerland

Introduction

Single-cell analysis (SCA) refers to the analysis of single cells in a sample instead of average measurements of the cells ensemble. Bulk experiments might lead to misleading interpretations, while observing a single cell gives indications about the specific cell phenotype [1]. Cell populations, especially of diseased cells, are heterogeneous. SCA of cell populations can finely describe their heterogeneity and identify minorities [2].

In order to observe a single cell, the clone has to be taken from the bulk and isolated. SCA becomes especially meaningful, if many single-cells can be observed concomitantly over time [3]. Therefore, methods were developed to array single-cells in order to investigate them in a simultaneous manner. Microwells, patterns or single-cell traps are examples to immobilize cells at fixed locations on a surface [4]. Negative dielectrophoretic (nDEP) traps can capture cells at electric field minima in suspension [5], [6].

For nDEP traps, three-dimensional electrodes are advantageous, since they create homogeneous electric fields and therefore create an equal trapping force over the complete height of a microfluidic channel, when placed within. Our group has recently developed a fabrication process, with which we can fabricate three-dimensional electrodes of any shape and high aspect ratio [7], a SEM micrograph of these electrodes is shown in Fig. 1. These electrodes have already been used for in flow impedance measurements, electrorotation and deterministic lateral displacement devices with implemented DEP fine tuning [8]–[10]. Now, we want to use these electrodes for nDEP trapping devices. We fabricated two arrays of three-dimensional electrodes and apply AC electric fields of different amplitudes between the first row of electrodes and the second row. These creates two dielectric barriers, a first, lower entry barrier and a second higher exit barrier. Cells are supposed to overcome the first barrier and get trapped at the second barrier, so we can perform analysis on these arrayed and separated single cells. In order to find the correct trap dimensions and experimental conditions, we perform finite elements simulations, using COMSOL Multiphysics®.

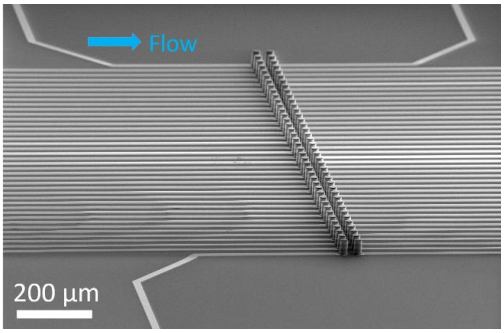

Figure 1. SEM micrograph of an array of 3D electrodes.

Theory

Dielectrophoresis is a phenomenon, in which polarizable particles experience a force in inhomogeneous electric field. The electric field polarizes the particles and the charges within the particles are dislocated. Due to the inhomogeneity, the electric field at one side of the particle is higher than at the other side. Consequently, one electrostatic force is stronger than the other and a net force is exerted on the particle. The dielectrophoretic force is given by [11]

$$\langle \mathbf{F}_{\mathrm{DEP}} \rangle = \pi \varepsilon_0 \varepsilon_m \mathrm{R}^3 Re[\mathrm{CM}] \nabla E_{pk}^2 \quad (1)$$

ε_0 is the absolute and ε_m is the relative permittivity of the medium; R is the cell radius and *Re*[CM] is the real part of the Clausius-Mossotti (CM) factor, which depends on the dielectric properties of the cell and the surrounding medium. ∇E_{pk}^2 is the gradient of the peak electric field.

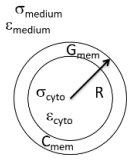

Figure 2. Illustration of the single-shell model used in the simulations.

In an AC electric field, the effects of the net charge of the particle cancels out and only the polarizability of the particle matters. However, the polarizability depends on the particle and the surrounding medium and is reflected in the CM factor. If the particle is more polarizable then the surrounding medium, it will move towards high field regions and one talks of positive DEP (pDEP). If it is less polarizable than the surrounding medium, it will move toward lower field region, called nDEP. This is reflected in the real part of

the CM factor for the single shell model, illustrated in Fig. 2, given by

$$\mathrm{CM} = \frac{\tilde{\varepsilon}_p - \tilde{\varepsilon}_m}{\tilde{\varepsilon}_p + 2\tilde{\varepsilon}_m}; \quad \tilde{\varepsilon}_p = \tilde{C}_{mem}\frac{3R\tilde{\varepsilon}_{cyto}}{3\tilde{\varepsilon}_{cyto} + 3\tilde{C}_{mem}R} \qquad (2)$$

$\tilde{\varepsilon}_p$, $\tilde{\varepsilon}_m$, $\tilde{\varepsilon}_{cyto}$ are the complex permittivity of the particle, the suspending medium and the cytoplasm, defined as: $\tilde{\varepsilon} = \varepsilon - \frac{i\sigma}{\omega}$ and $\tilde{C}_{mem}$ is the complex membrane capacitance defined as $\tilde{C} = C - \frac{iG}{\omega}$ with G the membrane conductance [12].

Besides the DEP force, another force is acting on the cells simultaneously, while in the microfluidic channel.

$$\langle \boldsymbol{F}_{drag} \rangle = -6\pi\eta R\boldsymbol{v} \qquad (3)$$

Is the microfluidic drag force, which depends on the medium viscosity η, the particle radius R and the velocity of the fluid $\boldsymbol{v}$. A cell can be trapped in suspension if there is no net force acting on it, so if Eq. 1 and Eq. 2 are equal and there is no initial velocity of the cell. A possibility to create this is by applying a specific voltage at the electrode arrays, which create dielectric barriers and exert a force, which compensates the drag force, as shown in Fig. 3.

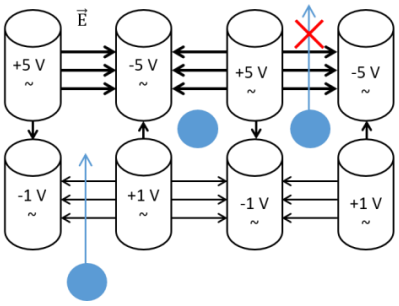

Figure 3. Cells trapped in an electrodes array with two different dielectric barriers. The cell (left) overcomes the first dielectric barrier due to the microfluidic drag force, but cannot overcome the second barrier (right) and is trapped in the array.

Methods

Finite elements simulations forecast the trajectory of cells in certain electrode geometries and experimental conditions. We create a cuboid of 400 µm per 400 µm per 50 µm of the electrode configuration, by creating a working plane of 400 µm per 400 µm and implementing the ground plane of the electrode (diameter and inter electrode distance of 20 µm, 40 µm and 80 µm) configuration. Subsequently we extrude this plane by 50 µm. Next, we introduce the electric current and laminar flow physics. The properties of water are given to the active volume of the device. We create a fluid inlet at one side, by applying a pressure between 0.01 mbar and 1 mbar and creating an outlet of 0 mbar at the opposite side.

We assign an alternating electric potential of -1V and +1V to the upstream and of -5V and +5V at the downstream electrodes. In a first stationary study we solve the laminar flow and electric current equations. The results are illustrated in the plot of the pressure and fluid streamlines, shown in Fig. 3, and in the plot of the absolute value of the electric field and the electric field lines, shown in Fig. 4.

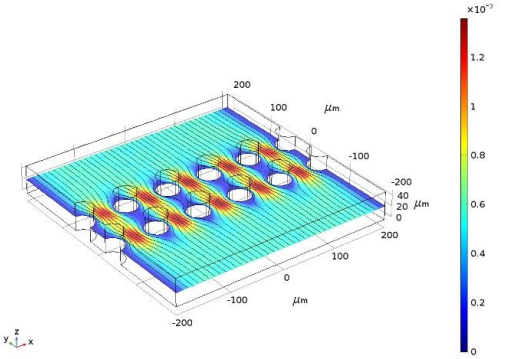

Figure 4. Illustration of the simulated pressure and the fluid flow streamlines in the 3D electrode array.

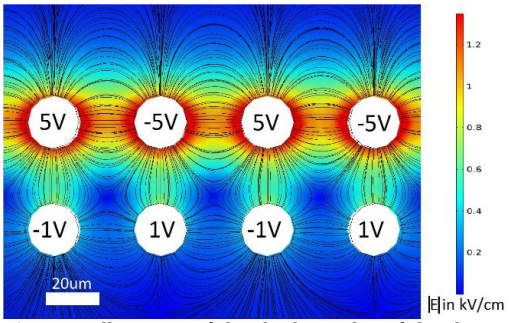

Figure 5. Illustration of the absolute value of the electric field and the electric field lines.

Using the results of the first stationary study, we compute a time dependent study, analyzing the cells trajectory, with the particle tracing for fluid flow module. We create a particle inlet at the same boundary as the fluid inlet and a particle outlet at the fluid outlet. At t = 0 s we release twenty solid particles at a density based position in the channel with the initial velocity based on based on the velocity field, previously calculated. The forces acting on the particles are set to be the fluid drag force, as given in

Eq. 2, which is already implemented in COMSOL® and the dielectric force, given by Eq.1, which we implemented ourselves in order to be able to use the CM factor, based on the complex membrane capacitance, shown in Eq. 3.

We performed this study sweeping the conductivity of the surrounding medium between 1m S/m and 1000 mS/m, as well as the electric field frequencies between 100 kHz and 10 MHz for human T lymphocytes, A549, M17 neuroblastoma, HEK 293 and HeLa cells. The dielectric parameters used for these cells are given in Table 1. After the simulations the trajectory and the final position of the cells are illustrated in the three-dimensional space and a statement about the functionality of the trapping in the given conditions can be made.

	C_{mem}	G_{mem}	R	σ_{cyto}	ε_{cyto}	Ref
T lymphocytes	7.01 mF/m^2	1345 S/m^2	3.6 µm	0.53 S/m	100	[13]
A549	16.95 mF/m^2	1345 S/m^2	3.45 µm	0.23 S/m	100	[13]
M17	16.95 mF/m^2	800 S/m^2	6.9 µm	0.23 S/m	100	[14]
HEK 293	7.94 mF/m^2	0	6.5 µm	0.408 S/m	85	[15]
HeLa	19.9 mF/m^2	0	10.5 µm	0.32 S/m	85	[16], [17]

Table 1: Dielectric parameters of the cells used in the simulations.

Results and Discussion

We performed this finite element study in order to find the experimental parameters and geometries to trap cells in the electrode array in order to perform subsequently electrorotation experiments with them. In what follows we present the parameters we tuned to achieve efficient DEP trapping.

1. Effect of the medium conductivity and the electric field frequency on the trapping efficiency

In order to find the correct trapping conditions, first the dielectrophoretic force has to be negative, since we want to trap the cells in suspension within the electrode array. To find the DEP force, given in Eq. 1, negative, the CM factor, given in Eq. 3, has to be negative. To ensure the correct values of this factor within COMSOL®, we plot this factor for the different cell values given in Table 1. The CM factor, depending on the frequency of the AC electric field for each cell at a medium conductivity of 100 mS/m, is shown in Fig. 6. The CM factor is plotted in COMSOL Multiphysics©, and ensures therefore the correct value for the simulations.

Different cells experience different DEP forces, depending on their CM factors. In the experiments, we used a medium conductivity of 100 mS/m, since the imaginary part of the CM factor needs to be negative, in order to have trapping, but the real part has to be distinct in order to extract the cells dielectric parameters by electrorotation [18].

The CM factor depends strongly on the medium conductivity, as shown in Fig. 7. In order to achieve nDEP for T lymphocytes, the medium conductivity cannot be set below 10 mS/m. Even with this medium conductivity the CM factor is never below -0.2, which directly results in a reduced DEP trapping force, given in Eq. 1. The higher the medium conductivity the stronger the DEP trapping force. At 100 mS/m medium conductivity, the CM factor below 100 kHz is not at its minimum of -0.5, but close with a value below -0.45.

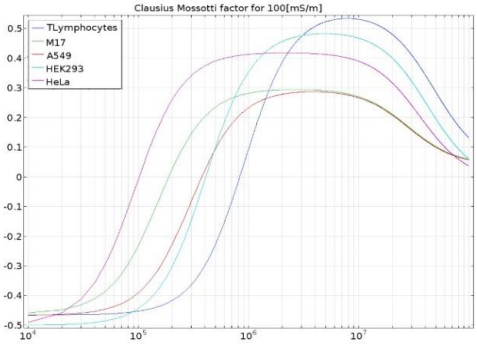

Figure 6. Clausius-Mossotti factor of different cells depending on the frequency of the electric field for medium conductivity of 100 mS/m.

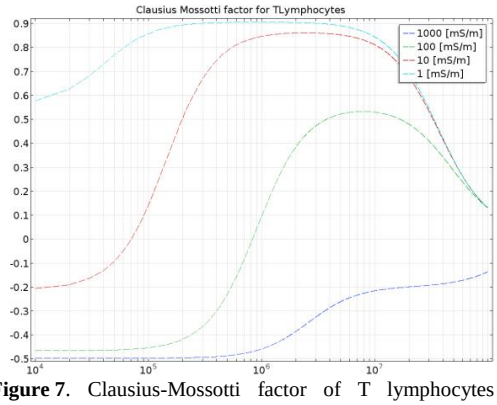

Figure 7. Clausius-Mossotti factor of T lymphocytes depending on the medium conductivity.

If the experimental conditions are not adapted and the DEP force is positive, the cells will not be trapped in the middle of the electrode array in open space, but will go towards high field regions and thus towards the electrodes' surface, as shown in Fig. 8.

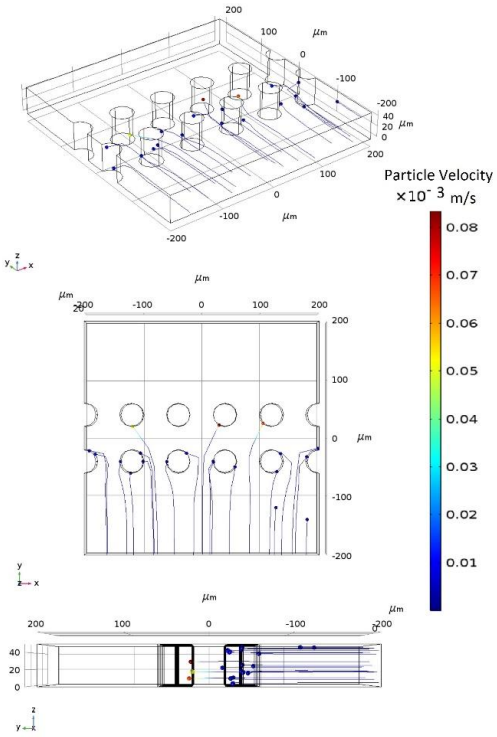

Figure 8. Perspective view (top), top view (middle) and side view (bottom) of T lymphocytes getting trapped on the electrodes due to the pDEP force. The medium conductivity is 100 mS/m and the frequency of the electric field is 10 MHz.

Applying the correct experimental conditions, for example, 100 kHz and 1000 mS/m for T lymphocytes, the cells are getting trapped in between the electrodes as shown in Fig. 9.

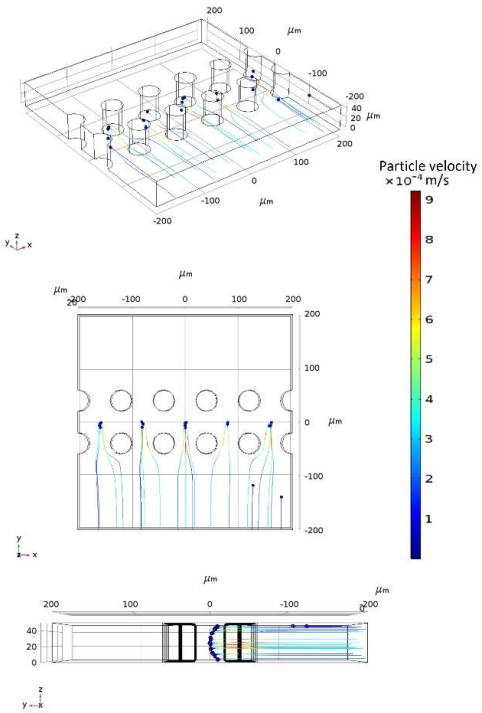

Figure 9. Perspective view (top), top view (middle) and side view (bottom) of T lymphocytes getting trapped in between the electrodes due to the nDEP force. The medium conductivity is 1000 mS/m and the frequency of the electric field is 100 kHz.

The experimental conditions of medium conductivity and electric field frequency have to be adapted. A first indication is the CM factor. Additionally finite elements simulations help illustrating and, finally, the experimental investigation has to be done.

2. Effect of the microfluidic pressure

Once the medium conductivity and the electric field frequency are found, the pressure of the fluid flow has to be adapted. The DEP trapping force, given in Eq. 1, and the fluid drag force, given in Eq. 2 have to cancel out inside the micro cage array and the initial velocity of the cell at the time it come to this point has to be neutral. Tuning the DEP force for the trapping in the first results section, we are now tuning the pressure and therefore the drag force in order to achieve trapping inside the array.

Working in nDEP conditions with a fixed electrode size, three scenarios for different pressures are possible. First, the pressure and therefore the drag

force is not sufficient to overcome the first, lower dielectric entrance barrier. The cells are stopped by the dielectrophoretic force before entering the micro cage array as shown in Fig. 10.

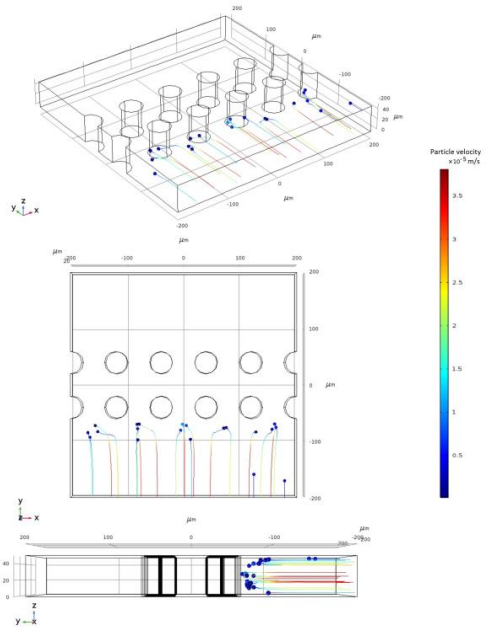

Figure 10. Perspective (top) and top (bottom) view of T lymphocytes prevented to access the micro cage space for a pressure difference of 0.01 mbar between inlet and outlet.

Second, if the pressure difference between the inlet and outlet, the drag force is always stronger then the DEP trapping force. The cells slow down inside the DEP trap, as seen in the velocity of the cells illustrated in the color of the trajectory in Fig. 11. However, in the end the cells get across the highest electric field between the downstream (exit) electrodes and are even accelerated by the DEP force, when they have passed the exit electrodes.

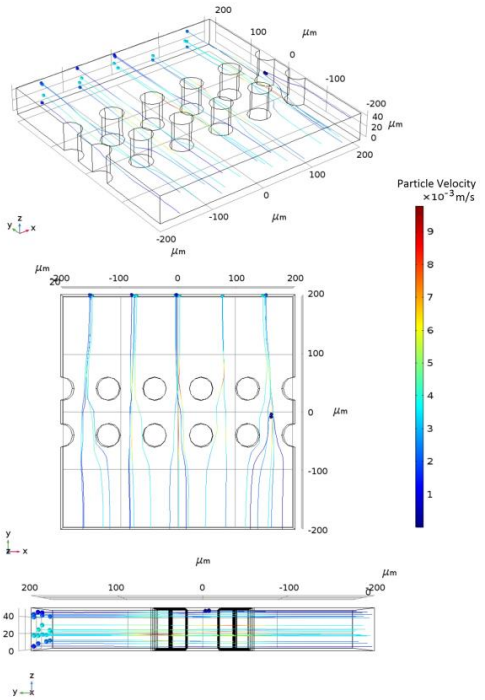

Figure 11. Perspective (top) and top (bottom) view of T lymphocytes flowing through the micro cage array for a pressure difference of 1 mbar between inlet and outlet. The cells decelerate in the trap, but reaccelerate when they leave the trap.

Adapting the pressure to the correct value allows trapping the cells within the micro cage array. The cells have to pass the first dielectric barrier. While approaching the local maximal value of the electric field in between the entrance electrodes, the cell slows down, but once it passes it, it reaccelerates. The restriction of the flow, between the electrodes, increases the speed of the cell additionally. However, this restriction is not present inside the trap. The second strong barrier eventually stops the cell completely and pushes it towards the local energy minimum, out of fluidic flow potential energy and dielectrophoretic potential energy. In this energy minimum, the force, which is the derivation of the energy in space, is zero. The trapping of the cells is illustrated in Fig. 12.

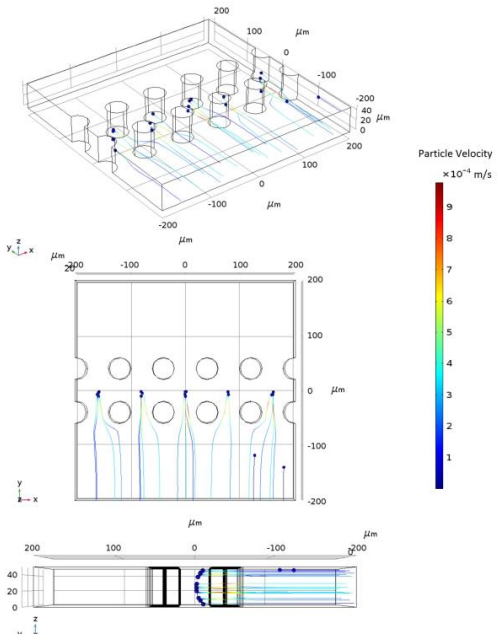

Figure 12. Perspective (top) and top (bottom) view of T lymphocytes trapped in the micro cage array for a pressure difference of 0.1 mbar between inlet and outlet. The cells accelerate, when passing the first dielectric barrier, but get eventually trapped.

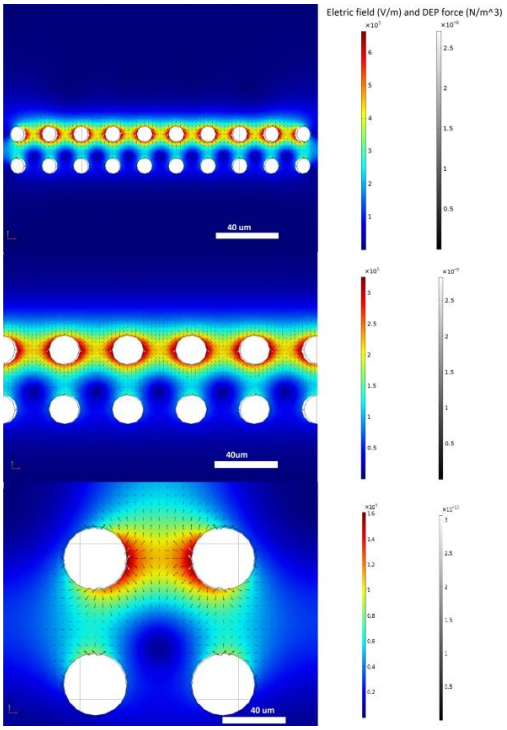

Figure 13. Illustration of the absolute value of the electric field and the corresponding DEP force. The DEP force increase, when decreasing the electrode distance (top: 80 µm; middle: 40 µm; bottom: 20 µm), due to the increase electric field and the increased gradient of the field.

3. Impact of the trap size

The last external parameter we are tuning is the trap size, which is defined as the distance between the electrode distance and which is at the same time the electrodes diameter. First, reducing trap size obviously increases the electric field, since the same voltage is applied over a shorter distance. Second, it changes the curvature of the electric field too. Since the DEP force, given in Eq. 1, depends on the gradient of the electric field squared $\nabla \boldsymbol{E}_{\boldsymbol{pk}}^{\boldsymbol{2}}$, as illustrated in Fig. 13, it changes with the trap size.

This variation of the trapping force, is as well reflected in the trapping behavior of the cells. A549 cells for example with a pressure of 0.1 mbar are not entering the electrode array, if the inter electrode distance is 20 µm, they are getting trapped in the array, if the inter electrode distance is 40 µm and are flowing through the electrode array if the inter electrode distance is 80 µm, as shown in Fig. 14.

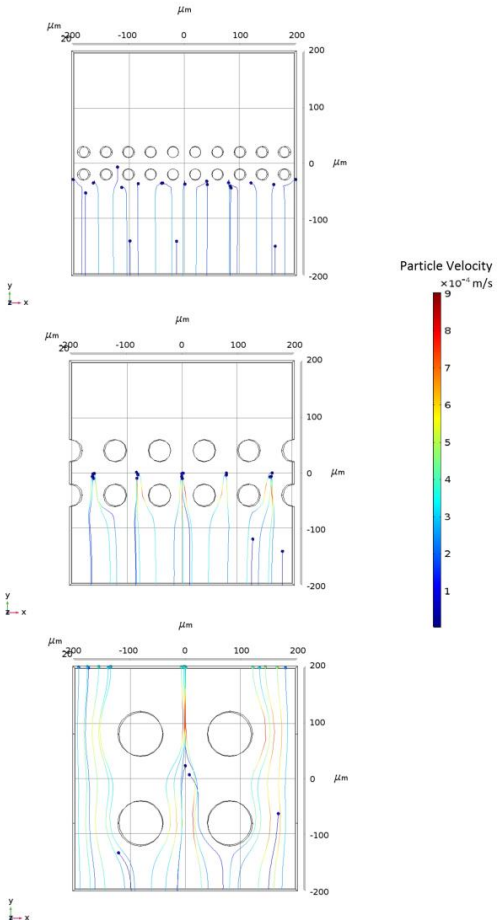

Figure 14. A549 cells for a pressure of 0.1 mbar are not entering the electrode array for a inter electrode distance of 20 µm are not entering the electrode array (top). For an inter electrode distance of 40 µm, they are getting trapped (middle) and for an inter electrode distance of 80 µm (bottom) they are flowing through the array.

4. Trapping efficiency for different cell types

As already partially discussed in the first results section, the CM factor depends on the cells dielectric properties. Different cells have different CM factor and radii, consequently they have different trapping behaviors. It turns out, that for the exact same conditions, some cell types are getting trapped and others are not, as shown in Fig. 15 for M17 cells and T lymphocytes and in Fig. 16 for HeLa and HEK 293 cells.

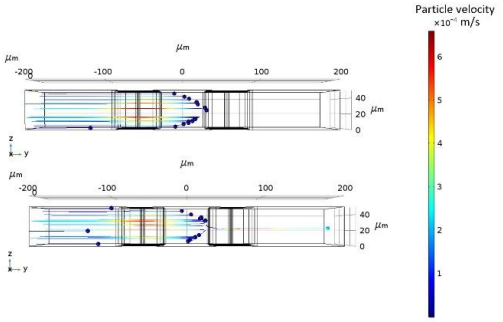

Figure 15. At a pressure of 0.07 mbar and an inter electrode distance of 40 µm and an electric field frequency of 2 MHz, M17 cells (top) are all getting trapped, while some T lymphocytes (bottom) are flowing through the array.

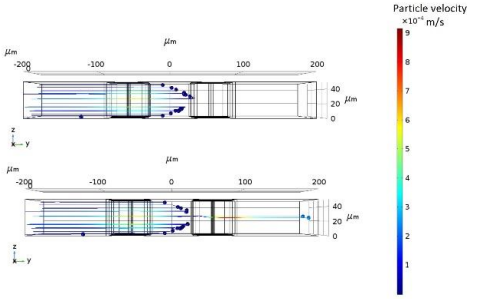

Figure 16. At a pressure of 0.06 mbar and an inter electrode distance of 40 µm and an electric field frequency of 2.3 MHz, HeLa cells (top) are all getting trapped, while some HEK 293 (bottom) are flowing through the array.

The different tapping behavior of different cells leads to the conclusion, that there is not one uniform experimental condition for all cell types, but specific ones for specific cell types. Therefore, in order to predict trapping of a certain cell type, finite element simulations with the specific dielectric parameters of the cells have to be performed.

Conclusions

In this paper, we present finite elements simulations, using COMSOL Multiphysics®, in which predict the trapping behavior of our nDEP traps. We could find trapping conditions for each of the cells, we considered. We investigated the effects of the frequency of the electric field, the medium conductivity as well as the trap size. Due to the diversity of cells we used, we did not find one configuration, which suits all needs, but we can simulate the behavior for every specific case.

References

[1] D. Di Carlo and L. P. Lee, "Dynamic Single-Cell Analysis for Quantitative Biology," *Anal. Chem.*, vol. 78, no. 23, pp. 7918–7925, Dec. 2006.

[2] H. A. Svahn and A. van den Berg, "Single cells or large populations?," *Lab Chip*, vol. 7, no. 5, pp. 544–546, 2007.

[3] G. R. Sant, K. B. Knopf, and D. M. Albala, "Live-single-cell phenotypic cancer biomarkers-future role in precision oncology?," *npj Precis. Oncol.*, vol. 1, no. 1, p. 21, 2017.

[4] S. Lindström and H. Andersson-Svahn, "Overview of single-cell analyses: microdevices and applications," *Lab Chip*, vol. 10, no. 207890, pp. 3663–3672, 2010.

[5] J. Voldman, M. L. Gray, M. Toner, and M. A. Schmidt, "A Microfabrication-Based Dynamic Array Cytometer," *Anal. Chem.*, vol. 74, no. 16, pp. 3984–3990, Aug. 2002.

[6] N. Manaresi *et al.*, "A cmos chip for individual cell manipulation and detection," *IEEE J. Solid-State Circuits*, vol. 38, no. 12, pp. 2297–2305, Dec. 2003.

[7] S. C. Kilchenmann, E. Rollo, P. Maoddi, and C. Guiducci, "Metal-Coated SU-8 Structures for High-Density 3-D Microelectrode Arrays," *Journal of Microelectromechanical Systems*, vol. 25, no. 3, pp. 425–431, Jun-2016.

[8] K. Keim, P. Maoddi, S. Kilchenmann, M. Comino, and C. Guiduccci, "Lab-on-a-Chip Platform for Single-Cell Electrorotation Using 3D Electrodes," in *microTAS*, 2017, pp. 932–934.

[9] E. Rollo *et al.*, "Label-free identification of activated T lymphocytes through tridimensional microsensors on chip," *Biosensors*, 2017.

[10] J. P. Beech, K. Keim, B. D. Ho, O. Ström, and J. O. Tegenfeldt, "Tuable separation and DNA manipulation in metal coated pillar arrays," in *microTAS*, 2018.

[11] R. Pethig, *Dielectrophoresis*. Chichester, UK: John Wiley & Sons, Ltd, 2017.

[12] P. R. C. Gascoyne, F. F. Becker, and X. B. Wang, "Numerical analysis of the influence of experimental conditions on the accuracy of dielectric parameters derived from electrorotation measurements," *Bioelectrochemistry Bioenerg.*, vol. 36, no. 2, pp. 115–125, 1995.

[13] S.-I. Han, Y.-D. Joo, and K.-H. Han, "An electrorotation technique for measuring the dielectric properties of cells with simultaneous use of negative quadrupolar dielectrophoresis and electrorotation.," *Analyst*, vol. 138, no. 5, pp. 1529–37, 2013.

[14] S. Kilchenmann, P. G. Carlotta, P. P. Demetri, and P. H. M. P, "Microfluidic and Electrokinetic Manipulation of Single Cells," 2016.

[15] A. El-Gaddar, M. Frénéa-Robin, D. Voyer, H. Aka, N. Haddour, and L. Krähenbühl, "Assessment of 0.5 T Static Field Exposure Effect on Yeast and HEK Cells Using Electrorotation," *Biophys. J.*, vol. 104, no. 8, pp. 1805–1811, Apr. 2013.

[16] R. T. K. Kumar, K. Cherukuri, R. Chadha, V. Holderby, and S. Prasad, "Planar biochip system for combinatorial electrokinetics," *Biochip J.*, vol. 10, no. 2, pp. 131–139, 2016.

[17] F. Y. Chang, M. K. Chen, M. H. Wang, and L. S. Jang, "Electrical Properties of HeLa Cells Based on Scalable 3D Interdigital Electrode Array," *Electroanalysis*, vol. 28, no. 5, pp. 962–969, 2016.

[18] K. Keim, P. Éry, A. Delattre, and C. Guiducci, "3D electrode arrays for trapping, analysis and selectrive release of single cells using DEP," in *Micro Total Analysis Systems*, 2018.

Acknowledgements

We would like to thank COMSOL® Switzerland and especially Thierry Luthy for support, setting up the simulations. Many thanks to the Scientific IT and Application support of EPFL, which provided us guidance and support in using the EPFL cluster to compute some of the simulations. This work was finance by the Swiss National Science Foundation (205321_179086).

Contact

kevin.keim@epfl.ch; +41 21 69 31335

ISSN 0173-0835 · ELCTDN 40 (14) 1745–1860 (2019) · Vol. 40 · No. 14 · July 2019

ELECTROPHORESIS

Electrokinetics | Fluidics | Proteomics

14 | 19

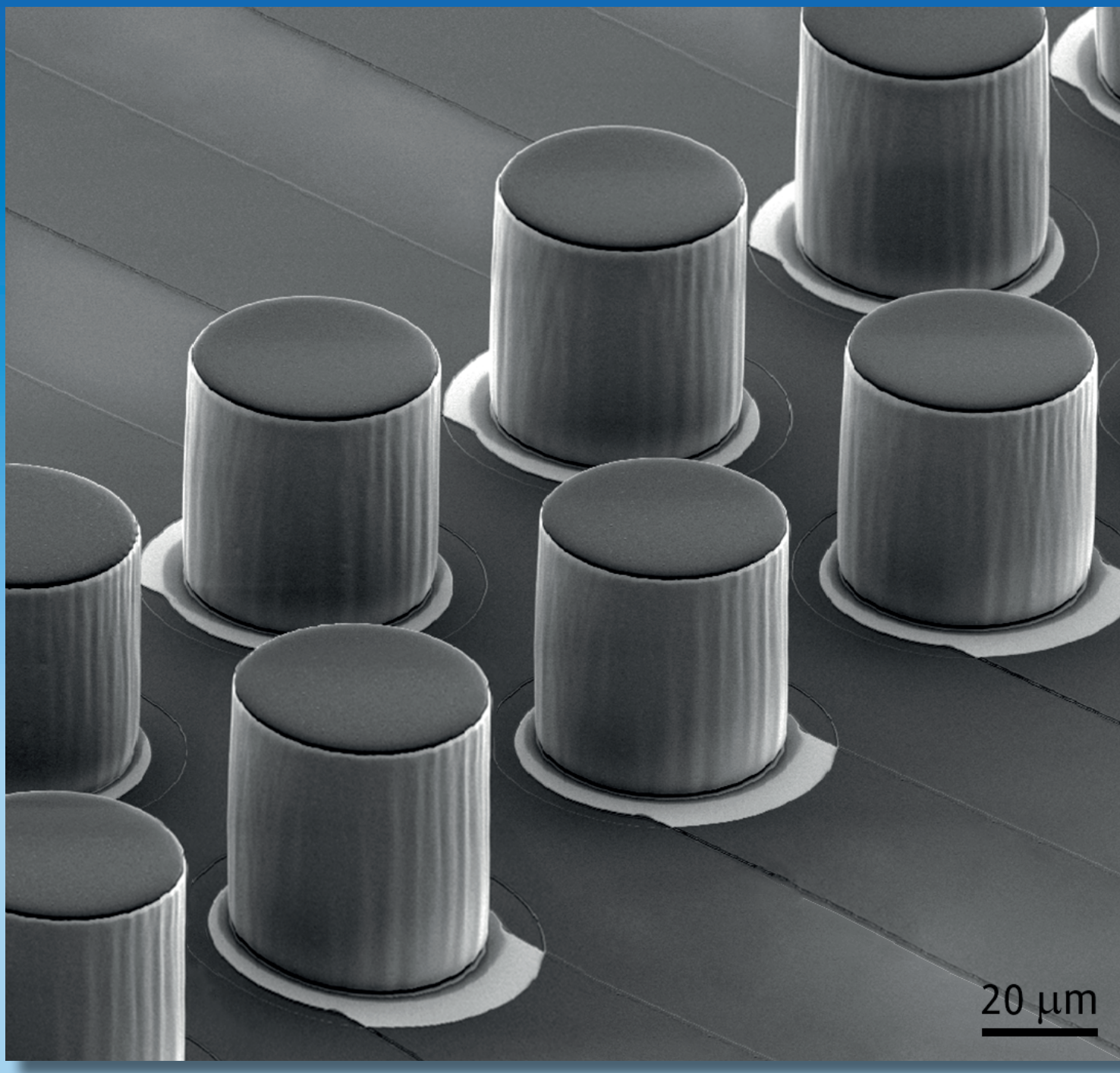

www.electrophoresis-journal.com

WILEY-VCH

Front Cover: On-chip technology for single-cell arraying, electrorotation-based analysis and selective release

"The standing pillars extend from the bottom to the top of a 50 μm high microfluidic chamber, thus generating uniform electric field lines across the direction normal to the chip surface. Each pillar electrode is singularly connected, which allow to selectively trap single cells in flow inside each adjacent quadrupole and to make them rotating at constant speeds. The observation of speed induced by different electric field frequencies reveals the dielectric properties of the cell." [151] reproduced with the permission of John Wiley and Sons.

3 Single-cell electrokinetics-based trapping and analysis by electrorotation

In this chapter, we will present the experimental results on the selective trapping and releasing of single cells in arrayed dielectrophoretic micro-cages, as well as their analysis via electrorotation.

First, a brief introduction to the theory of electrorotation is given. It explains the basic principles and allows the reader to understand how specific cell parameters can be extracted from the rotation of cells in rotating electric fields.

Second, the experimental innovations and improvement steps[152, 153] towards our parallel electrorotation system with individual controll on trapping and release of single cells are presented. The final system itself will be presented make use of our paper published in 2019 in Electrophoresis [151]. Additional further analysis using this system for a study of the effect of osmolarity of the specific cell membrane capacitance will be presented [151], illustrating how the system can not only be used to distinguish between different cell populations, but as well to distinguish between populations of one cell line in different osmolar conditions.

3.1 Theoretical background on electrorotation

As explained previously, particles in suspension polarize in an electric field and can be moved towards high or low field regions by experiencing pDEP or nDEP. However, when the particles are placed in a rotating electric field, they experience a torque due to the field's rotation [154]. The dipole moment of the particles rotates with the electric field, but lags behind by a phase factor, which is correlated to the complex part of the Clausius-Mossotti factor [154]. The time-averaged torque is given by [142]

$$< T(t) >= -4\pi\epsilon_0\epsilon_m R^3 Im[CM] E_0^2 \tag{3.1}$$

with the medium permittivity being ϵ_m, the particle radius R and the complex part of its Clausius-Mossotti factor $Im[CM]$, as well as the amplitude of the rotating electric field E_0.

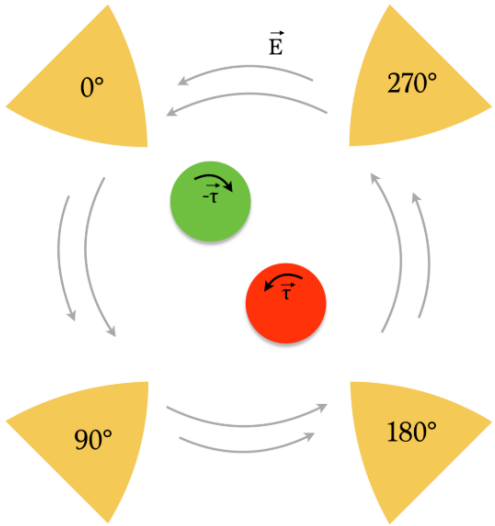

Figure 3.1 – Cells placed in a rotating electric field, can either rotate in the direction of the rotating electric field if $Im[CM] < 0$ (red particle) or against the electric field if $Im[CM] > 0$ (green particle). Figure reproduced from [149] with permission from Marta Comino.

Continuously exerting a torque on a particle will make it rotate faster and faster. The friction from the surrounding medium damps the rotation by a resistive viscose torque in the opposite direction of the rotation and is given by [155, 142]

$$T_\eta = -8\pi\eta R^3\Omega_0 \tag{3.2}$$

with the dynamic viscosity of the surrounding fluid [155] η and constant angular velocity Ω_0. This model is valid for a stationary fluid, where the fluid streamlines around the particle are not turbulent but laminar.

The stationary state, in which there is no net torque on the particle in the rotating electric field, can be found when the torque originated by the rotating field (eq. 3.1) and the resistive viscose torque (eq. 3.2) equal out. One finds a constant angular velocity of

$$\Omega_0 = -\frac{\epsilon_0\epsilon_m}{2\eta} Im[CM] E_0^2 \tag{3.3}$$

This is the angular velocity which is observed after the cell is accelerated up to a steady rotation speed.

Depending on the imaginary part of the Clausius-Mossotti factor the particle can either rotate in the direction of the rotating electric field, if $Im[CM] < 0$, as shown for the red particle in Fig. 3.1, or against the rotation of the electric field, if $Im[CM] > 0$, as shown for the green

particle. The imaginary part of the Clausius-Mossotti factor for the same particle changes for the same condition depending on the frequency of the applied electric field. For cells, usually the single-shell model is used to define the Clausius-Mossotti factor as explained in the previous chapter.

3.2 A parallelized electrorotation setup

Electrorotation is an established technology, which exists since decades [115, 116]. It used to be performed in micro-chambers of hundreds of micrometers in diameter. Lately, electrorotation analysis has been done within microfluidic channels, enabling a batch-wise continuous analysis. However, these systems are lacking the possibility to parallelize the analysis and therefore to enable the technology for analysis of a sample at the single cell level. In the following, we will show how a parallelized electrorotation platform can be realized and we will describe the implementations step by step based on our publications.

First, we present a system with 64 electrodes positioned on the chip, which are connected by an underlying double metal cross-bar structure enabling to contact all electrodes with only four off-chip connections [152]. Changing the connection method to a single metal layer and individual off-chip connections for each electrode allows individual trapping and release of single-cell, as well as their analysis by electrorotation[153].

Second, we demonstrated that the system can simultaneously trap and analyse several cells in parallel, by alternating the dielectrophoretic trapping and the electrorotation signal. The membrane parameters of four cell lines are investigated and the cell lines can be distinguished based on their electrorotation spectra [151].

Third, the influences of the system on the cell viability were investigated in real-time and failure of the membrane sealing function were observed by a shift in the electrorotation spectrum, as well as in a drop of the membrane capacitance. Changes of the membrane capacitance within a cell population are investigated by an osmolarity study on HEK293 cells [156]

3.2.1 Toward a parallelized electroroation setup

First, we addressed the following question: are three dimensional electrodes with distances within the size of single cells capable to perform electrorotation. Previous experiments in our group used three dimensional electrodes for impedance-based cell detection [34], however this technology used voltages up to $400 mV$, while we are applying amplitudes in the order of volts.

In order to demonstrate electrorotation in single-cell sized dielectrophoretic microcages built out of three dimensional electrodes, we constructed an array out of these electrodes which are connected by two underlying metal layers which crossed each other on chip. This allowed to

apply four different signals from the frequency generator which are needed for electrorotation to the specific electrodes.

In order to have individual control on each electrode, enabling selective trapping and release of individual cells, we changed to a simpler on-chip structure using only one metal connection layer, but several off-chip connections.

Using electrodes connected by a double metal cross-bar structure in order to contact many electrodes with few

The following content is adapted from our conference abstracted published in 2017 as "Lab-on-a-chip platform for single-cell electrorotation using 3D electrodes" (Kevin Keim, Pietro Maoddi, Samuel Kilchenmann, Marta Comino, Carlotta Guiducci) in the proceeding of the 21st International Conference on Miniaturized Systems for Chemistry and Life Sciences (microTAS) in Savannah, Georgia, USA [152].

First measurements of electrorotation spectra of single cells within three-dimensional electrodes inter-distanced in the order of magnitude of a cell diameter could be performed with a newly designed system. Two lines of 32 three-dimensional electrodes are placed in across a $5mm$ wide and $50\mu m$ high microfluidic channel. These three-dimensional electrodes with an inter electrode distance of $80\mu m$ are fabricated by covering cylindrical $50\mu m$-high and $80\mu m$-wide SU-8 pillars with titanium and platinum. Ion beam etching without etching mask removes the metal from planar surfaces but leaves vertical surfaces coated [4]. Four neighboring electrodes constitute an electrorotation quadrupole. In order to apply four different signals to the arrayed quadrupoles an underlying double metal cross bar structure is used to contact them. The bottom metal layer is patterned using lift-off and insulated with a sputtered SiO_2 layer. A top metal layer is patterned using ion beam etching and is again insulated with SiO_2. Vias to connect the two metal layers as well as the electrodes are etched in the insulation layers by reactive ion etching. A SEM micrograph of the device is shown in Fig. 3.2. The channel is closed by an $8mm$-thick PDMS layer.

$CD8^+$ human immortalized T lymphocytes were suspended in isotonic solution with a conductivity of $56mS/m$. They were injected in the microfluidic channel and positioned between the electrodes using a differential pressure system (Elveflow OB1 Pressure Controller). The electrode array is spanning the complete channel width, so cells are necessarily passing through a quadrupole. Stopping the microfluidic flow, while the cells are within the electrodes and applying an electrorotation signal, allowed to acquire first electrorotation spectra.

Our technology surpasses several limitations of previously-reported solutions. The use of an underlying double metal cross-bar structures allows us to contact an array composed of several quadrupole electrodes with-in a microfluidic channel. We could demonstrate the acquisition of electrorotation spectra within those 3D quadrupole electrodes. The device is designed to accommodate multiple single cells in parallel, where different clones could be

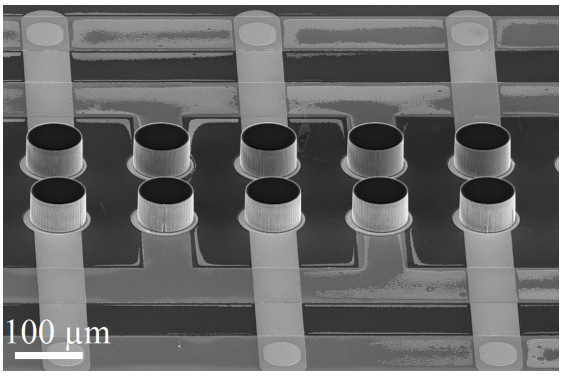

Figure 3.2 – SEM micrograph of three dimensional-elecrodes integrated in a dielectrophoretic trapping array. The electrodes are connected by two underlying metal layers, which are insulated by a SiO_2 layer. The cross-bar structure of the metal allows to contact 64 electrodes with only four off-chip connections. Figure depicted from [152].

trapped by dielectrophoresis, analyzed and released contemporary, increasing throughput.

Trapping cells in the array using DEP and individual control on the electrodes

The following content is partially adapted from our conference abstracted published in 2018 in the conference proceeding of the 22nd International Conference on Miniaturized Systems for Chemistry and Life Sciences (microTAS) in Kaoshiung, Taiwan under the title "3D electrode arrays for trapping, analysis and selective release of single cells using DEP" (Kevin Keim, Paul Éry, Aurélien Delattre, Carlotta Guiducci) [153].

The previously presented layout allows to acquire electrorotation spectra of single cells in quadrupoles of an inter electrode distance in the order of magnitude of a single cell. However, the cell needs to be positioned within the trap by the means of microfluidics. This means only cells which are arriving at the same time in the array can be analyzed together. The ability to trap the cells by dielectrophoresis inside the cages allows to position multiple single cells in the array at the same time. To do so, as shown by the simulations in the previous chapter, the conductivity of the surrounding medium was increased from $56 mS/m$ to $100 mS/m$.

Multiple conditions for an effective trapping and a good evaluation of the electrorotation spectrum have been investigated.

First, the frequency of the DEP trapping signal was investigated. According to theoretical simulations the lower the frequency of the DEP signal, the better the trapping, however, low frequencies lead to some practical problems. At a frequency of $10 kHz$, an amplitude of $5 V$ and a medium conductivity of $100 mS/m$ bubbles appear immediately after the application of the DEP signal, as shown in Fig. 3.3(a).

Increasing the frequency of the DEP signal to $100 kHz$, prevents the bubble formation.

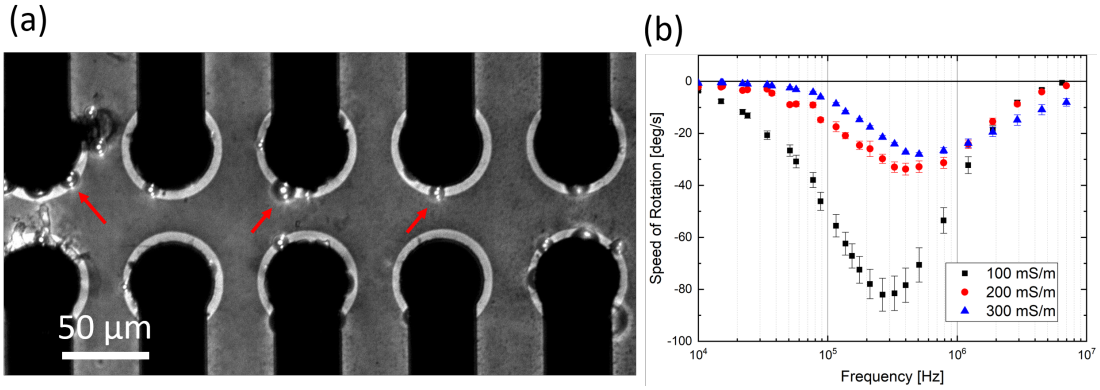

Figure 3.3 – (a)At a DEP traping frequency of 10 kHz and a voltage of 5 V, bubbles appear immediately at the electrodes. The red arrows point to the created bubbles. (b) Averaged electrorotation spectra of human immortalized T lymphocytes in media of different conductivity.

Increasing the medium conductivity improves the trapping of the cells, since the real part of the Clausius-Mossotti factor becomes more negative. However, the imaginary part of the Clausius-Mossotti factor is influenced as well. An increase of the medium conductivity leads to a less distinct imaginary part of the Clausius-Mossotti factor and therefore a reduced speed of rotation of the cells within the traps. As shown in Fig. 3.3(b), the maximal speed of rotation reduces from about $80 deg/s$ in a conductivity of $100 mS/m$ to a speed of $30 deg/s$ in $200 mS/m$ and to $25 deg/s$ in $300 mS/m$. An electrorotation spectrum with higher rotation speeds, allows to extract the speed of rotation with less relative error and leads to a more precise cell parameter extraction, therefore in the following experiments a medium conductivity of $100 mS/m$ is used in order to achieve reliable trapping and precise parameter extraction from the electrorotation measurements.

Additionally, every electrode is connected individually by interconnections on the chip, a SEM micrograph of the system is shown in Fig. 3.4. Providing a connection pin from the printed circuit board (PCB) to the chip for every electrode, allows to wire the connections without intersections on the chip, which enables a single metal connection layer and a removal of the double metal layer, which also simplifies the process flow from a six to a four mask process. This enables individual control on the electrodes and at the same time to disable specific downstream electrodes to perform release from specific traps.

Different cells are injected in microfluidic chips with different electrode diameters of $20 \mu m$, $40 \mu m$ and $80 \mu m$ with channel widths of $1.6 mm$, $3.2 mm$ and $6.4 mm$, respectively. The flowrate is set between $200 nl/min$ and $1 \mu l/min$ depending on the channel width, the cell type, the medium conductivity and the applied voltage on the electrodes. In absence of signals to the electrodes, the cells flow through the device from inlet to outlet. By applying DEP signals to the quadrupole, electrokinetic forces are generated that can hold the cell in place against the flow. In the experiments, the applied electric signal ($1 V_{pp}$) created a small dielectric barrier at the upstream (entry) electrodes and a high dielectric barrier ($5 Vpp$) at the downstream

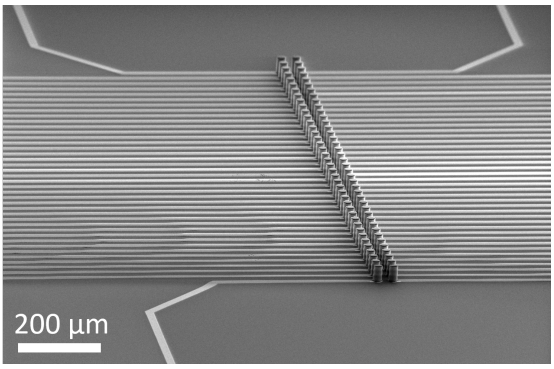

Figure 3.4 – SEM micrograph of a DEP microcage array of three-dimensional electrode with individual connections for every electrode. Figure depicted from [153].

(exit) electrodes, allowing cells to enter but not to pass the trap (catch configuration,3.5(a)/5s). Once several traps were occupied by single cells, the traps are closed by applying a barrier of $5V_{pp}$ to both rows, preventing additional cells to enter the trap. Subsequently, the flow is turned off and the trapping configuration is replaced by a rotating electric field obtained by applying signals with 90° phase shift to neighboring electrodes. This creates a clockwise rotating electric field in every other micro-cage and a counterclockwise electric field in the others. This induces a rotation speed on cells that depends on their dielectric parameters. It is read out using a camera grabbing five images per second. The frequency of the electric signal was logarithmically swept from $10kHz$ to $40MHz$ in 30 steps. Each frequency is applied for $5s$, which allows to acquire the rotation spectrum of multiple single cells within $3min$. After the spectra are taken the dielectric trapping is reactivated, so the cells remain trapped when reapplying the fluid flow, as shown in Fig. 3.5(h-i)/33-37s. Turning off the electric field the cell is carried away with the flow, as shown in Fig. 3.5(j-k)/45-47s.

The chips could be used up to two weeks. Once they clogged with organic materials like cells, cell fragments or bacteria, they could be cleaned by flushing a 1% sodium hypochlorite solution through the chip. Electrorotation spectra of several HeLa and HEK 293 cells could be acquired within the array. Alternating between trapping and rotation, the spectra could reliably be acquired over several hours.

3.2.2 Parallel acquisition of electrorotation spectra using alternating trapping and rotating signals allows to analyze the membrane capacitance of cell lines in flow

In the setup described in the previous subsection, the flow is stopped after the cell is trapped in the dielectrophoretic micro cage. At that point, the rotation signal is applied to analyze the cell dielectric parameters. After the acquisition of the electrorotation spectrum has been completed, the measurement of the rotation signals is replaced by the trapping signal and eventually in the configuration enabling single cell releases. Turning off the flow completely,

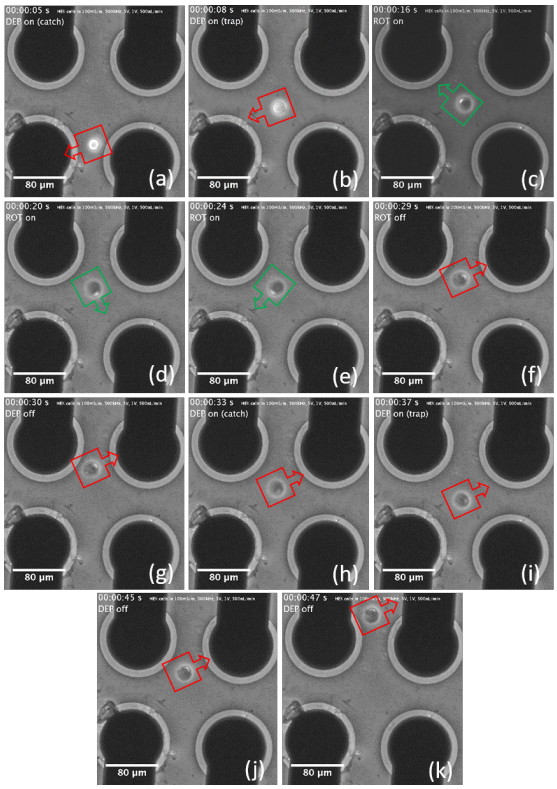

Figure 3.5 – Series of micrscope images showing the subsequential trapping of a cell (a-b), the analysis by electrorotation without flow (c-f), the retrapping after the analysis (g-h) and the release of the cell turning on the flow (i-j). Figure depicted from [153].

so the cells remain in the trap without the trapping signal takes time. Additionally the cell is not always centered in the middle of the trap due to small microfluidic flows. The movement of the cell to regions of different electric fields can distort the electrorotation spectrum.

One solution to this problem is to alternate the DEP trapping and the electrorotation signals as shown by Rohani et al. [94]. The cells are kept trapped in the middle of the dielectrophoretic micro-cages, while they are rotating in parallel and their electrorotation spectrum is acquired. This allows as well to keep the flow during the acquisition of the experiments, which has several advantages. First, the acquisition of spectra can start faster, since no waiting time is need to stop the flow. The cells are always centered in the middle of the quadrupoles. Second, additional cells are blocked out of the array, because of the dielectrophoretic barrier at the entrance. These waiting cells can be analyzed in the next batch and are kept in front of the trap.

This modification allows to analyze significant numbers of cells, and has a theoretical throughput of 600 cells/hour. Using this system, four different cell lines and over 200 single cells could be analyzed and their membrane capacitance calculated.

The results are reported in the paper "On-chip technology for single-cell arraying, electrorotation-based analysis and selective release" (Kevin Keim, Mohammed Z. Rashed, Samuel C. Kilchenmann, Aurélien Delattre, António Gonçalves, Paul Éry, Carlotta Guiducci) in Electrophoresis 2019 [151], reproduced with the permission of John Wiley and Sons.

Contributions

The electrorotation experiments on the different cell lines were carried out by Kevin Keim and Mohammed Z. Rashed. Mohammed did a five month research exchange from the laboratory of Prof. Stuart Williams at the University of Louville, he worked under the supervision and in collaboration with Kevin Keim and Carlotta Guiducci. Samuel C. Kilchenmann programmed the communication between the frequency generator and the video acquisition. The alternation of the trapping signal was implemented by Kevin Keim and Aurélien Delattre, as well as the design and the programming of the printed circuit board (PCB). The simulations were run and post-processed by Kevin Keim, based on previous work of from Kevin Keim, António Gonçalves and Carlotta Guiducci [150]. Paul Éry helped with the editing of the figures. The manuscript was written by Kevin Keim in direct collaboration with Carlotta Guiducci. It was edited by Mohammed Z. Rashed, Samuel C. Kilchenmann and Carlotta Guiducci. All authors read and approved the manuscript.

Electrophoresis 2019, *40*, 1830–1838

Kevin Keim
Mohamed Z. Rashed
Samuel C. Kilchenmann
Aurélien Delattre
António F. Gonçalves
Paul Éry
Carlotta Guiducci

Laboratory of Life Sciences Electronics, École Polytechnique Fédérale de Lausanne, Lausanne, Switzerland

Received October 15, 2018
Revised May 7, 2019
Accepted May 10, 2019

Research Article

On-chip technology for single-cell arraying, electrorotation-based analysis and selective release

This paper reports a method for label-free single-cell biophysical analysis of multiple cells trapped in suspension by electrokinetic forces. Tri-dimensional pillar electrodes arranged along the width of a microfluidic chamber define actuators for single cell trapping and selective release by electrokinetic force. Moreover, a rotation can be induced on the cell in combination with a negative DEP force to retain the cell against the flow. The measurement of the rotation speed of the cell as a function of the electric field frequency define an electrorotation spectrum that allows to study the dielectric properties of the cell. The system presented here shows for the first time the simultaneous electrorotation analysis of multiple single cells in separate micro cages that can be selectively addressed to trap and/or release the cells. Chips with 39 micro-actuators of different interelectrode distance were fabricated to study cells with different sizes. The extracted dielectric properties of Henrietta Lacks, human embryonic kidney 293, and human immortalized T lymphocytes cells were found in agreements with previous findings. Moreover, the membrane capacitance of M17 neuroblastoma cells was investigated and found to fall in in the range of $7.49 \pm 0.39\,\mathrm{mF/m^2}$.

Keywords:
Dielectrophoretic trapping / Electrorotation / Single-cell analysis / Single-cell array / Single-cell release
DOI 10.1002/elps.201900097

Additional supporting information may be found online in the Supporting Information section at the end of the article.

1 Introduction

Electrorotation (ROT) is a label-free analysis technique [1, 2], which can read out the dielectric properties of cells. It can differentiate between cell lines [3], observe cell membrane changes [4–6], or investigate the cytoplasm properties of cells [7], to only mention some examples.

Existing systems employing this technique suffer from a very low parallel operation. Simultaneous rotation of multiple single cells in an array has never been demonstrated so far. The technologies used to integrate electrorotation actuators on microfluidic chips allows a very limited scalability and flexibility in the channel height and cage size. We apply the vertical electrodes integration approach that we presented in previous works [8, 9] to develop a system for single cells arraying and parallel electrorotation analysis in 50 μm high microfluidic chambers (Fig. 1B). Each electrode is connected to a dedicated pad to allow the independent control of each single-cell actuator to capture a cell, retain it, rotate it by electric field of varying frequencies while being held against the flow, and finally selectively released.

Dielectrophoretic forces have been used previously to arrange cells in arrays. For instance, negative dielectrophoretic (nDEP) traps can capture cells at electric field minima [10,11]. In a device available on the market by Silicon Biosystems, multiple cells can be individually positioned in a 2D array to be analyzed by fluorescence through optical markers [11]. However, after positioning, the cells are closed into the chamber and no flow is applied. Devices to trap and release cells in flow, arrayed in a selective manner, have been developed using pillar-like electrodes, exploiting the higher efficiency of 3D structures to apply dielectrophoretic holding forces [10, 12].

Correspondence: Kevin Keim, École Polytechnique Fédérale de Lausanne, Laboratory of Life Sciences Electronics, Station 17, STI-CLSE, BM2.107, CH-1015 Lausanne, Switzerland
E-mail: kevin.keim@epfl.ch

Abbreviations: **CM**, Clausius-Mossotti; **DEP**, dielectrophoresis; **HEK 293**, human embryonic kidney 293; **HeLa**, Henrietta Lacks; **nDep**, negative dielectrophoresis; **PCB**, printed circuit board; **ROT**, electrorotation; **SU-8**, Gersteltec GM 1070; **Ti**, titanium

Color online: See the article online to view Figs. 1–4 in color.

Electrophoresis 2019, *40*, 1830–1838

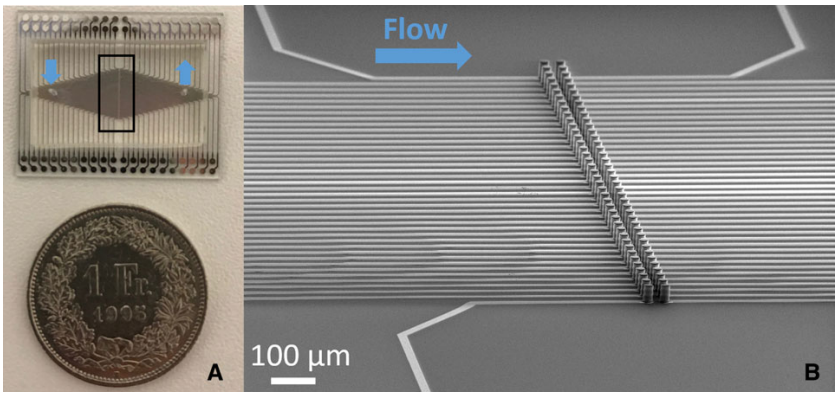

Figure 1. (A) Photograph of a bonded chip with a width of the microfluidic channel of 6.4 mm and with both electrode diameter and interelectrode distance of 80 µm. The black box shows the region observed by scanning electron microscopy shown in (B). (B) Scanning electron microscope micrograph of two arrays of metal covered SU-8 electrodes, which are separately connected by an underlying, insulated metal wire. The electrode´s diameters and interelectrode distance is 20 µm.

3D microelectrodes have been fabricated by additive techniques, such as electroplating [13–16], pyrolysis of photoresist [17, 18], or ion implantation into PDMS [19]. Subtractive techniques have also been employed such as based on etching of highly doped silicon [20, 21], or on the conformal deposition of conductive materials on a 3D scaffold and their subsequent pattering [22, 23]. Our group has recently developed a novel fabrication method to obtain high aspect ratio of tri-dimensional electrodes of any desired shape by covering passive negative photoresist Gersteltec GM 1070 (SU-8) cores with metal and subsequent mask-less etching which only lets metal to remain on the sidewall of the cores [8]. This technique combines the advantages of both additive and subtractive techniques, it is fast and inexpensive compared to electroplating, has high conductive electrodes compared to pyrolysis technique, doped silicon and ion implanted PDMS, as well as a micrometer precision.

Previous systems used an asymmetric electrode configuration and electric signals of the same amplitude to create open dielectrophoretic cages upstream to trap cells and analyze them by fluorescence [10]. In our system, we can address the four electrodes of the quadrupole separately, thus control the entry of the cells then retain them by blocking additional cells from entering the same trap. The first advantage of this configuration is that the same electrodes can be used for two neighboring traps, which enables to control the entire section of the flow chamber along the array of traps. This feature is crucial for handling low concentration of cells of interest inside the flow.

The second advantage is that the quadrupole is composed by four electrodes arranged symmetrically and close to each other, which grants high quality electrorotation spectra. In order to acquire accurate electrorotation spectra, cells have to be in the center of the rotating electric field. In large electrorotation chambers laser tweezers have been used in order to center the cells and keep them in place [24–26], so the cell experiences the torque corresponding to its position within the electrodes throughout the measurement [27]. This clearly comes at the cost of scalability and complexity provided by such techniques. Other approaches alternate nDEP signals and ROT actuation [28] or superpose them [3, 29]. Octopoles, which consist of a quadrupole placed on the bottom of a channel and one at the top [30], can create a rotating electric field, by placing the top and bottom quadrupole rotated by an angle [31] and perform electrorotation experiments.

All these systems report one single cage except for the work by Fuhr et al. where three single-cell octopoles are placed after each other in a narrow microfluidic channel [25]. However, simultaneous electrorotation on multiple single cells were not reported.

In our system, multiple trapping and rotation of single cells is achieved by independently-addressed single quadrupole cages positioned perpendicularly to the flow stream in a large microfluidic chamber.

2 Materials and methods

2.1 Experimental

2.1.1 Microfabrication

The dielectrophoretic microcages consist of two arrays of 40 3D electrodes integrated within a microfluidic channel. This leads to a total amount of 39 arrayed micro cages. The height of the electrodes and of the surrounding microfluidic channel is 50 µm. The diameter of the electrodes and of the inter electrode distance varies between 20, 40, and 80 µm.

First, a Ti/Pt/Ti (20/200/20 nm) is sputtered (*Pfeiffer Spider 600*) on the plane wafer and connection lines are subsequently patterned by ion beam etching (*Veeco Nexus IBE350*). Then, a SiO_2 (300 nm) layer is sputtered to insulate the wires. Vias (*SPTS APS Dielectric Etcher*) are etched into the insulation layer where the 3D electrodes and the contacts from the printed circuit board (PCB) to the chip are placed later on. A 50 µm SU-8 skeleton is patterned on the uninsulated metal. The whole wafer and therefore the SU-8 skeleton as well is covered with a Ti/Pt (20 nm/200 nm) metal layer by sputtering. This process achieves the coating of the side walls of the SU-8 skeleton. The metal on the planar wafer and on top of the electrodes is subsequently removed by ion beam etching without an etching mask. Due to an etching angle

of 0° perpendicular to the wafer surface, the metal on the side walls of the SU-8 skeleton remains. This process was presented in [8] except for the insulation of the planar wires with sputtered SiO_2. A second layer of 50 µm SU-8 is coated and patterned on the wafer, forming the wide microfluidic channel. The chip is closed by irreversibly bonding PDMS to the SU-8 channel [32]. A photograph of the final chip is shown in Fig. 1A.

2.1.2 Cell preparation

Henrietta Lacks (HeLa), human embryonic kidney 293 (HEK 293), and BE(2)-M17 human neuroblastoma cells are cultured in *DMEM*, human immortalized T lymphocytes are grown in suspension in Roswell Park Memorial Institute Medium. In both media, 10% Fetal bovine serum and 1% antibiotics (L-Glutamine-penicillin-streptomycin) are added. Before the experiments, the adherent HeLa, HEK 293 and M17 cells are detached from the surface of the culture flask using 1X *Trypsin* and all cells are resuspended in an isotonic solution (8.6% dextrose and 0.3% sucrose) with an adapted conductivity of 100 mS/m using 1X PBS. The cell concentration was around 200 000 cells per milliliter.

Before the experiments, the chips are primed by flushing 2 mL of the corresponding culture medium (including Fetal bovine serum) and subsequently by flushing 2 mL of the 100 mS/m solution, in which the cells are suspended. In many examples, electrorotation experiments are performed at a medium conductivity of 56 mS/m, which is found to be the conductivity at which the cytoplasm conductivity of cells can be investigated [7, 33]. However, in order to obtain nDEP at frequencies high enough to avoid electrolysis at the electrodes, 100 mS/m conductive media was used.

2.1.3 Measurement procedure

Cells are injected in the microchips with the proper electrode diameter size based on cells size. HeLa, HEK 293, and M17 cells are injected in chips with an electrode diameter of 40 and 80 µm. They are not injected in chips with an interelectrode distance of 20 µm, since they occasionally cause clogging due to their size, especially if cell clusters are formed. T lymphocytes can be injected in chips featuring any of the three electrode diameter.

The cells in suspension are driven through the device by a flow-rate between 200 and 1 µL/min. With no electric field applied, they simply pass by the upstream (entrance) electrodes first and then the downstream (exit) electrodes. For the trapping of cells, the arbitrary waveform generator (*TTi TGA12104*) creates four signals. Two signals of 5 V amplitude and a phase shift of 180° and two signals of 1 V amplitude and a phase shift of 180°. Applying an alternating current (100 kHz) electric voltage signal of 1 V amplitude at the entrance and of 5 V amplitude at the exit electrodes creates a lower dielectrophoretic barrier at the entrance and a higher barrier at the exit of the array. Due to the drag force of the fluid flow, the cells can pass the lower entrance barrier, but cannot overcome the higher exit barrier, consequently they are trapped in the array, as shown on the left sketch of Fig. 2(A).

After a cell is trapped in a single-cell microcage, the voltage at the two upstream electrodes is raised to 5 V amplitude preventing additional cells to enter the trap (the voltage is changed by means of selection circuitry on the PCB, described in the Supporting Information chapter 3). The other traps remain open, with an entrance voltage of 1 V amplitude. Adjacent quadrupoles now have one entrance electrode with an applied voltage of 1 V amplitude and one with 5 V

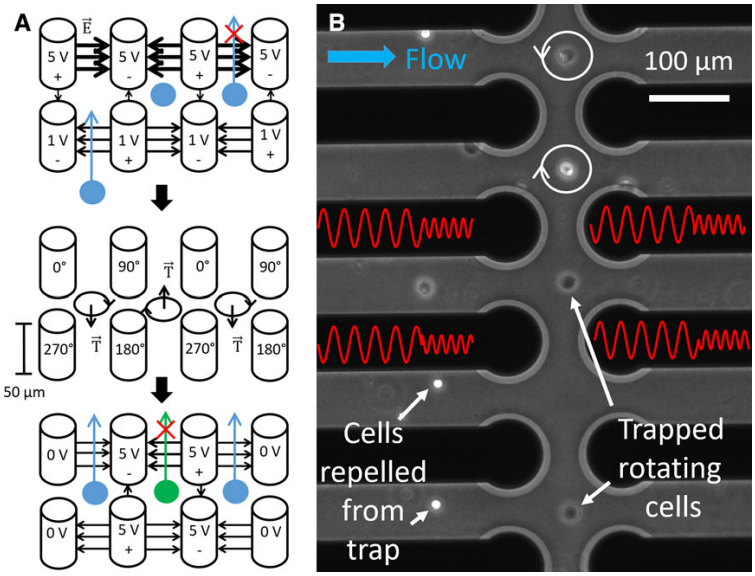

Figure 2. (A) Working principle of the microcage array. Single cells are trapped, analyzed by electrorotation and are selectively released. (B) Microscope image of rotating cells simultaneously trapped within the microcage array by alternating DEP and ROT signals. The first DEP signal has a phase shift of 180° between neighboring electrodes and exerts a trapping force. The second ROT signal has a phase shift of 90° between neighboring electrodes (the electric signals on the electrodes are illustrated in red) and exerts a torque on the cells making them rotate. Cells outside the cages are repelled and this cannot enter due to the presence of a dielectrophoretic barrier.

amplitude, however, the dielectrophoretic barrier is still low enough to allow incoming cells to enter the trap. After a sufficient amount of filled single-cell traps is reached, all traps are closed and the electric signal is alternated between a DEP trapping (5 V amplitude, 100 kHz and a phase shift of 180° between neighboring electrodes) and a ROT signal (2.5 V amplitude, a swept frequency and 90° phase shift between neighboring electrodes) as shown in Fig. 2B. A similar approach was already presented by Rohani et al. on planar electrodes [28]. The ROT signal generates a torque on the cells and causes them to rotate (Fig. 2A middle). Cells in neighboring microcages rotate in the opposite direction, since the two electrodes of the rotation quadrupole are shared. A microscope image of the measurement in which four single cells are rotating within the array and another four cells are prevented from entering the trap is shown in Fig. 2B and Supporting Information Video 1. The frequency of the rotating electric field is swept between 10 kHz and 10 MHz in 25 logarithmic steps, the switching of the frequency can be seen in Supporting Information Video 2. Multiple single cells are rotating simultaneously in individual neighboring microcages, as shown in Supporting Information Video 4. Videos of the cells rotation are acquired with a frame rate between 5 and 25 Hz with a microscope camera (*Andor Neo sCMOS*) for 3 s for each electric signal frequency. The rotation speed of the cells rotating in the videos were acquired by an automatic pattern matching algorithm implemented in LabVIEW. Since T lymphocytes could not get held against the flow by cages of 40 and 80 μm interelectrode distance, the flow was stopped as soon as the T lymphocytes were within the microcage array. Hence, the nDEP force was sufficient to center them and their electrorotation spectra could be acquired, as shown in Supporting Information Video 3 and 4.

After the acquisition of the ROT spectra, the cells can be selectively released by turning off the electric signal at one of the exit electrodes. The exit barrier is thus reduced and the cell is carried away by the flow as sketched at the bottom of Fig. 2A.

If the chips are clogged with organic material like cells, cell fragments, or bacteria, they can be cleaned by flushing 1% sodium hypochlorite through the chip until all organic contamination are flushed away. Subsequently, the chip is flushed with culture medium and 100 mS/m solution in order to remove sodium hypochlorite residuals. Using this procedure, the chips could be used for several weeks during continuous experiments.

2.2 Dielectrophoretic force and electrorotation phenomenon

The dielectrophoretic force $\mathbf{F}_{\mathrm{DEP}}$, which balances the drag force of the fluid flow when the cell is stably trapped in the center of the microcage, is given by [34]

$$\langle F_{\mathrm{D}}\, E\, P\rangle = \pi\varepsilon_0\varepsilon_{\mathrm{m}}\, R^3\, Re[C\,M]\nabla\ E_{pk}^2 \tag{1}$$

Here, ε_0 is the absolute and ε_{m} is the relative permittivity of the medium; R is the cell radius and Re[CM] is the real part of the Clausius-Mossotti factor, which depends on the dielectric properties of the cell and the surrounding medium. $\nabla\ E_{pk}^2$ is the gradient of the electric field amplitude.

The speed of electrokinetically-induced rotation is [34]

$$\Omega = -\frac{\varepsilon_0\varepsilon_{\mathrm{m}}}{2\eta}\mathrm{Im}\,[C\,M]\ E^2 \tag{2}$$

with the medium viscosity η and Im[CM] the imaginary part of the Clausius-Mossotti factor. The Clausius-Mossotti factor's expression depends on the model used for the cell and is given by [35]

$$C\,M = \frac{\tilde{\varepsilon}_{\mathrm{p}} - \tilde{\varepsilon}_{\mathrm{m}}}{\tilde{\varepsilon}_{\mathrm{p}} + 2\tilde{\varepsilon}_{\mathrm{m}}};\quad \tilde{\varepsilon}_p = \tilde{C}_{\mathrm{mem}}\frac{3\,R\tilde{\varepsilon}_{\mathrm{cyto}}}{3\tilde{\varepsilon}_{\mathrm{cyto}} + 3\tilde{C}_{\mathrm{mem}}\,R} \tag{3}$$

$\tilde{\varepsilon}_p$, $\tilde{\varepsilon}_m$, $\tilde{\varepsilon}_{cyto}$are the complex permittivity of the particle, the suspending medium and the cytoplasm respectively, defined as: $\tilde{\varepsilon} = \varepsilon - i\sigma/\omega$ and $\tilde{C}_{mem}$ is the complex membrane capacitance defined as $\tilde{C} = C - iG/\omega$ with G the membrane conductance.

2.3 Simulations

Finite element simulations of the trap configurations are performed using COMSOL Multiphysics®. The electrode configurations as described in the microfabrication section are implemented in a cuboid of 400 μm per 400 μm per 50 μm. The flow in the device is simulated using laminar flow. The pressure difference between the inlet and the outlet is varied logarithmically between 0.001 and 0.1 mbar. The electric field is simulated using the electric current module. At the entrance electrodes an electric potential of +1 V and -1 V is applied and at the exit an electric potential of +5 V and -5 V is applied. The absolute value of the electric field is illustrated in the background color of the simulations shown in Fig. 3. In order to see if a specific cell type is getting trapped in the electrode configuration, we used the COMSOL® module for particle tracing in fluid flow. Particles with the cells' diameters are created at the high-pressure side of the cuboid. The drag force on the particles, as well as a self-implemented DEP force based on Eq. (1) are calculated from the laminar flow profile and the electric field. The particle trajectory of T lymphocytes (a), HEK 293 cells (b), M17 cells (c) and HeLa cells (d) in the 3D space for an interelectrode distance of 40 μm is calculated and illustrated in Fig. 3. The simulations for interelectrode distances of 20 μm and of 80 μm can be found in the Supporting Information (chapter 2).

In the nDEP regime at a frequency of 100 kHz, three trapping scenarios are possible depending on the microfluidic pressure and the trap size. First, the pressure is not sufficient and the cells do not overcome the entrance barrier (as shown in the Supporting Information chapter 2 for HEK 293, M17 and HeLa cells in an array of an interelectrode distance of 20 μm). Second, the cells are being trapped in the array, as shown in Fig. 3B–D and, third, the cells go through the

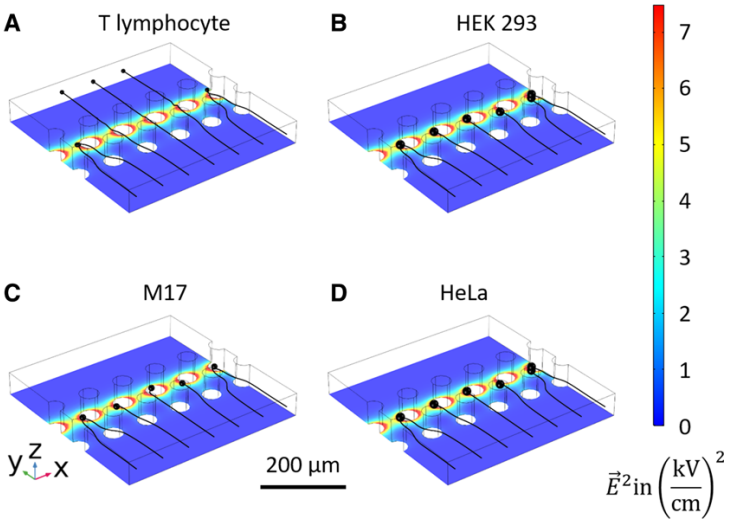

Figure 3. Finite element simulations of (A) human T lymphocytes, (B) HEK 293 cells, (C) M17 neuroblastoma and (D) HeLa cells in a microfluidic channel with an applied electric field of 5 V amplitude at the exit and 1 V amplitude at the entrance electrodes. The cells with a larger diameter (HEK 293 cells, M17 neuroblastoma and HeLa) (B–D) are trapped between the two electrode arrays with an interelectrode distance of 40 µm, while the T lymphocytes (A) are not. The square of the electric field is illustrated by a rainbow color coding. The particle's trajectory is shown in black.

array and are not trapped, as shown in 3A for T lymphocytes. The DEP trapping force depends on the cell type. HEK 293, M17 as well as HeLa cells can get retained against the flow in cages with interelectrode distance of 40 µm and 80 µm, as opposed to T lymphocytes. However, the latter are being trapped in cages with 20 µm interelectrode distance (See Supporting Information). On the other hand, for the same electrode configuration and pressure difference, HEK 293, M17, and HeLa cells are not entering the nDEP trap, but are blocked by the entry barrier. A more detailed description of the simulations models and methods used here can be found in [36].

3 Results and discussion

Cells of four different cell lines are injected and driven through the chips as described in the measurement procedure. We could trap four different cell types in our arrays controlling the entry of cells in individual cages. Multiple electrorotation spectra of different cell types were acquired. Finally, single cells were selectively released by lowering the dielectric barrier at the downstream electrodes.

3.1 Electrode diameter and trapping outcome

HeLa, HEK 293 cells, and M17 neuroblastoma are getting trapped in arrays with 40 µm and 80 µm inter electrode distance, while human immortalized T lymphocytes are not, which confirms the simulated expectations. A possible explanation for this could be the smaller cell radius R of such cells, which enters cubic into the DEP force. The force might not be large enough to overcome the fluid drag force. Reducing the interelectrode distance to 20 µm, not only the electric field becomes stronger, but as well its gradient ∇E_{pk}^2. This leads to a major increase of the trapping force and enable the trapping of the smaller T lymphocytes in the 20 µm interelectrode distance arrays. One of the main advantages of the presented electrode configuration vs. planar or octopole-based solutions is that it generates a homogeneous electric field over the complete channel height and, therefore, equivalent DEP force. The presented 3D electrodes generate efficiently a holding force in the middle of the channel, where the drag force is the strongest, due to the parabolic flow profile.

3.2 Electrorotation spectra of single cells

Using the protocol described in the measurement procedure, electrorotation spectra of 20 immortalized human T lymphocytes, 33 HEK 293 cells, 14 HeLa cells, and 29 M17 neuroblastoma were acquired. In total, over 140 single-cell spectra were recorded, including repeated measurements on the same cell to characterize the stability of the system. The average electrorotation spectra and its standard error of each population are shown in Fig. 4A. The spectra were normalized by dividing the speed of rotation in each point by the corresponding speed of rotation of the negative peak of each spectrum. The curves based on the extracted parameters are traced as a continuous line. The first acquired electrorotation spectrum of each cell was fitted to the single shell model, depicted in Fig. 4B, using a least square method. The cell radii were measured based on the optical images on the chip. Since our measurements were performed for frequencies below 10 MHz, the cytoplasm parameters hardly influence the electrorotation spectrum [35], and were therefore fixed to values reported in agreement with the literature. For T lymphocytes [3, 6, 37–39] and HEK 293 cells [40–43] a cytoplasm conductivity of 0.5 S/m and a cytoplasm permittivity of $78\varepsilon_0$ (same as water) are assumed.

Electrophoresis 2019, *40*, 1830–1838

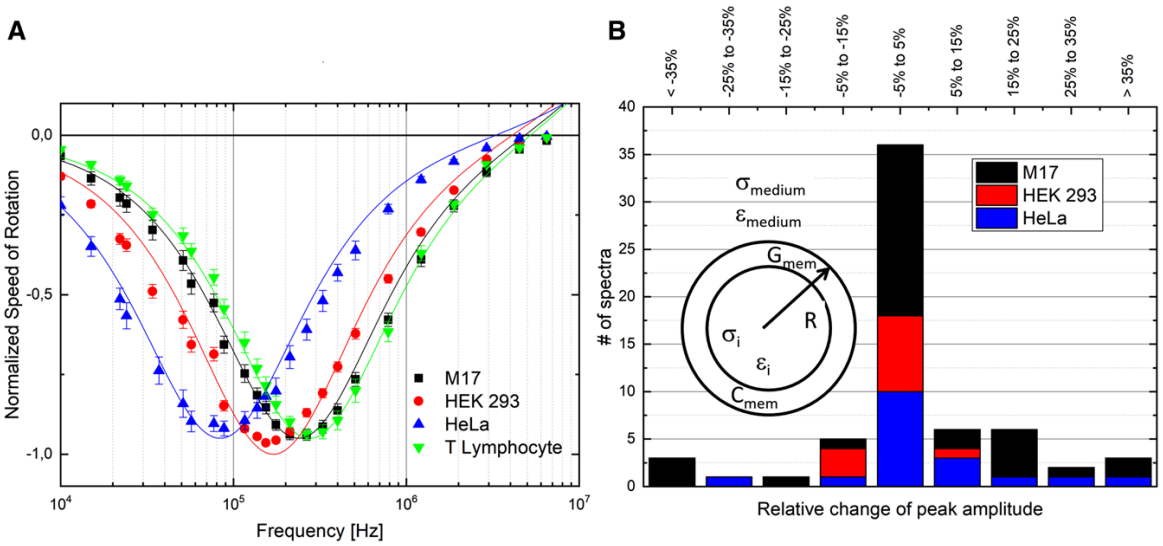

Figure 4. (A) Averaged and normalized electrorotation spectra and standard error of M17 neuroblastoma cells (black), HEK 293 (red) cells, HeLa (blue) cells, and human immortalized T lymphocytes (green) and their corresponding theoretical curves based on the extracted cell parameters. (B) Evaluation of the relative change of the absolute peak amplitude before and after the exposure to the rotating electric field for 5 min.

M17 neuroblastoma are fitted with these cytoplasm parameters too, since these are values commonly used for several cell lines. For HeLa cells a cytoplasm conductivity of 0.84 S/m was chosen as well as a cytoplasm permittivity of $60\varepsilon_0$ [44,45]. The membrane conductance was fixed to a value of 100 S/m^2 for T lymphocytes [38, 39] and 0.95 S/m^2 for HeLa cells [44]. For HEK 293 cells and M17 neuroblastoma the membrane conductance was kept floating. However, this parameter should have little influence on the electrorotation spectrum [35].

Consecutive acquisitions of a spectrum of a single HEK 293 cell every 5 min over 30 min time period were performed (Supporting Information chapter 1). The difference between the peak frequency overall was ±10%, which is lower than what was reported when using laser tweezers (approx. 50% in 40 min) [25]. In order to investigate the stability of the acquired spectra over time, electrorotation of 63 cells was performed before and after 5 min exposure to nDEP trapping and rotation within the array. The relative change of the peak amplitude is illustrated in Fig. 4B. 36 out of 63 cells experience a variation of less than ±5%, the other vary more. A possible explanation for the variation of the peak amplitude could be that the cells are observed in flow and possibly particulates in the solution or fluctuations within the solution might impact the rotation. However, the different contributions to this variation, on one side the sources of noise derived by the unprecise definition of the cell position and, on the other side, the actual changes of the rotation speed over time has to be further investigated.

The extracted membrane conductance data reported in Table 1 are in agreement with the literature (immortalized human T lymphocytes [3, 6, 37–39]; HEK 293 cells [40–43] and HeLa cells [44, 45]). This demonstrates the functionality and accuracy of the proposed system. However, the specific membrane capacitance of M17 neuroblastoma has, to our knowledge, not yet been reported in the literature. Hence, we could not compare the value we extracted, i.e., 7.49 ± 0.39 mF/m^2, to any previous work.

The number of cells possible to analyze at once is limited by the field of view of the used microscope. Using a 20X magnification with a field of view of 690 µm * 582 µm, we could observe 10 quadrupoles with 40 µm interelectrode distance could be acquired simultaneously. Moreover, using a magnification of 10X and arrays with an inter electrode distance of 20 µm, all 39 traps could be observed. The image quality would need to be further improved in order to acquire spectra with such low magnification. Filters could help improving the contrast [46]. Another possibility could be to use an automatized microscope stage [47] to observe all 39 quadrupoles with a 20X magnification in sequential videos.

At a cell concentration of 200 cells/ml and a flow rate of 1 µl/min, a new cell arrives every 12 s at a single trap, which leads to a total batch process time of about 90 s, including the spectra acquisition time. Including the statistical probability that some traps remain empty or occupied by multiple cells, this leads to a throughput of about 600 cells/h. Electrorotation systems are usually low throughput and therefore many papers do not mention this property explicitly. However, using the combination of a laser tweezer and electrorotation [26], a spectrum of a single cell is acquired in less than 3 min and the laser tweezer is applied for less than 5 min, which leads

Table 1. The extracted dielectric parameters and their standard error compared to the values found in literature. The values indicated with * were fixed. The cell radii were measured by optical observation of the cells in suspension

Cell Type	Radius (µm) (measured)	Cytoplasm conductivity σ_i (S/m)	σ_i reported in literature (S/m)	Cytoplasm permittivity ε_i	ε_i reported in literature	Membrane Conductance G_{mem} (S/m^2)	G_{mem} reported in literature (S/m^2)	Specific Membrane Capacitance C_{mem} (mF/m^2)	C_{mem} reported in literature (mF/m^2)	(Ref)
Human T-lymphocyte (n=20)	4.75 ± 0.12	0.5*	0.5	78*	78	100*	10–1000	8.05 ± 0.47	13.49 ± 4.72	[3]
			0.53 ± 0.1		100		-		7.01 ± 0.91	[6]
			0.65 ± 0.15		103.9 ± 24.5		-		10.5 ± 3.1	[38]
			1.06 ± 0.14		74.0 ± 5.3		100		12.1 ± 1.4	[39]
			0.3–1		85		-		11±1.1	[40]
HEK293 (n=33)	6.75 ± 0.5	0.5*	0.175 ± 0.014	78*	85 ± 15	$3 \bullet 10^{-14}$	0	9.81 ± 0.39	7.5 ± 0.3	[41]
			-		-		-		11.1 ± 0.8	[42]
			0.5		60		$7 \bullet 10^{-14}$		-	[43]
			0.408 ± 0.019		85 ± 4		≈0		7.94 ± 0.4	[44]
Hela (n=14)	8.74 ± 1.33	0.84*	-	60*	47	0.95*	0.95-1.2	17.51 ± 0.75	18.5 ± 2.6	[45]
			0.435–1.25		35–60		-		19	[46]
M17 (n=29)	6.30 ± 1.29	0.5*	-	78*	-	$5 \bullet 10^{-13}$	-	7.49 ± 0.39	-	

to an estimated throughput of 12 to 20 cells/h. Our system has a potential throughput, that we estimated to be 30 to 50 times higher.

3.3 Single-cell release

After the cells are trapped and analyzed, they can be released selectively. The chip design with separate interconnections for every electrode allows to change the signal applied by a single or several electrodes. Every interconnection on the chip is polarized by a dedicated pin to a PCB, where multiplexers direct the four signals supplied by the frequency generator to the corresponding electrodes. In order to release cells selectively, the signal of an exit electrode of the microcage is set to 0V. An experimental illustration of the release mechanism is shown in Fig. 5. The ability to turn off the electric signal of a single electrode using the switches on the PCB allows to turn off the retaining action of a microcage in which a cell is trapped. In 5(A–C) two cells are getting trapped in the array. In Fig. 5D the electric signal on the left electrode is turned off and the left cell is released. In Fig. 5E the electric signal of the right electrode is turned off and the cell on the right is released too, as shown in Supporting Information Video 5.

4 Concluding Remarks

In this paper, we present a full system for simultaneous label-free analysis of multiple single cell dielectric properties. Electrorotation spectra of arrayed single cells are acquired multiple while the cells are held against the flow in a wide microfluidic channel to monitor cells over time. Fabricated arrays with different cage size were designed to achieve efficient cell retention that facilitated the acquisition of more than a hundred spectra of single cells from four different cell types. The populations can be clearly differentiated and the extracted membrane capacitance for HeLa, HEK 293, and human immortalized T lymphocytes are in agreement with the values previously reported. Moreover, the dielectric properties of M17 neuroblastoma cells were characterized and reported for the first time by using electrokinetic based technique.

Currently we integrated 39 micro cages in our system, but could only observe 10 micro cages at a time in sufficient image resolution to acquire the spectra. Improving the imaging quality, decreasing the size of the cages and employing large-scale optical observation system could make it possible to observe many arrays on the same chip simultaneously. The microfluidic system itself is able to acquire spectra of non-adjacent quadrupoles independently from each other. However, the PCB, the image acquisition software as well as the application of the actuators electric signal would need to be redesigned in order start the spectra acquisition of the cells in an overlapping timely manner.

This research was funded by the Swiss National Science Foundation (205321_179086). We are thankful for the support of the

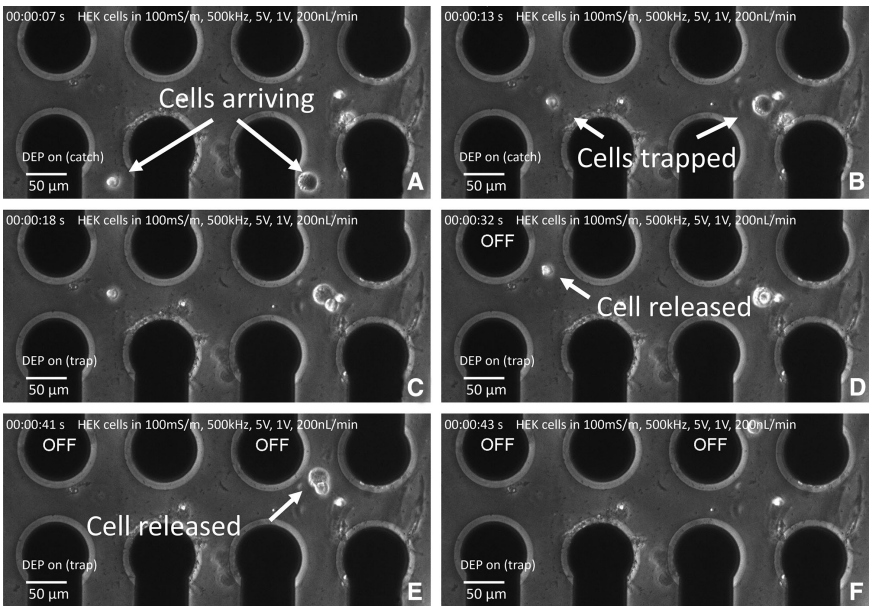

Figure 5. (A–D) Image series of the release mechanism. (A–C) two HEK 293 cells are trapped simultaneously in the microcage array. (E) Removing the electric signal on the very left electrode releases the left cell. (F), (G) Removing the signal on the electrode bordering the cell on the right releases it.

Center for Nano- and Microtechnology at EPFL where we fabricated the chips and the Scientific IT and Application Support cluster where we ran the finite elements simulations. We would like to thank Xavier Pierrat from the laboratory of Alexandre Persat at EPFL for supplying us with HeLa and HEK293 cells, the Ludwig Cancer center for supplying the human immortalized T lymphocytes and the laboratory of Hilal Lashuel at EPFL for supplying the M17 neuroblastoma. We are thankful for experimental support and discussion with Lilia Salimova, David Urban, Mathilde Roige and Sébastien Emery.

The authors have declared no conflict of interest.

5 References

[1] Pohl, H. A., Crane, J. S., *Biophys. J.* 1971, *11*, 711–727.

[2] Pohl, H. A., Pollock, K., Crane, J. S., *J. Biol. Phys.* 1978, *6*, 133–160.

[3] Han, S.-I., Joo, Y.-D., Han, K.-H., *Analyst* 2013, *138*, 1529–1537.

[4] Wang, X., Becker, F. F., Gascoyne, P. R. C., *Biochim. Biophys. Acta, Biomembr.* 2002, *1564*, 412–420.

[5] Huang, Y., Wang, X.-B., Becker, F. F., Gascoyne, P. R. C., *Biochim. Biophys. Acta Biomembr.* 1996, *1282*, 76–84.

[6] Huang, Y., Wang, X.-B., Gascoyne, P. R. C., Becker, F. F., *Biochim. Biophys. Acta Biomembr.* 1999, *1417*, 51–62.

[7] Huang, Y., Wang, X.-B., Holzel, R., Becker, F. F., Gascoyne, P. R. C., *Phys. Med. Biol.* 1995, *40*, 1789–1806.

[8] Kilchenmann, S. C., Rollo, E., Maoddi, P., Guiducci, C., *J. Microelectromech. Syst.* 2016, *25*, 425–431.

[9] Rollo, E., Tenaglia, E., Genolet, R., Bianchi, E., Harari, A., Coukos, G., Guiducci, C., *Biosens. Bioelectron.* 2017, *94*, 193–199.

[10] Voldman, J., Gray, M. L., Toner, M., Schmidt, M. A., *Anal. Chem.* 2002, *74*, 3984–3990.

[11] Manaresi, N., Romani, A., Medoro, G., Altomare, L., Leonardi, A., Tartagni, M., Guerrieri, R., *IEEE J. Solid-State Circuits* 2003, *38*, 2297–2305.

[12] Martinez-Duarte, R., *Electrophoresis* 2012, *33*, 3110–3132.

[13] Voldman, J., Toner, M., Gray, M. L., Schmidt, M. A., *J. Electrostat.* 2003, *57*, 69–90.

[14] Wang, L., Flanagan, L., Lee, A. P., *J. Microelectromech. Syst.* 2007, *16*, 454–461.

[15] Cho, Y. K., Kim, T. H., Lee, J. G., *J. Micromech. Microeng.* 2010, *20*.

[16] Xu, J., Wu, D., Hanada, Y., Chen, C., Wu, S., Cheng, Y., Sugioka, K., Midorikawa, K., *Lab Chip* 2013, *13*, 4608.

[17] Wang, C., Guangyao, J., Taherabadi, L. H., Madou, M. J., *J. Microelectromech. Syst.* 2005, *14*, 348–358.

[18] Martinez-Duarte, R., Gorkin, R. A., Abi-Samra, K., Madou, M. J., *Lab Chip* 2010, *10*, 1030–1043.

[19] Choi, J.-W., Rosset, S., Niklaus, M., Adleman, J. R., Shea, H., Psaltis, D., *Lab Chip* 2010, *10*, 783.

[20] Tay, F. E. H., Yu, L., Pang, A. J., Iliescu, C., *Electrochim. Acta* 2007, *52*, 2862–2868.

[21] Iliescu, C., Xu, G. L., Samper, V., Tay, F. E. H., *J. Micromech. Microeng.* 2005, *15*, 494–500.

[22] Rajaraman, S., Choi, S. O., Shafer, R. H., Ross, J. D., Vukasinovic, J., Choi, Y., Deweerth, S. P., Glezer, A., Allen, M. G., *J. Micromech. Microeng.* 2007, *17*, 163–171.

[23] Kilchenmann, S. C., Rollo, E., Bianchi, E., Guiducci, C., *Sens. Actuators B* 2013, *185*, 713–719.

[24] Gasperis, G.De., Wang, X., Yang, J., Becker, F. F., Gascoyne, P. R. C., *Meas. Sci. Technol.* 1998, *9*, 518–529.

[25] Reichle, C., Schnelle, T., Müller, T., Leya, T., Fuhr, G., *Biochim. Biophys. Acta Bioenerg.* 2000, *1459*, 218–229.

[26] Cristofanilli, M., De Gasperis, G., Zhang, L., Hung, M. C., Gascoyne, P. R. C., Hortobagyi, G. N., *Clin. Cancer Res.* 2002, *8*, 615–619.

[27] Hughes, M. P., *Phys. Med. Biol.* 1998, *43*, 3639-3648.

[28] Rohani, A., Varhue, W., Su, Y. H., Swami, N. S., *Electrophoresis* 2014, *35*, 1795–1802.

[29] Trainito, C. I., Français, O., Le Pioufle, B., *Electrophoresis* 2015, *36*, 1115–1122.

[30] Fuhr, G., Müller, T., Baukloh, V., Lucas, K., *Hum. Reprod.* 1998, *13*, 136–141.

[31] Reichle, C., Müller, T., Schnelle, T., Fuhr, G., *J. Phys. D Appl. Phys.* 1999, *32*, 2128–2135.

[32] Ren, Y., Huang, S. H., Mosser, S., Heuschkel, M. O., Bertsch, A., Fraering, P. C., Chen, J. J. J., Renaud, P., *Micromachines* 2015, *6*, 1923–1934.

[33] Wang, X. B., Huang, Y., Gascoyne, P. R. C., Becker, F. F., Hölzel, R., Pethig, R., *Biochim. Biophys. Acta Biomembr.* 1994, *1193*, 330–344.

[34] Pethig, R., *Dielectrophoresis*, John Wiley & Sons, Ltd, Chichester, UK, 2017.

[35] Gascoyne, P. R. C., Becker, F. F., Wang, X. B., *Bioelectrochem. Bioenerg.* 1995, *36*, 115–125.

[36] Keim, K., Gonçalves, A., Guiducci, C., *Proc. 2018 COMSOL Conf., Lausanne*, 2018; https://www.comsol.nl/conference2018/download-paper/62311.pdf.

[37] Pethig, R., Bressler, V., Carswell-Crumpton, C., Chen, Y., Foster-Haje, L., García-Ojeda, M. E., Lee, R. S., Lock, G. M., Talary, M. S., Tate, K. M., *Electrophoresis* 2002, *23*, 2057–2063.

[38] Yang, J., Huang, Y., Wang, X., Wang, X. B., Becker, F. F., Gascoyne, P. R., *Biophys. J.* 1999, *76*, 3307–3314.

[39] Gascoyne, P. R. C., Wang, X.-B., Huang, Y., Becker, F. F., *IEEE Trans. Ind. Appl.* 1997, *33*, 670–678.

[40] Zimmermann, D., Kiesel, M., Terpitz, U., Zhou, A., Reuss, R., Kraus, J., Schenk, W. A., Bamberg, E., Sukhorukov, V. L., *J. Membr. Biol.* 2008, *221*, 107–121.

[41] Gentet, L. J., Stuart, G. J., Clements, J. D., *Biophys. J.* 2000, *79*, 314–320.

[42] Soffe, R., *Discontinuous Dielectrophoresis Enabled Investigation of High Shear Stress Flows on Intracellular Calcium Signalling of Non-Adherent Cells*, PhD Thesis, Royal Melbourne Institute of Technology, Melbourne, 2016.

[43] El-Gaddar, A., Frénéa-Robin, M., Voyer, D., Aka, H., Haddour, N., Krähenbühl, L., *Biophys. J.* 2013, *104*, 1805–1811.

[44] Asami, K., Takahashi, Y., Takashima, S., *Biophys. J.* 1990, *58*, 143–148.

[45] Jen, C., Chen, T., *Biomed. Microdevices* 2009, *11*, 597–607.

[46] Schaeper, M., Schmidt, R., Kostbade, R., Damaschke, N., Gimsa, J., *J. Phys. D Appl. Phys.* 2016, *49*, 265402.

[47] Cornaglia, M., Mouchiroud, L., Marette, A., Narasimhan, S., Lehnert, T., Jovaisaite, V., Auwerx, J., Gijs, M. A. M., *Sci. Rep.* 2015, *5*, 1–13.

On-chip technology for single-cell arraying, electrorotation-based analysis and selective release
Supplementary Information
Kevin Keim, Mohamed Z. Rashed, Samuel C. Kilchenmann, Aurélien Delattre, António F. Gonçalves, Paul Éry and Carlotta Guiducci

On-chip technology for single-cell arraying, electrorotation-based analysis and selective release

Supplementary information

Kevin Keim, Mohamed Z. Rashed, Samuel C. Kilchenmann, Aurélien Delattre, António F. Gonçalves, Paul Éry and Carlotta Guiducci

Laboratory of Life Sciences Electronics – École Polytechnique Fédérale de Lausanne, Switzerland

1. Evaluation of the stability of the acquisition of electrorotation spectra

Experiments were performed to show the stability of the electrorotation system as well to verify the functionality of the proposed system.

A study on effect of changing the applied voltage on the speed of rotation was conducted. The electrorotation spectra of a single HEK 293 cell were acquired at different applied voltages, as shown in Supplementary Figure 1 (a). The speed of rotation increases quadratically with increasing applied voltage, as predicted by eq. 2 in the main manuscript.

Moreover, electrorotation spectra of a single HEK 293 cell were acquired every 5 minutes over a duration of 30 minutes while the cell was constantly kept rotating in an electric field. As can be seen from the spectra shown in Supplementary Figure 1 (b), the electrorotation spectrum remains stable over the whole duration of the experiment. Changes of the speed of rotation are of less than ±10% overall.

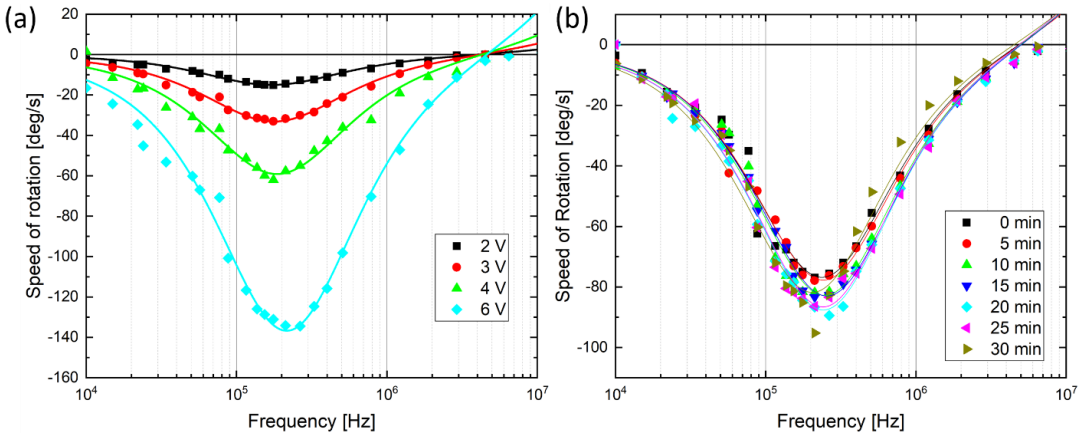

Supplementary Figure 1 (a) Non-normalized electrorotation spectra of a HEK 293 cell for different applied amplitude of the signal. (b) Non-normalized spectra of a single HEK 293 cell. 7 spectra were acquired subsequentially with 5 minutes interval for 30 minutes.

In the main manuscript we present averaged spectra of 17 T lymphocytes, 33 HEK 293, 14 HeLa and 29 M17 neuroblastoma. The data shown contains only the data of the first electrorotation spectrum of each cell. The original spectra of each cell was normalized by dividing it by the maximum speed of rotation as can be shown in Supplementary Figure 2.

On-chip technology for single-cell arraying, electrorotation-based analysis and selective release
Supplementary Information

Kevin Keim, Mohamed Z. Rashed, Samuel C. Kilchenmann, Aurélien Delattre, António F. Gonçalves, Paul Éry and Carlotta Guiducci

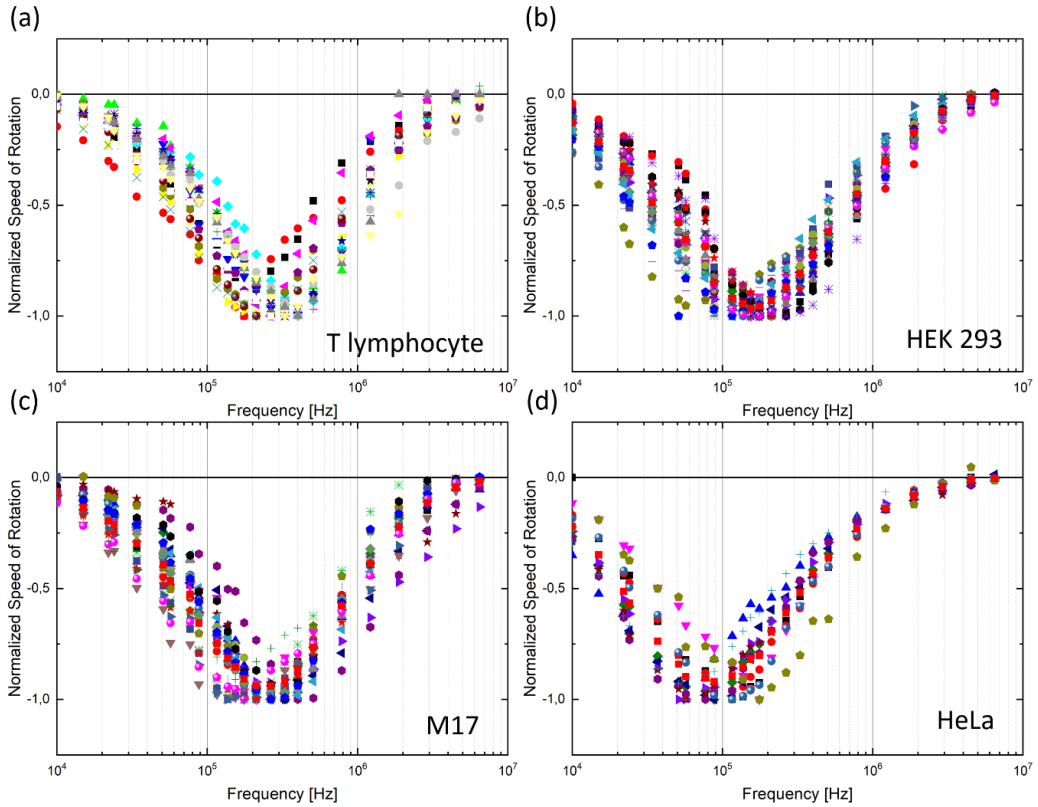

Supplementary Figure 2 Measured electrorotation spectra of (a) 20 immortalized human T lymphocytes, (b) 33 HEK 293 cells, (c) 29 M17 neuroblastoma cells, and (d) 14 HeLa cells. Normalized by the maximum rotation speed.

On-chip technology for single-cell arraying, electrorotation-based analysis and selective release
Supplementary Information
Kevin Keim, Mohamed Z. Rashed, Samuel C. Kilchenmann, Aurélien Delattre, António F. Gonçalves, Paul Éry and Carlotta Guiducci

2. Finite element simulations

The finite element simulations presented in the main manuscript were performed for all cell types (T lymphocytes, HEK 293, M17 and HeLa cells) at different medium conductivities (1 mS/m, 10 mS/m, 100 mS/m, and 1000 mS/m), different electric field frequencies (10 kHz, 100 kHz, 1 MHz and 10 MHz), different pressure differences (0.001 mbar, 0.01 mbar, 0.05 mbar and 0.1 mbar) and different electrode layouts (interelectrode distances of 20 µm, 40 µm and 80 µm). The trapping behavior of cells of the different configurations was investigated. It turns out that at conditions which are convenient for combined electrorotation and DEP trapping experiments (100 mS/m and 100 kHz DEP signal) HEK 293, M17 and HeLa cells are behaving very similar. They are being trapped at a medium pressure difference (0.01 mbar at an inter electrode of 80 µm and 0.05 mbar at an inter electrode of 80 µm), as shown in Supplementary Figure 3(e-h) and in the main manuscript. T lymphocytes in contrast are being slowed down, but are finally flowing through the traps. However, in smaller cell traps as with an inter electrode distance of 20 µm and a pressure difference of 0.05 mbar, T lymphocytes are getting trapped, while the other cell types are partially not overcoming the first dielectric barrier as shown in Supplementary Figure 3 (b-d).

The main reason for the different trapping behavior is related to the size of the cells, since the DEP force depends on the cell radius cube, as shown in eq. (1) in the main manuscript. T lymphocytes are the smallest cells investigated in this study, therefore, they are the hardest to trap.

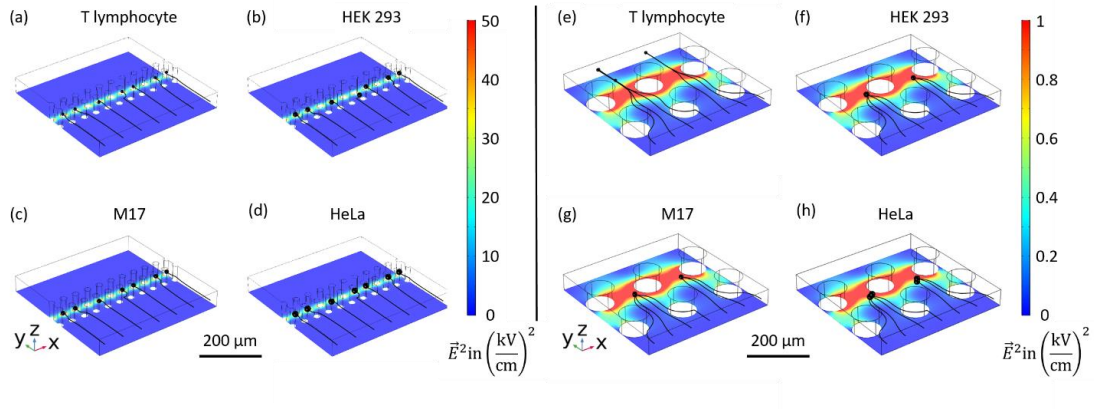

Supplementary Figure 3 Finite element simulations of the trajectory of different cell types in a microfluidic channel. The 3D electrodes in the middle of the microfluidic channel have a diameter and an interelectrode distance of 20 µm (a-d) and of 80 µm (e-h). The applied voltage at the exit electrodes is 5 V amplitude and at the entrance electrodes 1 V amplitude. The squared electric field in the microfluidic channel is illustrated in the rainbow colors. The cells trajectory in black illustrates that T lymphocytes are (a) getting trapped within the electrode array of an inter electrode distance of 20 µm, while HEK 293, M17 and HeLa cells (b-d) partially blocked by the lower entrance barrier and do not enter the micro cages In an array of an inter electrode distance of 80 µm T lymphocytes are not getting trapped (e), while the other cells are getting trapped (f-h).

On-chip technology for single-cell arraying, electrorotation-based analysis and selective release
Supplementary Information

Kevin Keim, Mohamed Z. Rashed, Samuel C. Kilchenmann, Aurélien Delattre, António F. Gonçalves, Paul Éry and Carlotta Guiducci

3. Printed Circuit Board

A printed circuit board (PCB) was designed in order to address every electrode on the chip separately. The PCB has a whole cut in the middle to facilitate the vision of the chip under inverted microscope as shown in Supplementary Figure 4.

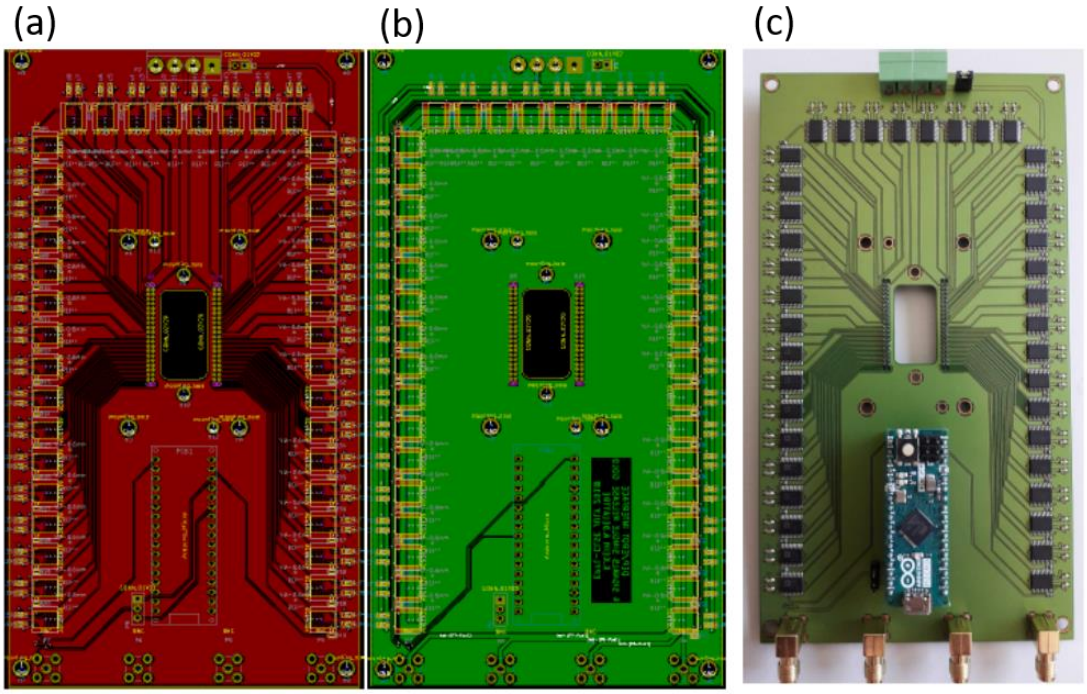

Supplementary Figure 4 Top views of the PCB. (a) Copper mask for the PCB showining the connection lines from the springloaded contacts on the left and right sides of the cut hole connecting the electrodes to the multiplexers that are selectively switched in order to address a specific elctrode. (b) The connections lines of the bottom part of the PCB from where the four signals supplied from the frequency generator through the SMB connectors- at the bottom of the PCB- to the multiplexers (c) Photograph of the final fabricated and assembled PCB. Connection to the frequency generator are achieved through the four SMB connectors at the bottom. The power is supplied by the green connector at the top of the PCB. The Arduino controller is placed central below the cut hole for the chip observation and is connected via mini USB to the controlling computer.

On-chip technology for single-cell arraying, electrorotation-based analysis and selective release Supplementary Information

Kevin Keim, Mohamed Z. Rashed, Samuel C. Kilchenmann, Aurélien Delattre, António F. Gonçalves, Paul Éry and Carlotta Guiducci

On the left and the right side of the hole cut, 40 spring loaded contacts are placed to connect each electrode on the chip individually to the PCB. Etched copper lines shown in Supplementary Figure 4 (a) are connecting each contact to an exit of an ADG1439 multiplexer.

Supplementary Figure 5 Control interface of the LabView program controlling the multiplexers. The operator can address any electrode by selecting the signal type 1,2,3,4 or 0 (0 corresponds to no signal applied) from a selection menu. By clicking send, the new signal is updated by the multiplexers. For electrorotation experiments a circular/anticircular order for one quadrupole of electrodes has to be chosen.

Each multiplexer can route four different input signals (or no signal) to two outputs. Therefore, by such MUX we can decide which of the four signals supplied by the frequency generator is routed to which electrode, or if there is no signal at all applied (OFF state). The four signals from the frequency generator are connected to the PCB by four SMB connectors as shown at the bottom of Supplementary Figure 4 (c). Each signal line supplies every multiplexer with all four signals. In Supplementary Figure 4 (b), below the hole cut for observation, the wiring for the Arduino (microcontroller) is shown. Two lines connect all ADG1439 in series. One line is used to provide the clock signal, which gives the timing for the switches and the other line is the control line, which ultimately passes the signal from the Arduino to the switches. The Arduino is controlled by a LabView interface, as shown in Supplementary Figure 5.

On-chip technology for single-cell arraying, electrorotation-based analysis and selective release
Supplementary Information

Kevin Keim, Mohamed Z. Rashed, Samuel C. Kilchenmann, Aurélien Delattre, António F. Gonçalves, Paul Éry and Carlotta Guiducci

4. Field of vision and parallelized acquisition of electrorotation spectra

As discussed in the main manuscript, the field of vision with a 20X magnification is 690 µm × 582 µm and therefore 10 microcages of an electrode array of a 40 µm inter electrode distance can be observed under the microscope as shown in Supplementary Figure 6.

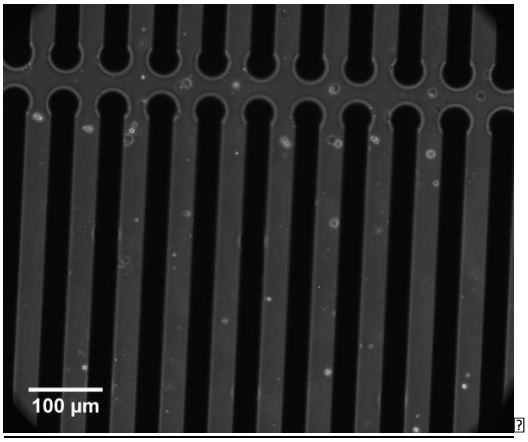

Supplementary Figure 6 Field of vision on an electrode array of 40 µm inter electrode distance with HeLa cells flowing inside the microchannel, using a 20x magnification. The field of vision with this magnification is 690 µm × 582µm and 10 quadrupoles can be visualized.

Electrorotation spectra of multiple single cells can be acquired simultaneously as shown for: three M17 neuroblastoma cells (Supplementary Figure 7); 3 human immortalized T lymphocytes (Supplementary Figure 8) and a HeLa cell and a M17 neuroblastoma cell (Supplementary Figure 9).

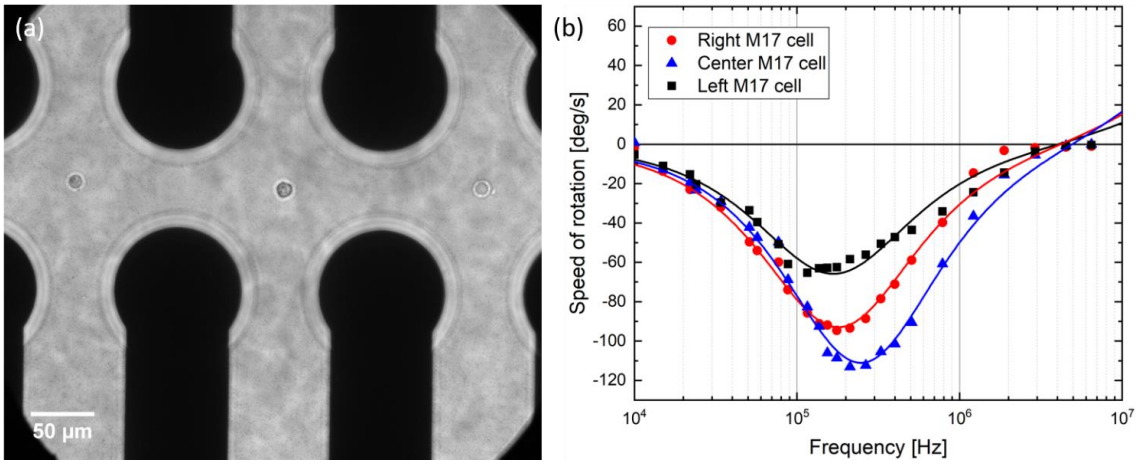

Supplementary Figure 7 (a) Three M17 neuroblastoma cells simultaneously rotating in three individual neighboring quadrupole cages of the array. (b) the corresponding electrorotation spectra of the three cells shown in (a).

On-chip technology for single-cell arraying, electrorotation-based analysis and selective release
Supplementary Information
Kevin Keim, Mohamed Z. Rashed, Samuel C. Kilchenmann, Aurélien Delattre, António F. Gonçalves, Paul Éry and Carlotta Guiducci

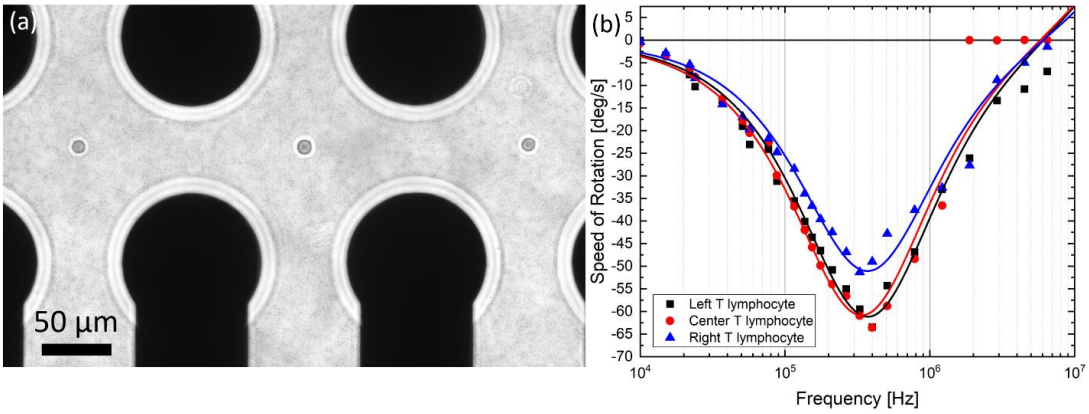

Supplementary Figure 8 (a) Three human immortalized T lymphocytes simultaneously rotating in three separate electrode cages of the array. (b) the corresponding electrorotation spectra of the Three cells shown in (a).

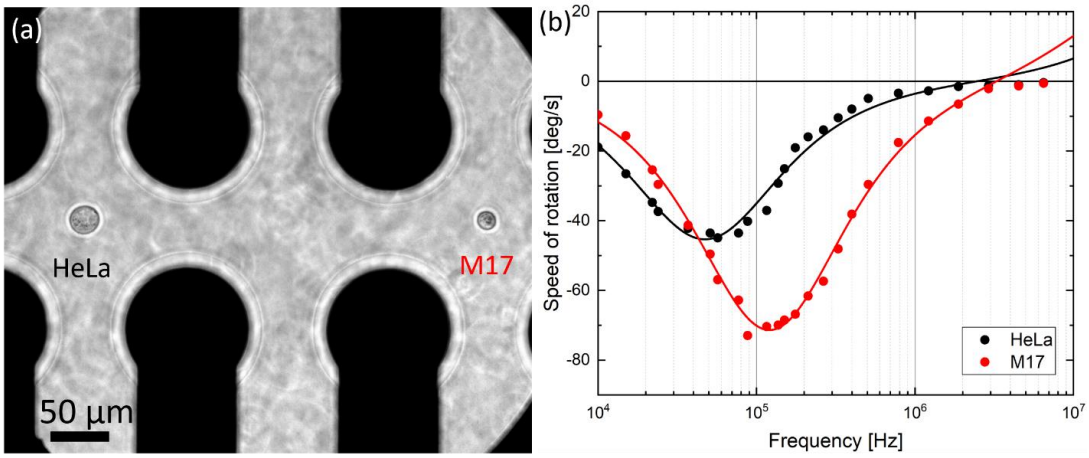

Supplementary Figure 9 (a) HeLa cell and M17 neuroblastoma cells simultaneously trapped and rotating in two individual cages of the array. (b) corresponding electrorotation spectra of the two cells

On-chip technology for single-cell arraying, electrorotation-based analysis and selective release
Supplementary Information
Kevin Keim, Mohamed Z. Rashed, Samuel C. Kilchenmann, Aurélien Delattre, António F. Gonçalves, Paul Éry and Carlotta Guiducci

5. Bibliography

[1] J. Voldman, M. Toner, M. L. Gray, and M. A. Schmidt, "Design and analysis of extruded quadrupolar dielectrophoretic traps," *J. Electrostat.*, vol. 57, no. 1, pp. 69–90, 2003.

[2] L. Wang, L. Flanagan, and A. P. Lee, "Side-wall vertical electrodes for lateral field microfluidic applications," *J. Microelectromechanical Syst.*, vol. 16, no. 2, pp. 454–461, 2007.

[3] Y. K. Cho, T. H. Kim, and J. G. Lee, "On-chip concentration of bacteria using a 3D dielectrophoretic chip and subsequent laser-based DNA extraction in the same chip," *J. Micromechanics Microengineering*, vol. 20, no. 6, 2010.

[4] J. Xu *et al.*, "Electrofluidics fabricated by space-selective metallization in glass microfluidic structures using femtosecond laser direct writing," *Lab Chip*, vol. 13, no. 23, p. 4608, 2013.

[5] Chunlei Wang, Guangyao Jia, L. H. Taherabadi, and M. J. Madou, "A novel method for the fabrication of high-aspect ratio C-MEMS structures," *J. Microelectromechanical Syst.*, vol. 14, no. 2, pp. 348–358, Apr. 2005.

[6] R. Martinez-Duarte, R. A. Gorkin, K. Abi-Samra, and M. J. Madou, "The integration of 3D carbon-electrode dielectrophoresis on a CD-like centrifugal microfluidic platform," *Lab Chip*, vol. 10, no. 8, pp. 1030–1043, 2010.

[7] J.-W. Choi, S. Rosset, M. Niklaus, J. R. Adleman, H. Shea, and D. Psaltis, "3-Dimensional Electrode Patterning Within a Microfluidic Channel Using Metal Ion Implantation," *Lab Chip*, vol. 10, no. 6, p. 783, 2010.

[8] F. E. H. Tay, L. Yu, A. J. Pang, and C. Iliescu, "Electrical and thermal characterization of a dielectrophoretic chip with 3D electrodes for cells manipulation," *Electrochim. Acta*, vol. 52, no. 8 SPEC. ISS., pp. 2862–2868, 2007.

[9] C. Iliescu, G. L. Xu, V. Samper, and F. E. H. Tay, "Fabrication of a dielectrophoretic chip with 3D silicon electrodes," *J. Micromechanics Microengineering*, vol. 15, no. 3, pp. 494–500, 2005.

[10] S. Rajaraman *et al.*, "Microfabrication technologies for a coupled three-dimensional microelectrode, microfluidic array," *J. Micromechanics Microengineering*, vol. 17, no. 1, pp. 163–171, 2007.

[11] S. C. Kilchenmann, E. Rollo, E. Bianchi, and C. Guiducci, "Metal-coated silicon micropillars for freestanding 3D-electrode arrays in microchannels," *Sensors Actuators B Chem.*, vol. 185, pp. 713–719, Aug. 2013.

[12] S. C. Kilchenmann, E. Rollo, P. Maoddi, and C. Guiducci, "Metal-Coated SU-8 Structures for High-Density 3-D Microelectrode Arrays," *Journal of Microelectromechanical Systems*, vol. 25, no. 3, pp. 425–431, Jun-2016.

[13] K. Keim, A. Gonçalves, and C. Guiducci, "Trapping of Single-Cells Within 3D Electrokinetic Cages," in *Proceedings of the 2018 COMSOL Conference in Lausanne*, 2018.

Discussion of the potential throughput of the system

The parallelized electrorotation system presented here can help automatize cell analysis by electrorotation. It shows how a parallel in-flow operation can be realized using three dimensional electrodes in microfluidic channels. As mentioned in the paper, the system currently features 39 micro-cages. Upscaling does not require specific technological challenges. In the current version, the device has a significant increase in throughput to comparable systems, with up to $600 cells/hour$, as is shown in the following calculation.

The typical cells's concentration in the experiments was

$$C_{cell} = 200.000 \frac{cells}{ml} \tag{3.4}$$

The flow rate was of

$$Q = 200 \frac{nl}{min} - 1 \frac{\mu l}{min} \tag{3.5}$$

Consequently, at a high flow rate, the cells reach the array with a frequency of

$$f_{array} = C_{cell} \cdot Q = 200.000 \frac{cells}{ml} \cdot 1 \frac{\mu l}{min} = 200 \frac{cells}{min} \tag{3.6}$$

Which means that cells reach each of the 39 traps with a frequency of

$$f_{trap} = \frac{f_{arrray}}{39} \approx 5 \frac{cells}{min} \tag{3.7}$$

Which leads to an average loading time of

$$T_{trap} = \frac{1}{f_{trap}} = 12s \tag{3.8}$$

This means that on average each of the 39 traps is reached by one cell within 12s, and that overall 39 cells are reaching the array in that time. Assuming a random distribution, the probability of one of the traps to be reached by $k = [0,39]$ cells in this time is

$$P_k = \binom{n}{k} p^k \cdot (1-p)^{(n-k)} \tag{3.9}$$

with $n = 39$ the number of traps, $p = 1/39$ the probability of a cell being trapped in a specific trap. Consequently, the probability P_k of k cells occupying one single trap out of the 39 traps is:

$$P_0 = 0.36 \qquad P_1 = 0.37 \qquad P_2 = 0.19 \qquad P_3 = 0.06 \qquad P_4 = 0.01 \qquad P_{(>4)} = 0.01 \tag{3.10}$$

If a trap is occupied by multiple cells, the single exit barrier can be opened and the cells can be released. After release, the trap can be reloaded by a single cell (while the other cages stay closed). Assuming a measurement time for the acquisition of the spectrum of

$$t_{measure} = 75s \tag{3.11}$$

and a loading time of

$$t_{load} = 12s \tag{3.12}$$

a total batch time can be calculated as

$$t_{batch} = t_{measure} + t_{load} = 86s \tag{3.13}$$

Assuming that we can only use the traps when only one cell is present - so neglecting the possibility to reload and adjust the trap - the throughput can be calculated as

$$Throughput = (39 \cdot P_1)/t_{batch} = 596 cells/h \tag{3.14}$$

Comparable systems, usually do not comment on the throughput, since the system are not made for a high throughput anyways. However, based on our own calculations for instance on the paper by Cristofanilli and coauthors [93], considering a declared acquisition time of a ROT spectrum of $t_{min} < 3min$ as the lower boundary and maximal application time of the laser tweezer of $t_{max} < 5min$, their throughput should be between 12 and $20 cells/h$, since they only have a single trap. Our system has a theoretical throughput 30 to 50 times higher.

Our system demonstrate the possibility to perform single-cell electrorotation on an array. It is possible to further increase the number of cages, leading to higher throughput devices. Instead when using technologies like laser tweezers the scale is limited by the number of cages that can be controlled in parallel by this centering method.

3.2.3 Investigation of the effect of osmolarity on the membrane capacitance and real-time analysis of the membrane integrity

In the previous section the ability of the system to analyze multiple cells in flow in parallel were demonstrated. Due to the high sensitivity of electrorotation to the membrane capacitance [90], this system might not only be eligible to distinguish between populations of different cell lines, but could as well be used to investigate sub populations based on their membrane properties. This could potentially be used to investigate protein deposition on the membrane of cells in real-time.

In order to characterize the performance of the system to extract the cell membrane capacitance value, we carried out a so-called osmolarity study. We performed electrorotation of the same cell type in solutions of different osmolarity in order to induce a change of the membrane capacitance similarly to what is reported by [118]. Membrane changes within the same cell populations due to the different osmolarity of the surrounding medium are recorded.

Dielectrophoresis can influence the viability of cells, depending on the applied frequency, the electric field and the medium conductivity. In order to reveal non viable cells, 0.1% erythrosine B dye was added to the measurement solution. Additionally, this enabled to investigate the viability in real-time, based on the dye readout as well as on the changes in the electrorotation spectrum.

The results on this are presented in 2019 in the conference proceeding of the 23rd International Conference on Miniaturized Systems for Chemistry and Life Sciences (microTAS) in Basel, Switzerland under the title "Observation of membrane changes and viability of cells in a parallel electrorotation platform" (Kevin Keim, Mohammed Z. Rashed, Carlotta Guiducci) [156].

Contributions

The experiments were carried out by Mohammed Z. Rashed under the instruction of Kevin Keim. The manuscript was written by Kevin Keim and edited by Mohammed Z. Rashed and Carlotta Guiducci.

OBSERVATION OF MEMBRANE CHANGES AND VIABILITY OF CELLS IN A PARALLEL ELECTROROTATION PLATFORM

Kevin Keim, Mohamed Z. Rashed, and Carlotta Guiducci
École Polytechnique Fédérale de Lausanne, Switzerland

ABSTRACT

Multiple single cells are analyzed in parallel by electrorotation within a microfluidic channel. In this work, the effects of increased osmotic stress was investigated on HEK 293 cells by means of electrorotation analysis. The induced size change and the possible modification in the membrane morphology were characterized by optical and dielectric characterization via the electrorotation experiments. Moreover, cell viability was evaluated in real-time by the use of Erythrosin B dyes diluted in the measurement medium. We could observe that a loss of the cell membrane sealing function appears concomitantly to a drop of the membrane capacitance.

KEYWORDS: Cell viability, Electrorotation, Osmolarity, Membrane folding

INTRODUCTION

Suspending cells in solutions of different osmolarity induces a size change that derives by the desire to compensate the osmolarity gradient by exchanging solution through the membrane. For instance, a higher osmolarity of the solution will induce a decrease of the cell size which might result in an increased complex morphology and membrane folding. Such effect has been previously observed on DS19 murine erythroleukemia cells together with a corresponding increase of the membrane capacitance characterized by electrorotation [1]. We recently developed a technology to obtain the electrorotation spectra of multiple single cells arranged in an array of identical nDEP microcages [2]. In the present contribution, we report the dielectric characterization of multiple cells suspended in solution of four different osmolarity values and the corresponding difference in membrane capacitance. Moreover, we observe the effect on cell viability in real-time by mixing Erythrosin B dye with the solution, visualizing the uptake of such marker by the cell during the electrorotation measurements.

The platform, which is capable of individual addressing, trapping and releasing of 39 single cells in separated dielectrophoretic single-cell microcages [4], is based on a 3D-electrodes technology fabricated out of metal-covered SU-8 cores, developed previously in our laboratory [3].

EXPERIMENTAL

HEK 293 cells are cultured in DMEM medium and are detached from the surface using Trypsin prior to the experiment. Subsequently, they are suspended in a measurement solution with a conductivity of σ = 100 mS/m and 0.1% Erythrosine B dye with adapted osmolarity between 100 mOs/kg (hypotonic) and 400 mOs/kg (hypertonic). The cells are flown through the device, trapped by DEP force in the microcages and made rotate to acquire their electrorotation spectrum. The dye stains the cell cytoplasm once the membrane functionality fails, giving an indication of the cell viability in real-time during the electrorotation measurements.

RESULTS AND DISCUSSION

Multiple electrorotation spectra of HEK 293 cells in different osmolarity solutions are acquire and averaged, as shown in Fig. 1(a). The cells dielectric parameters can be obtained by fitting the single-shell model to each single-cell spectrum [5].

The osmotic stress influences the average cell radius – measured by optical observation while in suspension in the microfluidic chip - and the extracted value of the plasma membrane capacitance as shown in Fig. 1(b). Plotting the membrane capacitance versus the inverted cell radius square, as shown in Fig. 2(a), we find a total membrane capacitance of HEK 293 cells of $C_{tot} = 8.9 \pm 1.4$ mF extracted from the linear regression using $C_{tot} = 4\pi R^2 C_{mem}$. We observe an increase of membrane capacitance and decreasing of cell radius related to a higher osmolarity of the solution. Previously, Wang and coworkers [1] reported as well that the induced radius change due to osmotic stress results in the increase of the membrane capacitance per surface area of the cell, C_{mem} and that this could related to enhanced membrane morphology of the cells.

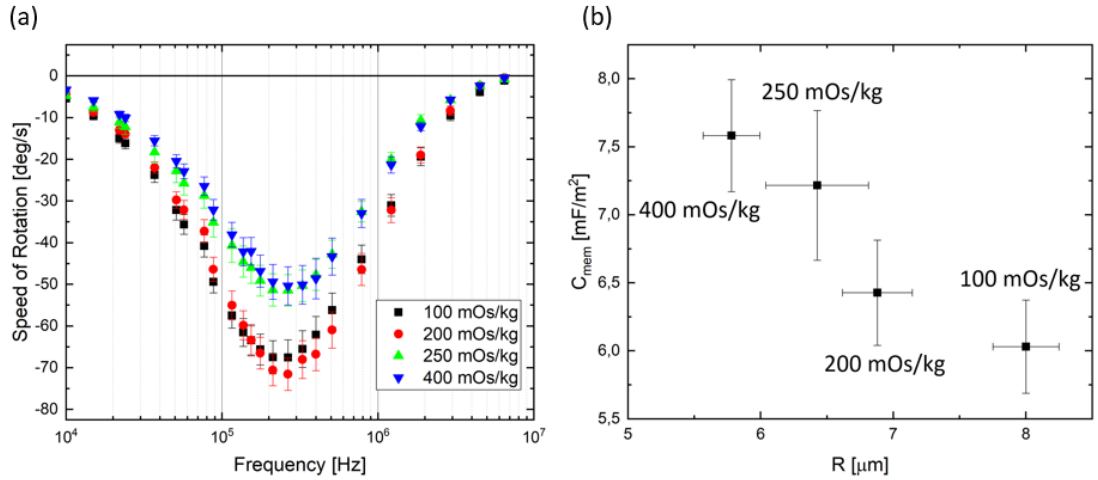

Figure 1: (a) Averaged electrorotation spectra of more than ten HEK 293 cells per single condition of osmolarity value of the solution. (b) The extracted average membrane capacitance and average cell radius for each osmolarity.

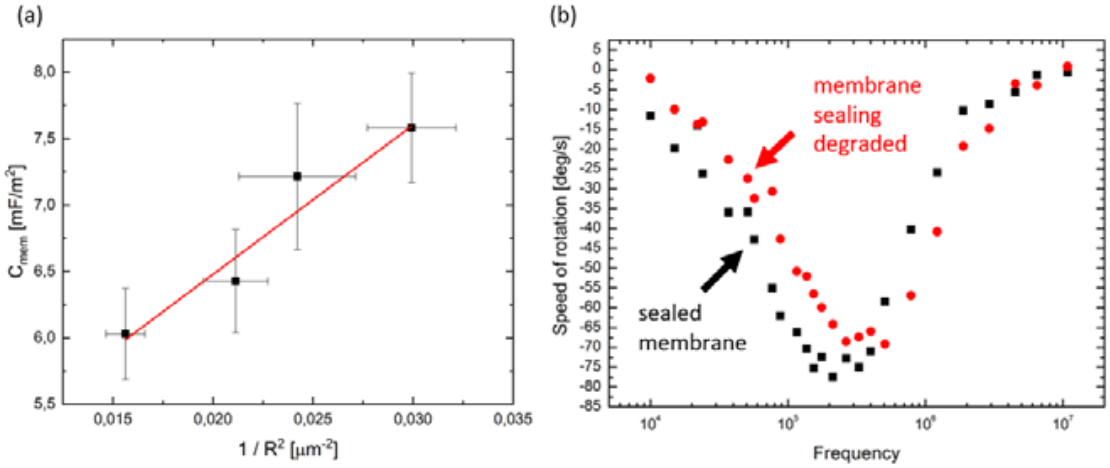

Figure 2: (a) Membrane capacitance depends linearly on $1/R^2$ (linear regression shown in red). (b) The loss of membrane sealing is effecting the electrorotation spectrum (one HEK 293 cell characterized in σ = 100 mS/m and an osmolarity of 150 mOs/kg). The negative peak of the same cell shifts to higher frequencies and the fitted membrane capacitance drops from 4.7 mF/m^2 to 3.7 mF/m^2 after cell death.

We characterized the effect of osmotic stress on cells viability by suspending them in the specific osmolarity solution and 0.1% Erythrosine B dye in petri dishes. The viability was accessed by counting the stained (dead) and unstained (alive) cells after one hour. The outcome in percentage of cells affected is presented in Tab. 1. We performed electrorotation experiments in presence of Erythrosin B dye as well on chip to assess the cell viability in real-time. We first performed electrorotation measurements in low conductivity (σ = 100 mS/m) solution. The cells remained always viable during the first spectrum and the intake of the dye by the cell happened only after the acquisition of several electrorotation spectra or not at all. As an example, a cell dye intake was observed in real-time with a shift of the negative peak of the spectrum to higher frequencies (Fig. 2(b)). The fitted membrane capacitance of the cell after membrane sealing failure decreased from 4.7 mF/m^2 to 3.7 mF/m^2 in a measurement solution of σ = 100 mS/m and an osmolarity of 150 mOs/kg.

However, in DMEM, which has physiological values of ionic force, we observed a loss of the membranes sealing function during the first spectrum acquisition or immediately after (Fig. 3). Since the electric field in DMEM medium and the 100 mS/m measurement solution of different osmolarity is similar, we assume that the

cell membrane degradation might depend on Joule heating caused by an increased ionic current due to higher conductivity of DMEM. Joule heating increases the temperature in the surrounding area of the cell, which might damage its membrane.

Table 1. A measurement solution with a reduced osmolarity stresses the cells and affects the viability. 0.1% Erythrosine B dye was added to detect viable cells. For each condition about 200 cells were observed in separate petri dishes.

Osmolarity [mOs/kg]	100	200	250	300 (DMEM)
Viability	60 %	77 %	87%	92 %

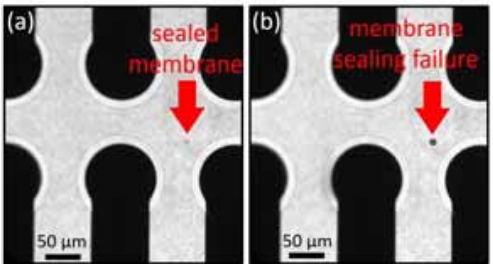

Figure 3: A HEK 293 cell in DMEM with 0.1% erythrosine B dye is not stained and therefore has a sealed membrane before the spectra acquisition (a) and is stained due to membrane sealing failure after the spectra acquisition (b).

CONCLUSION

In conclusion, several electrorotation experiments could be performed in order to demonstrate the stability and functionality of our parallel electrorotation platform. The effect of the osmolarity on the cell membrane could be observed in agreement with the literature. The effect of osmolarity on the cell viability was characterized outside the chip. Moreover, we could observe in real-time on our chips the loss of membranes sealing function by adding Erythrosin B dye in the measurement solution. Finally a shift in the electrorotation spectrum related to a change in the membrane capacitance could be observed corresponding to the appearance to of the cell intake of the viability masker.

ACKNOWLEDGEMENTS

This research was financed by the Swiss National Science Foundation (205321_179086). The microfluidic chips were fabricated at the Center for Nano- and Microtechnology at EPFL.

REFERENCES

[1] X. B. Wang, Y. Huang, P. R. C. Gascoyne, F. F. Becker, R. Hölzel, and R. Pethig, "Changes in Friend murine erythroleukaemia cell membranes during induced differentiation determined by electrorotation," *BBA - Biomembr.*, vol. 1193, no. 2, pp. 330–344, 1994.

[2] K. Keim, M. Z. Rashed, S. C. Kilchenmann, A. Delattre, A. F. Gonçalves, P. Éry, and C. Guiducci, "On-chip technology for single-cell arraying, electrorotation-based analysis and selective release," *Electrophoresis*, vol. 40, no. 14, pp. 1830–1838, Jun. 2019.

[3] S. C. Kilchenmann, E. Rollo, P. Maoddi, and C. Guiducci, "Metal-Coated SU-8 Structures for High-Density 3-D Microelectrode Arrays," *Journal of Microelectromechanical Systems*, vol. 25, no. 3, pp. 425–431, Jun-2016.

[4] K. Keim, P. Éry, A. Delattre, and C. Guiducci, "3D electrode arrays for trapping, analysis and selectrive release of single cells using DEP," in *Micro Total Analysis Systems*, 2018, pp. 2394–2397.

[5] P. R. C. Gascoyne, F. F. Becker, and X. B. Wang, "Numerical analysis of the influence of experimental conditions on the accuracy of dielectric parameters derived from electrorotation measurements," *Bioelectrochemistry Bioenerg.*, vol. 36, no. 2, pp. 115–125, 1995.

CONTACT

* Kevin Keim; phone +41-21-69-31335; kevin.keim@epfl.ch

Vol. 4 • No. 9 • September • 2019
www.advmattechnol.com

ADVANCED MATERIALS TECHNOLOGIES

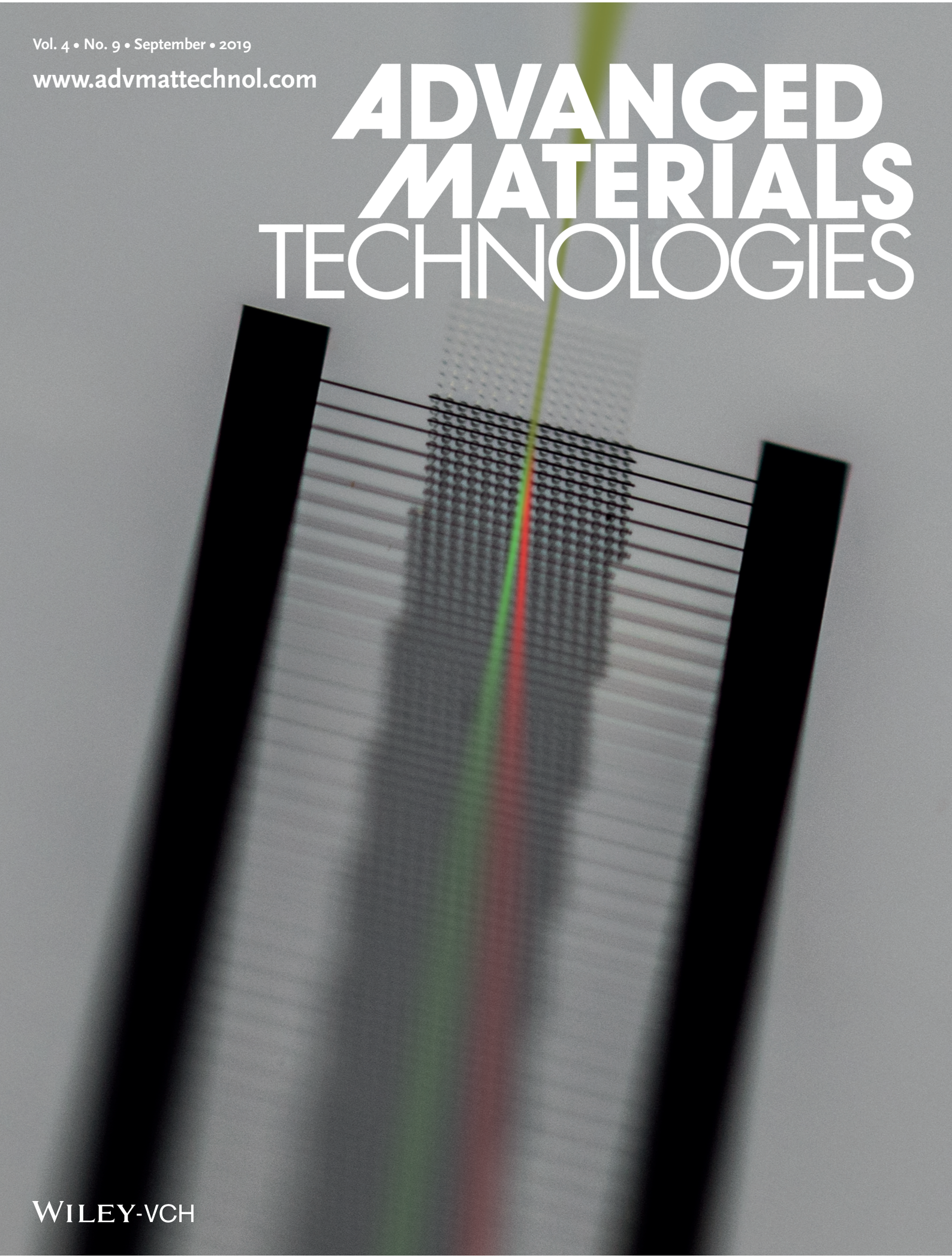

WILEY-VCH

Microfluidics: Active Posts in Deterministic Lateral Displacement Devices (Adv. Mater. Technol. 9/2019)

"A microfluidic sorting scheme based on deterministic lateral displacement in which the posts are active electrodes is presented by Jason P. Beech, Jonas O. Tegenfeldt, and co-workers, in article number 1900339. Changing the voltage applied to the posts allows for adjustment of the cut-off size in a range from $6\mu m$ to $0.25\mu m$. Although the device has features of tens of micrometers, this large dynamic range allows for the sorting of nanoscale particles." [157] reproduced with permission from John Wiley and Sons.

4 Sub micrometer particles sorting by combined electrokinetic and microfluidic methods

In this chapter a deterministic lateral displacement (DLD) device is presented, whose sorting size can be tuned by an additional dielectrophoretic force. The DLD posts are replaced by three dimensional electrodes, which allow to create local electric fields and change the sorting size by a local dielectrophoretic force.

First, the basic principles of deterministic lateral displacement are explained and fundamental equations from the research area, predicting the behavior of particles in the structures, are presented.

Second, the measurement setup and procedure for the deterministic lateral devices are presented and explained in more detail.

Last, the different electrode designs for the sorting devices are shown and explained, as well as the functionality is demonstrated by the presentation of the experimental results and the derivation of a predicting theoretical equation.

4.1 Theoretical background on deterministic lateral displacement

Deterministic lateral displacement is used to sort particles by size. It consists of a microfluidic channel in a laminar flow regime. The channel features a regular pattern of posts/restrictions. Each consecutive row is shifted by a set distance to the previous [43].

The particles in the fluid flow through the labyrinth and their center of mass follows the microfluidic stream lines. Due to their finite size and the periodic shift of the rows, the particles will bump into the posts.

First, due to their increased size, larger particles will bump into the posts earlier than smaller particles. Their radius is larger and therefore their center of mass, correspondingly the microfluidic flow line which they follow, can be further away from the post wall and they still get in contact.

Second, if differently-sized particles on a microfluidic flow line get in contact with a post, larger particles will experience an increased displacement compared to smaller particles, as shown in Fig. 4.1. Their center of mass will remain at least the particle radius away from the post wall. The wall force does not let the particle penetrate it and therefore the particle is displaced away from the microfluidic stream line.

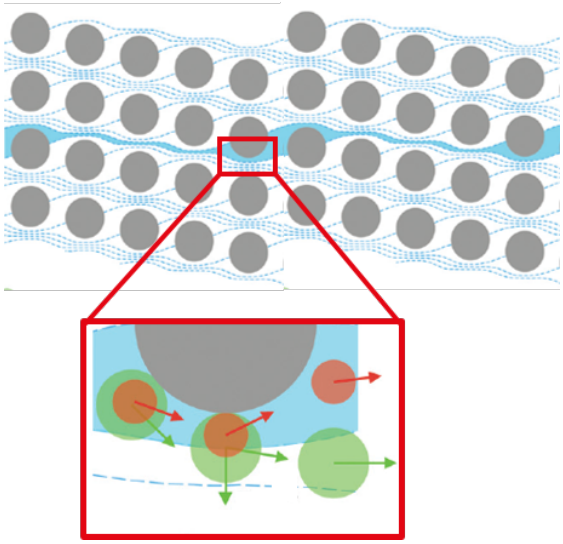

Figure 4.1 – Differently-sized particles are flown through a labyrinth featuring of microfluidic post. Due to there finite size and the shift of the rows, the particles are eventually colliding with the posts. Due to their radius, the center of mass of larger particles are further pushed away from the stream line than smaller particles. Figure adapted from [47] with permission from the Royal Society of Chemistry.

Correspondingly, smaller particles will continue following the microfluidic stream lines (so-called zigzag mode), while larger particles are getting displaced and follow the diagonal alignment of posts in the labyrinth (displacement mode), as shown in Fig. 4.2.

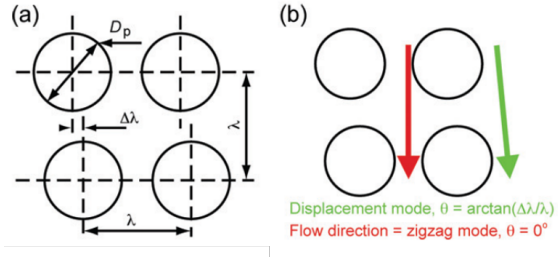

Figure 4.2 – (a)Definition of the parameters for the DLD devices. (b) Small particles will follow the flow direction and flow in the zigzag mode at an angle of 0° while larger particles in the displacement mode go along the alignment of the posts under an angle to the average microfluidic flow. Figure adapted from [47] with permission from the Royal Society of Chemistry.

The critical size at which larger particles are in the displacement mode and smaller particles

are in zigzag mode depends on the device parameters and is given by [47]

$$D_C = 2\alpha \frac{d}{N} \tag{4.1}$$

with

$$d = \lambda - D_p \tag{4.2}$$

and the periodicity is

$$N = \frac{\lambda}{\Delta\lambda} \tag{4.3}$$

with $\alpha = 2.5$ from the stretching method [45], λ the distance between the posts, $\Delta\lambda$ the shift distance from row to row and D_p the post diameter.

Particles larger than the critical size will flow in displacement mode through the posts labyrinth and end up against one of the border sidewall of the channel. On the other hand, particles smaller than the critical size will go straight through the device following the microfluidic stream lines in the zigzag mode and end at approximately the same channel section, where they entered.

This method allows to perform a continuous size-based sorting of bio-particles.

4.2 Experimental methods for deterministic lateral displacement

The experiments with the combined DLD and DEP devices using three dimensional electrodes are tested at the Tegenfeldt lab, at NanoLund of the Lund University, as well as at EPFL in the bioimaging and optics platfrom (BIOP) facility. The experimental setup and the used methods will be presented in the following. Some content of the following chapter is reproduced from [157] with the permission from John Wiley and Sons.

4.2.1 Deterministic lateral displacement setup

The microfluidic connection is provided by glued tubes of $5mm$ diameter on top of the three inlets, the middle one is dedicated respectively to inject the sample, and the two on the side for the buffer to focus the stream of the particles in the device. Another tube is glued at the outlet of the device, working as waste reservoir, as shown in Fig. 4.3(b). The outlet of the PDMS is kept at ambient pressure, while three inlets are supplied with pressure from a MFCS-4C pressure controller (Fluigent, Paris, France).

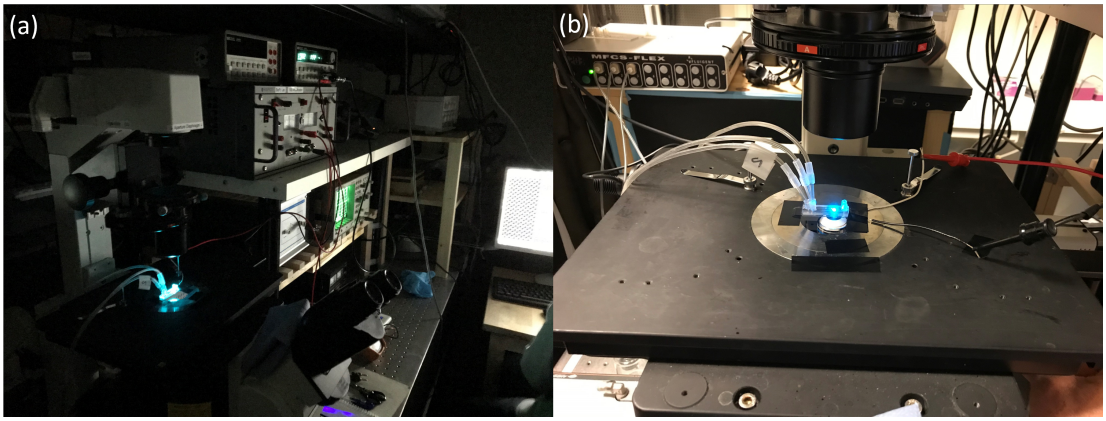

Figure 4.3 – (a) The DLD setup connected the microfluidic chip under an inverted microscope to a pressure system and a frequency generator which were controlled by a computer. (b) close look to the microfluidic chip under the microscope. The microfluidic connectors are glued to the device and the electronic contacts are soldered on.

The microfluidic chip for the active deterministic lateral displacement posts is inspected under an inverted microscope (Nikon Eclipse TE2000-U, Nikon Corporation, Tokyo, Japan) and camera (Andor Neo CMOS, Andor Technology, Belfast, Northern Ireland). A picture of the setup is shown in Fig. 4.3(a). The chip is placed under the microscope as shown in Fig. 4.3(b). Beforehand, the electronic connections, as shown in Fig. 4.3(b) and for the electrodes are soldered on the chip in order to provide the electronic signal, as shown in Fig. 4.4(B). No PCB is used in this setup. The signal is applied to the different rows of electrodes, as sketched in Fig. 4.4(A) and (C), using a function generator (15 MHz function/arbitrary waveform generator, model 33120A, Hewlett Packard, Palo Alto, CA, USA), which provides one of the signal lines with an AC signal and the other one with a reference ground signal. The applied voltage is monitored by an oscilloscope (Hewlett Packard 54603B 60 MHz) with a 1×/10× probe (Kenwood PC-54, 600 Vpp).

4.2.2 Deterministic lateral displacement measurement procedure

The buffer solution for the deterministic lateral displacement experiments is prepared by adding $1.7 \cdot 10^{-3}$ M KCl and 0.1% Pluronics F127 deionized water. The conductivity of the solution is measured to be $25 mS/m$. All reservoirs are filled with the buffer and the solution is driven through the device until the device is filled with liquid and no air bubbles remain. Then latex beads are suspended in the buffer and the pure buffer from the middle sample inlet is exchanged for the buffer solution containing beads. Over pressure in the range of $0.3 - 75 mBar$ is applied to the inlets. The beads are flowing through the device in a stream which we call *beam*. The beam through the device is adjusted by changing the pressure at the two buffer inlets so that the beads are going straight through the device, as shown in Fig 4.5(A). Subsequently an AC electric signal is applied to the electrodes. The beads eventually change their traveling mode through the device from zigzag (straight through the device) to

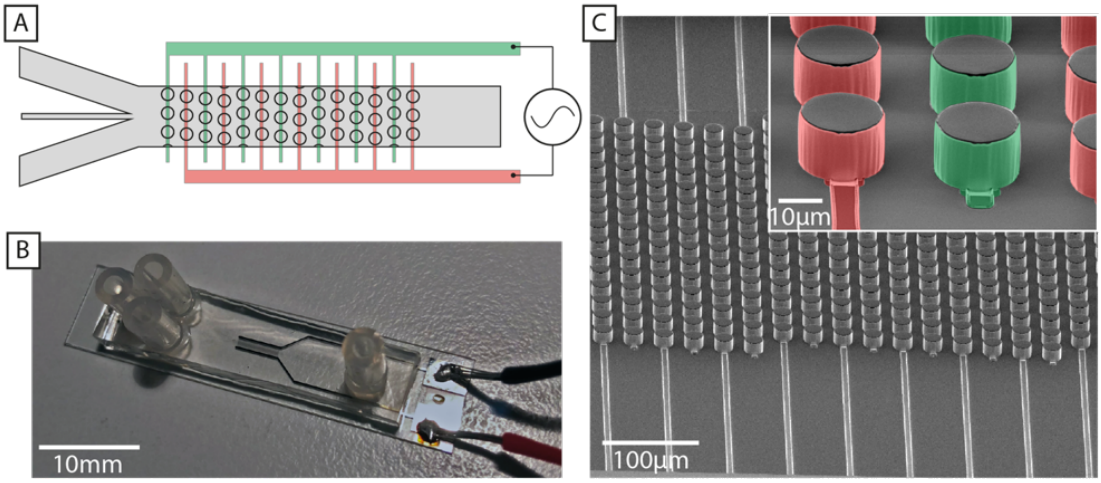

Figure 4.4 – The chips with the three-dimensional electrodes have three inlets and one outlet. Subsequent rows of electrodes are connected to the opposite signal of a sinusoidal $10MHz$ AC signal. (A) Sketch of the device layout. The sample is injected in the middle inlet on the left and driven over the device, where subsequent rows are connected to opposite AC signals. (B) Picture of the device directly before using it. Tubes as reservoirs are glued on the chip and cables are soldered on the exposed metal to apply the AC signal. (C) SEM micrograph of the three-dimensional electrodes, which are connected from both sides, with the different electric signal. The color indicated, which signal is applied. Figure reproduced from [157] with permission of John Wiley and Sons.

a displacement mode (traveling along the post direction) and end up at a different position, as shown in Fig 4.5(B). The different modes are illustrated in Fig. 4.5(C). The zigzag mode at the bottom appears, when the particles are smaller than the critical size of the device. The beads follow the microfluidic flow. The displacement mode, illustrated in the top, shows beads traveling along the direction of the displaced posts. It appears, when the critical size of the device is smaller than the particles. A mix mode, as illustrated in the middle, appears, when the critical size of the device is about the size of the beads. Still the particles are going in zigzag through the device, but the natural periodicity is enlarged. Our device has 14 outlets, as shown in Fig. 4.5(E). When the beads travel through the device in zigzag mode, they leave the device through channel 8. When they are in full displacement mode, they leave the device through outlet 14. Counting the beads going through each outlet, at a specific applied voltage, allows to plot the average outlet position versus the applied voltage, as shown in Fig. 4.5(D). For beads of a size below the critical size of the device with no field applied, the outlet position at $0V$ is outlet 8. Increasing the the applied voltage, eventually they get into a mixed mode and leave the device in average at outlet 10, until they are getting in full displacement mode and leave the device through outlet 14. These graphs for beads of different sizes are used to characterize the device.

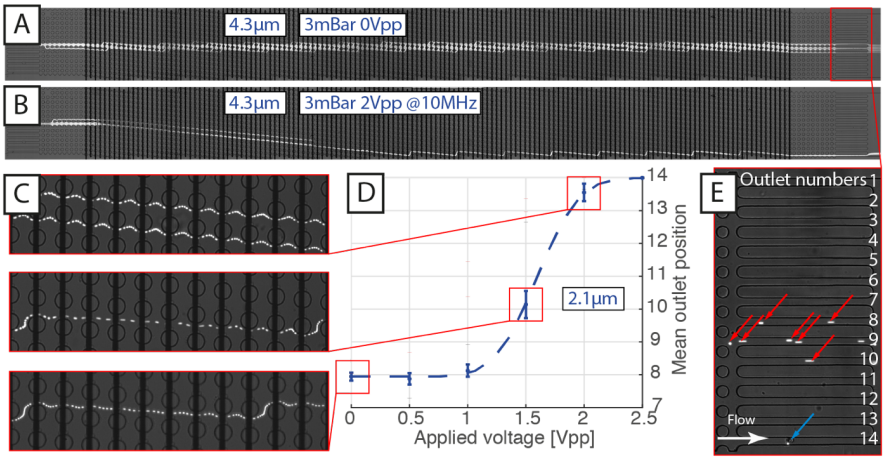

Figure 4.5 – Principle of investigation of the devices. (A) Beads below the critical size of the device are flown through the device in zigzag mode. They leave the device at outle number 7 and 8. (B) The same beads with an applied voltage. They displace and leave the device at outlet 14. (C) The different travelling modes of the beads through the device. Top: displacement mode. Middle: mixed mode with enlarged periodicity. Bottom: zigzag-mode. (D) The average outlet through which the beads leave the device depends on the travelling mode. In the zigzag mode the beads leave the device at outlet 8, in the mixed mode at outlet 10 and at the displacement mode at outlet 14. (E) The number of beads at each outlet are counted to evaluate the behavior of the beads at different conditions. Figure reproduced from [157] with permission of John Wiley and Sons. The microscope images where taken at NanoLund of devices produced at EPFL.

4.3 Three dimensional posts enable local dielectrophoretic forces in deterministic lateral displacement devices

In this section the experimental results are presented and discussed. Beads of different sizes are flown through the device at different pressure differences. Applying an electric field on the electrodes changes the trajectory of the beads and their outlet position is observed. Later for one bead size, the applied voltage is choose that way that the beads are in full displacement, subsequently the pressure and therefore the beads flow speed is increased. The beads are not in full displacement anymore. The applied voltage is increased in order to get them back in displacement mode. The corresponding pressure and applied voltage are recorded. From these acquired data an equation for the critical voltage for a specific device can be estimated, which is the applied voltage needed in order to have a specific critical size in a device of a defined geometry and pressure difference.

4.3.1 The critical size is changed by the applied voltage

Beads of a diameter of $200nm$, $500nm$, $1\mu m$ and $2\mu m$ are flown through the device at a pressure difference between the inlet and the outlet of $0.3mBar$. At no applied voltage, they

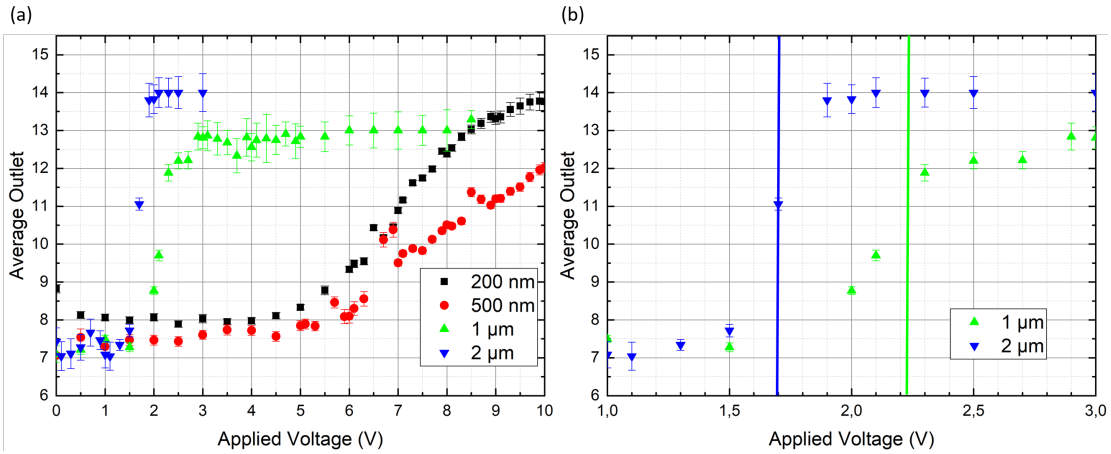

Figure 4.6 – The averaged outlet position of beads of different sizes is plotted versus the applied voltage. The applied pressure is $0.3mBar$. (a) Characteristic curves for $200nm$, $500nm$, $1\mu m$ and $2\mu m$ diameter beads. (b) Zoom for $1\mu m$ and $2\mu m$ diameter beads. The cross-over voltages of $1.7V$ and $2.2V$is indicated by a vertical line.

go straight through through the device and leave the device through outlet 7 or 8, as shown in Fig. 4.6 (a). Increasing the voltage some of the beads are getting into the a mixed mode. First, the $2\mu m$ at a voltage of $1.7V_{pp}$ are in a mixed mode and leave the device through outlet 11, as clearly visible in the zoom in 4.6 (b) and marked with a blue vertical line. At $1.9V_{pp}$ they are already in the displacement mode. Next, the the beads of a diameter of $1\mu m$ are getting in a mixed mode at a voltage of $2.2V_{pp}$. At $3V_{pp}$ they are in a full displacement mode, but leave the device through outlet 13, which can be explained by clogging of the fourteens outlet channel, which therefore makes outlet 13, the outlet of the displacement mode. Next, the beads of $500nm$ diameter should get into the mixed and subsequently the displacement mode, which is not the case, as seen in 4.6 (a). The smaller $200nm$ beads are getting into the mixed and the displacement mode at lower applied voltages. Additionally, one can see, that the transition of from full zigzag to full displacement is spread over a more applied voltages, which could potentially be explained by the increased diffusion of smaller particles. The lower crossover voltage of $200nm$ beads compared to $500nm$ beads could be explained by the usage of different devices. In order to minimize the contamination of the experiment by remaining beads of different sizes from a previous experiment, new chips are used for every bead size. However, every chip has imperfections due to the fabrication and the natural critical size due to the device geometry can slightly vary. This could explain, why the $200nm$ beads are getting into the displacement mode at lower voltages than the $500nm$ beads. As well the small offset in the outlet position at no applied voltage is an indicator of this imperfection and can be added for the explanation of a varying behavior. However, repeating the experiments several times with bare new chips, the outcome of the experiments showed much better repeatability, as demonstrated in [157] for eight different bead sizes.

4.3.2 The traveling mode depends on the applied voltage and the applied pressure

In order to find the relation between the traveling speed of the beads, which we control by the applied pressure, and the applied voltage in order to get the beads in full displacement mode, the applied pressure is set and the applied voltage is increased until all beads leave the device through channel 14. For this experiment, beads of $2\mu m$ diameter are used.

First, the pressure is increased so the beads are not in full displacement mode anymore. Subsequently the the applied voltage is mounted until the beads are leaving the device again through channel 14 and are in the full displacement mode. The corresponding pressure/voltage values are noted and the pressure is increased again.

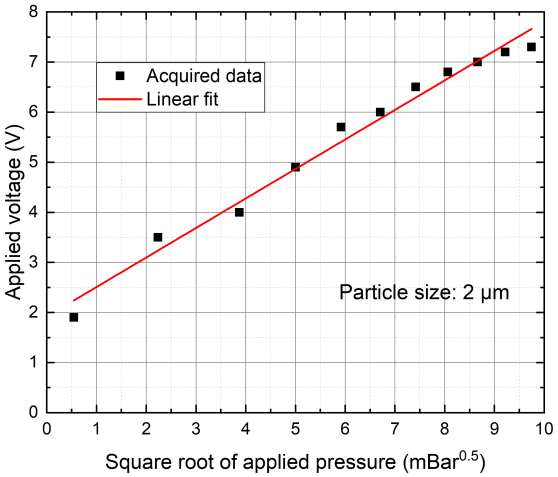

Figure 4.7 – The square root of the applied pressure versus the applied voltage is plotted, when reaching full displacement. The red line shows the linear fit with offset of $1.9V$, a slope of $0.6V/mbar^{0.5}$ and $R^2 = 0.98$.

Plotting the square rood of the applied pressure versus the applied voltage, as shown in Fig. 4.7, shows a linear relation, with an offset at the voltage axis of $1.9V$ and a slop of $0.6V/mbar$. The linear relation of the applied voltage/square root of applied pressure relation is reasonable, since the dielectrophoretic force scales with the square of the applied voltage, while the microfluidic drag force scales linear with the applied pressure, which we will explain in more detail. Since the size of the beads of $2\mu m$ is below the critical size of the device of $6\mu m$, the offset at the voltage axis of $1.9V$ makes sense, since even at very slow flow speeds a voltage has to be applied in order to push the beads into the displacement mode. The slope of $0.6V/mbar$ is a parameter which depends on the size of the beads and the device geometry, as well as on the conditions playing into the Clausius-Mossotti factor, such as electric frequency, medium conductivity, and material of the beads. Since we did this experimental with only with one bead size, no statement on this value should be done, however, comparing this value for different bead sizes, a statement on the slope could be done later on.

4.3.3 Equation for the crossover voltage

As already implied, the dielectrophoretic force and the microfluidic drag force for particles below the natural critical size of the device are in competition to define the trajectory of the beads through the device. As sketched in Fig. 4.8, the particle which is naturally in zigzag mode, wants to cross between the electrodes. An electric field of high field gradient is created between the two posts, leading to a negative dielectrophoretic force at the chosen conditions, pushing the particle away from the zigzag mode to the displacement mode. Whether a particle remains in the zigzag mode or changes to the displacement mode depends on the strength of the two mentioned forces, drag and dielectrophoretic.

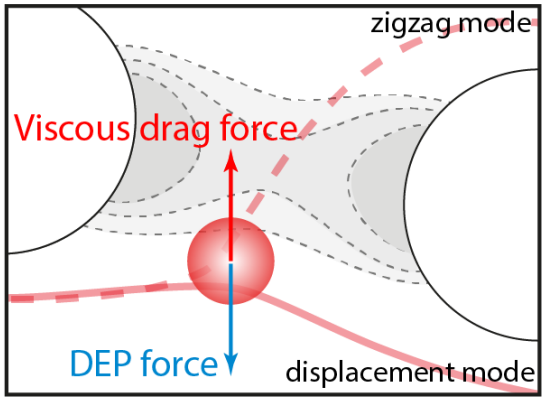

Figure 4.8 – For particles which are due to their size without electrical field applied in the zigzag mode, the viscous drag force is laterally competing with the DEP force. The critical voltage can be determined by comparing these two forces. Figure reproduced from [157] with permission of John Wiley and Sons.

The dielectrophoretic force is given by

$$\langle \mathbf{F}_{DEP} \rangle = \pi \epsilon_0 \epsilon_m R^3 Re[CM] \nabla E_{pk}^2 \tag{4.4}$$

and the drag force is given by

$$F_{drag} = 6\pi\eta R v \tag{4.5}$$

as explained in chapter 2.

At the critical speed v_{DEP}, created by the DEP force, these two forces in Eq. 4.4 and Eq. 4.5 are equal and therefore

$$v_{DEP} = \frac{\epsilon_m R^2 Re[CM] \nabla E_{pk}^2}{6\eta} \tag{4.6}$$

knowing that

$$\nabla E_{pk}^2 \propto \frac{1}{w}\frac{V^2}{w^2} \tag{4.7}$$

with V the applied voltage and w the distance between the posts we get

$$v_{DEP} \propto \frac{\epsilon_m R^2 Re[CM] V^2}{6\eta w^3} \tag{4.8}$$

A particle smaller then the critical size is usually in zigzag mode. It has to be displaced by

$$\Delta S = R_C - R \tag{4.9}$$

in order to get into the displacement mode (with R_C the critical size of the device). This distance is the time of the exposed DEP force times the critical DEP velocity from Eq. 4.6. The time is given from the inter post distance divided by the flowspeed v_{flow}

$$\Delta S = v_{DEP} \cdot t_{DEP} = v_{DEP}\frac{w}{v_{flow}} \tag{4.10}$$

Combining Eq. 4.9 and 4.10, one finds

$$R_C - R = v_{DEP}\frac{w}{v_{flow}} \tag{4.11}$$

and from the parabolic flow profile in the laminar flow regime we know

$$v_{flow} = \frac{\Delta p \cdot w^2}{24\eta L} \tag{4.12}$$

with the pressure difference Δp and the total length of the device L.

Combining Eq. 4.11 and 4.12, one finds for the critical speed

$$v_{DEP} = \frac{(R_C - R)\Delta p \cdot w^2}{24\eta L w} \tag{4.13}$$

Comparing Eq. 4.14 and 4.8 one finds for the critical voltage of the specific device

$$V^2 \propto \frac{R_c - R}{R^2} \cdot \Delta p \cdot \frac{1}{\epsilon_m Re[CM]} \cdot \frac{w^4}{L} \tag{4.14}$$

This is very well in agreement with the experimental data. We observed the linear relation between applied voltage and the square root of the applied pressure $V^2 \propto \Delta p$, as well as the increase in the critical voltage for smaller particles $V^2 \propto \frac{R_c - R}{R^2}$. Additional the fundamental variables of the dielectrophoretic force, the real part of the Clausius-Mossotti factor, as well as the fundamental parts of the microfluidic drag force, the device parameters, are reflected in the equation.

4.3.4 Sharp edged electrodes for sorting of smaller particles

Round electrodes are commonly used in DLD devices and were therefore the first choice for testing the devices. However, with the photolithographic precision, we can as well fabricate electrodes/posts in any other shape. Their form shapes both the electric field, as well as the microfluidic flow lines, which are initially followed by the particles with no field applied. One very promising shape is teardrop shaped electrodes, whose sharp tip points towards the inlet of the chip. We performed finite element simulations using COMSOL Multiphysics 5.3 ®, simulating the electric field as well as the microfluidic flow of the traditional round electrodes and the teardrop shaped electrodes. This results of the simulation are shown in Fig. 4.9.

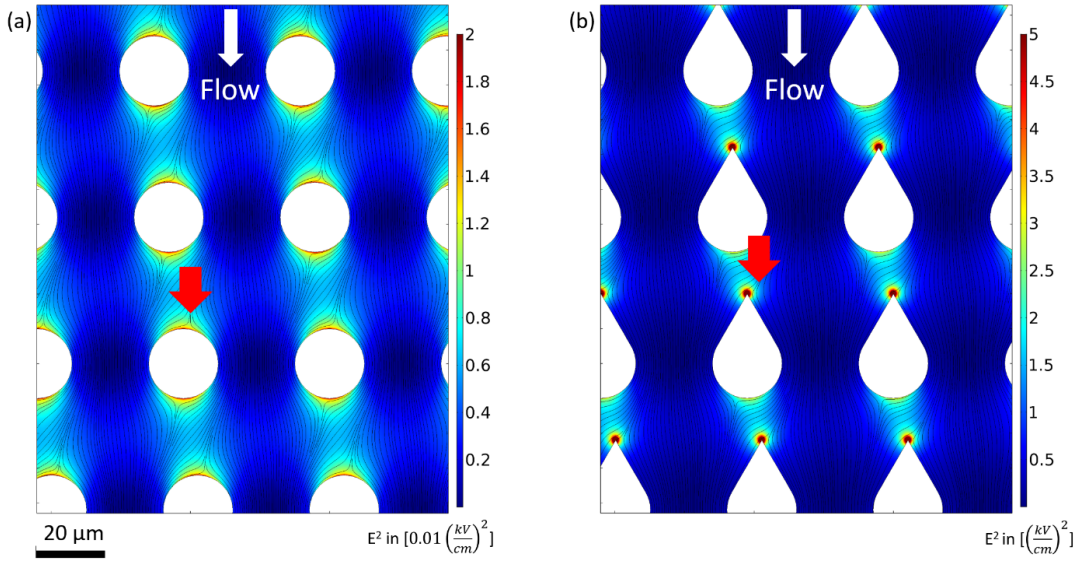

Figure 4.9 – Two-dimensional COMSOL models of the microfluidic stream lines (black lines) and the electric field square (colour code) for different electrode geometries. (a) round post shapes, which create more homogeneous and smaller electric fields. (b) teardrop shaped electrodes, with high gradient and high electric field squares. More importantly the electric field gradient is the highest, where the critical particles decide their trajectory, because of the separation of the microfluidic field lines. The red arrows point to the critical area.

The microfluidic flow is from the top to the bottom and the flow lines are shown in black. The square of the electric field between the different poled electrodes rows is illustrated by the color coding of the background. One has to mention, that the scale of the electric field square

is different in both graphs due to visibility reasons in both cases. First, the electric field is generally higher between the teardrop shaped electrodes, which is related to their increased length and therefore the reduced gap, leading to a higher electric field. However, as well the field gradient is significantly higher and very local, as seen by small read areas in Fig. 4.9(b). In Fig. 4.9(a) the strength of the electric field square is not changing as fast, and therefore the electric field gradient is smaller too.

Particles of exactly the critical size of the size follow one of the flow lines, which separate right before the microfluidic restriction. The decision for left (zigzag mode) or right (displacement mode) happens where the flow lines separate, as indicated by the red arrows. An advantage of the teardrop shaped electrodes is, that the electric field and the electric field gradient are exactly here the strongest, where the particle decides its trajectory. Therefore, a tipping into the displacement mode can be done with very little applied voltage, since the resulting dielectrophoretic force is strong.

Our hope is that with the electrode shape already tested particles can be displaced at smaller voltages and that even smaller particles then 200nm of diameter can be displaced by voltages up to 10V_{pp}.

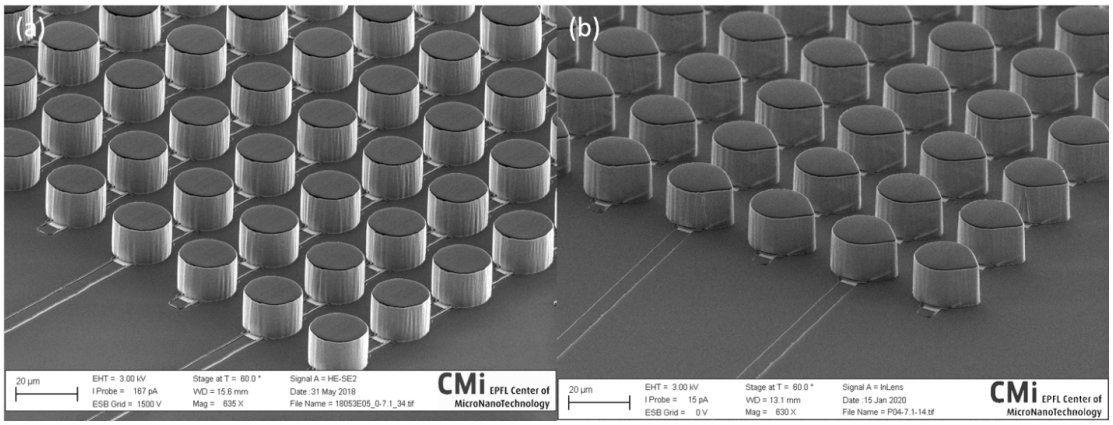

Figure 4.10 – SEM micrographs of different electrode shapes. (a) traditional round electrode shapes. (b) sharp edged teardrop shaped electrodes for smaller critical sizes.

The teardrop shape electrodes could already be fabricated as shown in Fig. 4.10(b). In the fabricated device, the tip of the teardrop does not look as sharp as in the simulations, still the sharp edge is clearly visible compared to the traditional round electrodes shown in Fig. 4.10(a), hopefully leading to an improved device performance.

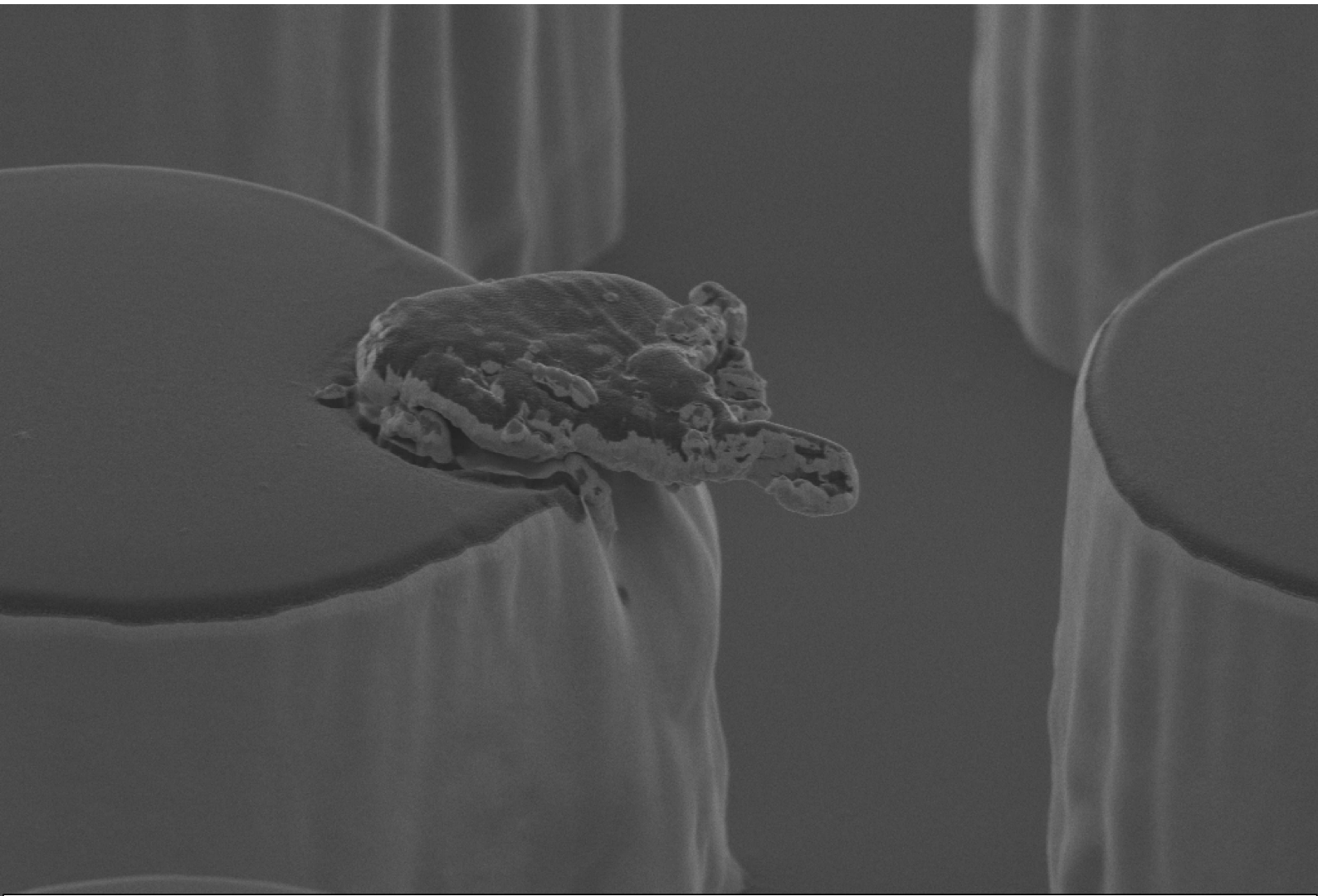
1 µm
EHT = 3.00 kV
I Probe = 15 pA
ESB Grid = 0 V
Stage at T = 60.0 °
WD = 13.1 mm
Mag = 3.97 K X
Signal A = InLens
Date :15 Jan 2020
File Name = P04-7.1-09.tif
CMi EPFL Center of MicroNanoTechnology

CMi Picture of the Month Run-up January 2020: Turtle diving into ocean

In January 2020 this titanium-platinum turtle is diving from the sharp edge of a new teardrop-shaped 3D electrode into the ocean, swimming to new shores. “Bye bye CMi. Thanks for the great time. I will send you a postcard.”
Kevin Keim, Gloria Porro

5 Summary, Conclusion and Outlook

In what follows, the results of this thesis are summarized and some conclusions are drawn. Future possible work is discussed in the outlook.

5.1 Summary

This thesis reports two implementations of three dimensional electrodes in dielectrophoretic devices. Both systems show their functionality and are used either to build a novel design, outperforming previous solutions thanks to the use of this new technology. In the case of the DLD-DEP device, our contribution enabled to replace existing insulating structures with three dimensional electrodes giving new functionalities to an existing design.

First, an arrayed electrorotation device is designed based on finite element simulations of the microfluidic and electrokinetic forces. A design and the corresponding conditions are found, which enables to trap different cell lines in arrayed dielectrophoretic micro-cages. This design is realized and tested. An array of 39 dielectrophoretic traps made out of two rows of three dimensional electrodes spanning a wide microfluidic channel is created. Controlling the applied signals on each of the electrodes by a homemade PCB allows to selectively trap and release individual cells. The alternation between the nDEP trapping and the electrorotation signal, enables to keep single cells centered in the middle of the trap against flow while blocking additional cells from entering the same trap. In the current state, this system allows to analyze 10 cells at a time, since those can be visualized in the same field of view in parallel. HEK293, T lymphocytes, M17 neuroblastoma and HeLa cells could be distinguished based on their electrorotation spectra and their membrane capacitance could be found by fitting the single shell model to the data. The values of HEK293 cells, T lymphocytes and HeLa cells are in agreement with the literature, while the membrane value of M17 neuroblastoma of $7.49 \pm 0.39 mF/m^2$ is reported in our paper for the first time. The viability of the cells is investigated in real-time by adding an erythrosin B dye to the measurement solution. Cells survive over 30 min of continuous measurements. If cells are found to die during the measurements, the cell death is also visible in a shift in the electrorotation spectrum and a

drop in the extracted membrane capacitance. Membrane changes within one cell population are investigated by an osmolarity study and differences in the membrane capacitance in the same population of cells due to different osmolarities could be resolved. Overall, the system is fully functional and can be employed for further biological applications.

Second, PDMS pillars in deterministic lateral displacement devices can be replaced by three dimensional electrodes. Applying an alternating electric field at the electrodes adds a local dielectrophoretic force, which changes the critical size of the originally deterministic device. The critical size can actually be tuned by the applied voltage to the electrodes. The device can continuously separate particles from $6\mu m$ to $250nm$. This means that the critical size in the exact same DLD device could be reduced by a factor of 24. The devices are extremely robust and withstand $100V_{pp}$. Finite element simulations confirm the results from a theoretical perspective and a relation for the cross-over voltage of the device can be found as a function of the particle size, the critical size of the device, the Clausius-Mossotti factor of the particle and the applied pressure. The devices are fully functional with beads and first experiments were performed using bio samples. The devices are ready to be investigated for biological applications.

Overall, the implementation of three dimensional electrodes in dielectrophoretic devices is shown and the functionality of the devices is proven, opening the door for further investigations of these devices or to create new dielectrophoretic designs using three dimensional electrodes.

5.2 Conclusion

Two different devices using three dimensional electrodes for dielectrophoretic applications have been demonstrated in this thesis. This shows that the three dimensional electrodes are well suited and reliable for these applications.

The parallel electrorotation devices shows that the electrodes can be used for arrayed analysis of the membrane properties of individually trapped single cells. This allows to think of further layouts, which can array even more cells and make electrorotation a technology which can analyze a large number of cells. It probably will not become a high throughput technology but hundreds of cells can realistically be analyzed in parallel with such systems.

This work shows as well that new devices with completely new layouts can be designed based on this technology. We demonstrated that the fabrication portfolio of researchers can be extended by this technology.

The usage of the three dimensional electrodes in the deterministic lateral displacement devices shows that passive structures in microfluidic devices can be replaced by the electrodes. This enables to reduce the sorting size of the devices and to tune it according to the needs, which allows to sort nano-sized particles in micro scale structures preventing the clogging and

improving the throughput. This shows, that existing devices can be improved by replacing their passive structures by three dimensional electrodes and this can improve the device performance. Additionally it can make these devices hybrid. In fact, combining microfluidic sorting and dieletrophoretic sorting could expand the particles properties used for sorting, for instance, shape, dielectric properties and morphology.

In conclusion, one can state that the presented three dimensional electrodes can be used to create new devices as well as to be implemented in existing devices to improve them. Even if the three dimensional electrodes are built by a multi mask process, which makes them expensive or time consuming to produce, they should be added to the researchers toolkit of fabrication processes for specialized applications.

5.3 Outlook

Based on the results of this thesis further possible projects are foreseen. Two of them are a further investigation and development of the two presented system. Another one is the use of the three dimensional electrodes in a different application. The next steps in there future endeavors will be explained in the following section.

5.3.1 Using parallelized electrorotation to investigate protein deposition in Alzheimer's disease

Alzheimer's disease is of major concern to the Western societies due to progressive age of their population [158]. Currently, there is a lack of effective diagnostic tools and therapies to prevent or slow the progress of the disease [159]. The aggregation state on neurons of two proteins amyloid beta (Aβ) and Tau [160] seems to have a major role in the primary process of the pathological lesions in the brain. The system could be used to assess the toxicity on a single neuronal cell level with a dielectric readout. The contribution of soluble Aβ and Tau oligomeric intermediates on the pathway to amyloid formation might bet investigated in comparison to mature fibrils and monomeric forms of the protein. As a first step, these proteins could be incubated with primary neurons or cultures of neuroblastoma, for example M17 cells, which are a common model for neurodegeneration studies, in order to see how they deposit on the cell membrane in different conditions. The dielectric parameters of the membrane, especially the membrane capacitance can be read out by the system. Furthermore, the process of fibril growth in modulating the neurotoxicity of the proteins could be investigated by applying conditions where the fibrils elongation is enhanced or blocked by adding excess of monomeric proteins or known inhibitors of fibril growth.

Another possibility to use the platfrom comes from its ability to access the membrane properties in real-time and the possiblity to exchange the surrouding medium. Cells, especially those living in suspension, could be kept in the dielectrophoretic traps over time and supplied with different reagents. Monitoring of the cells state based on an optical read-out, as well as based

on the dielectric properties of the cells would be possible. The exchange of different media with different reagents could be probed and give insights on their influences on the cell state.

5.3.2 Active DLD posts to separate exosoms based on their dielectric properties

In the next steps, the behavior of bio particles inside the devices shall be investigated. There is a major interest of the community to separate exosoms from different cells in order to further investigate the genomic information by liquid biopsy. First, exosoms could potentially be separated in the device based on their size. Conditions where the Clausius-Mossotti factor of the exosoms are similar need to be found, which is assumed to be simple for exosoms from the same cell, since they might be composed out of the same material. Correspondingly exosoms of the same size, but from different parental cells might be separated in the devices. This might be possible if their parental cells are different and therefore have different dielectric properties, which are possibly reflected in the exosoms they extrude. This might overcome competing technologies to separate exosoms at the moment, since they sort the populations mainly based on size.

Other interesting bio particle to investigate inside the device are bacteria. Changing the connection of the electrodes from rows of the same electric signal to columns of the same signal could enable two possible new effects. First, particles could be tipped from the zigzag to the displacement mode by positive dielectrophoresis, since the DEP force might pull the particles from the zigzag mode to the displacement mode. Second, due to the oval shape of bacteria they could be aligned in the electric field. Bacteria are growing lengthily during their life cycle, therefore they are getting longer but not wider. With no electric field applied, bacteria would flow stream lined through the device, reducing their fluidic resistance. The effective size within one population is about the same. However, aligning them in a way that they progress with their wide side in the direction of the microfluidic stream, they would have a different effective size and thus could be sorted depending on their life cycle.

The dimensions of the device could further be decreased in order to enable the sorting of even smaller particles or sorting of same-sized particles with even smaller applied voltages.

5.3.3 Trapping cells in flow to ensure encapsulation of multiple cells in droplets

As discussed before, the electrodes can be used in new devices, enabling functionalities, which were not available before. The electrorotation system was able to trap cells against flow. Selective trapping and selective release of individual cells is possible. In fact, keeping the trap open the accumulation in the trap of more than one cell would occur. One possible application of this configuration is to use the selective trapping behavior in order to accumulate cells upstream to droplet systems. A current challenge for the creation of microfluidic droplets is to create droplets with a specific number of cells or micro beads. The DEP trap, with the possibility to accumulate a certain number of cells in one trap and to selectively release, can

be used to collect a certain number of cells and release them together. This could allow to encapsulate them in one single droplet downstream.

Bibliography

[1] A. Manz, N. Graber, and H. Widmer, "Miniaturized total chemical analysis systems: A novel concept for chemical sensing," *Sensors and Actuators B: Chemical*, vol. 1, pp. 244–248, jan 1990.

[2] B. A. Kidd, G. Hoffman, N. Zimmerman, L. Li, J. W. Morgan, P. K. Glowe, G. J. Botwin, S. Parekh, N. Babic, M. W. Doust, G. B. Stock, E. E. Schadt, and J. T. Dudley, "Evaluation of direct-to-consumer low-volume lab tests in healthy adults," *Journal of Clinical Investigation*, vol. 126, no. 5, pp. 1734–1744, 2016.

[3] J. Carreyrou, *Bad Blood Secrets and Lies in a Silicon Valley Startup.* New York, NY: Alfred A. Knopf, 2018.

[4] S. C. Kilchenmann, E. Rollo, P. Maoddi, and C. Guiducci, "Metal-Coated SU-8 Structures for High-Density 3-D Microelectrode Arrays," *Journal of Microelectromechanical Systems*, vol. 25, pp. 425–431, jun 2016.

[5] J. V. Sweedler and E. A. Arriaga, "Single cell analysis," *Analytical and Bioanalytical Chemistry*, vol. 387, no. 1, pp. 1–2, 2007.

[6] L. Armbrecht and P. S. Dittrich, "Recent Advances in the Analysis of Single Cells," *Analytical Chemistry*, vol. 89, pp. 2–21, jan 2017.

[7] C. Wyatt Shields Iv, C. D. Reyes, and G. P. López, "Microfluidic cell sorting: A review of the advances in the separation of cells from debulking to rare cell isolation," *Lab on a Chip*, vol. 15, no. 5, pp. 1230–1249, 2015.

[8] L. A. Herzenberg, D. Parks, B. Sahaf, O. Perez, M. Roederer, and L. A. Herzenberg, "The history and future of the Fluorescence Activated Cell Sorter and flow cytometry: A view from Stanford," *Clinical Chemistry*, vol. 48, no. 10, pp. 1819–1827, 2002.

[9] S. Miltenyi, W. Müller, W. Weichel, and A. Radbruch, "High gradient magnetic cell separation with MACS," *Cytometry*, vol. 11, no. 2, pp. 231–238, 1990.

[10] T. R. Carey, K. L. Cotner, B. Li, and L. L. Sohn, "Developments in label-free microfluidic methods for single-cell analysis and sorting," *Wiley Interdisciplinary Reviews: Nanomedicine and Nanobiotechnology*, vol. 11, p. e1529, jan 2019.

[11] D. Di Carlo, D. Irimia, R. G. Tompkins, and M. Toner, "Continuous inertial focusing, ordering, and separation of particles in microchannels," *Proceedings of the National Academy of Sciences of the United States of America*, vol. 104, no. 48, pp. 18892–18897, 2007.

[12] S. S. Kuntaegowdanahalli, A. A. S. Bhagat, G. Kumar, and I. Papautsky, "Inertial microfluidics for continuous particle separation in spiral microchannels," *Lab on a Chip*, vol. 9, no. 20, p. 2973, 2009.

[13] J. Che, V. Yu, M. Dhar, C. Renier, M. Matsumoto, K. Heirich, E. B. Garon, J. Goldman, J. Rao, G. W. Sledge, M. D. Pegram, S. Sheth, S. S. Jeffrey, R. P. Kulkarni, E. Sollier, and D. Di Carlo, "Classification of large circulating tumor cells isolated with ultra-high throughput microfluidic Vortex technology," *Oncotarget*, vol. 7, no. 11, pp. 12748–12760, 2016.

[14] C. Renier, E. Pao, J. Che, H. E. Liu, C. A. Lemaire, M. Matsumoto, M. Triboulet, S. Srivinas, S. S. Jeffrey, M. Rettig, R. P. Kulkarni, D. Di Carlo, and E. Sollier-Christen, "Label-free isolation of prostate circulating tumor cells using Vortex microfluidic technology," *npj Precision Oncology*, vol. 1, no. 1, pp. 1–10, 2017.

[15] L. R. Huang, E. C. Cox, R. H. Austin, and J. C. Sturm, "Continuous Particle Separation Through Deterministic Lateral Displacement," *Science*, vol. 304, no. 5673, pp. 987–990, 2004.

[16] J. P. Beech, S. H. Holm, K. Adolfsson, and J. O. Tegenfeldt, "Sorting cells by size, shape and deformability," *Lab on a Chip*, vol. 12, no. 6, pp. 1048–1051, 2012.

[17] N. M. Karabacak, P. S. Spuhler, F. Fachin, E. J. Lim, V. Pai, E. Ozkumur, J. M. Martel, N. Kojic, K. Smith, P.-i. Chen, J. Yang, H. Hwang, B. Morgan, J. Trautwein, T. A. Barber, S. L. Stott, S. Maheswaran, R. Kapur, D. A. Haber, and M. Toner, "Microfluidic, marker-free isolation of circulating tumor cells from blood samples," *Nature Protocols*, vol. 9, pp. 694–710, mar 2014.

[18] J. Giddings, F. Yang, and M. Myers, "Flow-field-flow fractionation: a versatile new separation method," *Science*, vol. 193, pp. 1244–1245, sep 1976.

[19] H. Zhang and D. Lyden, "Asymmetric-flow field-flow fractionation technology for exomere and small extracellular vesicle separation and characterization," *Nature Protocols*, vol. 14, pp. 1027–1053, apr 2019.

[20] H. Jung, M. S. Chun, and M. S. Chang, "Sorting of human mesenchymal stem cells by applying optimally designed microfluidic chip filtration," *Analyst*, vol. 140, no. 4, pp. 1265–1274, 2015.

[21] J. Shi, H. Huang, Z. Stratton, Y. Huang, and T. J. Huang, "Continuous particle separation in a microfluidic channel via standing surface acoustic waves (SSAW)," *Lab on a Chip*, vol. 9, no. 23, pp. 3354–3359, 2009.

[22] J. Nam, H. Lim, D. Kim, and S. Shin, "Separation of platelets from whole blood using standing surface acoustic waves in a microchannel," *Lab on a Chip*, vol. 11, no. 19, pp. 3361–3364, 2011.

[23] Y. Huang, X. B. Wang, F. F. Becker, and P. R. Gascoyne, "Introducing dielectrophoresis as a new force field for field-flow fractionation," *Biophysical Journal*, vol. 73, no. 2, pp. 1118–1129, 1997.

[24] J. Giddings, "Field-flow fractionation: analysis of macromolecular, colloidal, and particulate materials," *Science*, vol. 260, pp. 1456–1465, jun 1993.

[25] D. R. Gossett, H. T. K. Tse, S. A. Lee, Y. Ying, A. G. Lindgren, O. O. Yang, J. Rao, A. T. Clark, and D. Di Carlo, "Hydrodynamic stretching of single cells for large population mechanical phenotyping," *Proceedings of the National Academy of Sciences*, vol. 109, pp. 7630–7635, may 2012.

[26] J. Guck, S. Schinkinger, B. Lincoln, F. Wottawah, S. Ebert, M. Romeyke, D. Lenz, H. M. Erickson, R. Ananthakrishnan, D. Mitchell, J. Kas, S. Ulvick, and C. Bilby, "Optical deformability as an inherent cell marker for testing malignant transformation and metastatic competence," *Biophysical Journal*, vol. 88, no. 5, pp. 3689–3698, 2005.

[27] B. Lincoln, H. M. Erickson, S. Schinkinger, F. Wottawah, D. Mitchell, S. Ulvick, C. Bilby, and J. Guck, "Deformability-based flow cytometry," *Cytometry*, vol. 59A, no. 2, pp. 203–209, 2004.

[28] A. Mietke, O. Otto, S. Girardo, P. Rosendahl, A. Taubenberger, S. Golfier, E. Ulbricht, S. Aland, J. Guck, and E. Fischer-Friedrich, "Extracting Cell Stiffness from Real-Time Deformability Cytometry: Theory and Experiment," *Biophysical Journal*, vol. 109, no. 10, pp. 2023–2036, 2015.

[29] O. Otto, P. Rosendahl, A. Mietke, S. Golfier, C. Herold, D. Klaue, S. Girardo, S. Pagliara, A. Ekpenyong, A. Jacobi, M. Wobus, N. Töpfner, U. F. Keyser, J. Mansfeld, E. Fischer-Friedrich, and J. Guck, "Real-time deformability cytometry: On-the-fly cell mechanical phenotyping," *Nature Methods*, vol. 12, no. 3, pp. 199–202, 2015.

[30] M. Xavier, P. Rosendahl, M. Herbig, M. Kräter, D. Spencer, M. Bornhäuser, R. O. Oreffo, H. Morgan, J. Guck, and O. Otto, "Mechanical phenotyping of primary human skeletal stem cells in heterogeneous populations by real-time deformability cytometry," *Integrative Biology (United Kingdom)*, vol. 8, no. 5, pp. 616–623, 2016.

[31] W. B. Varhue, L. Langman, M. Kelly-Goss, M. Lataillade, K. L. Brayman, S. Peirce-Cottler, and N. S. Swami, "Deformability-based microfluidic separation of pancreatic islets from exocrine acinar tissue for transplant applications," *Lab on a Chip*, vol. 17, no. 21, pp. 3682–3691, 2017.

[32] S. Gawad, K. Cheung, U. Seger, A. Bertsch, and P. Renaud, "Dielectric spectroscopy in a micromachined flow cytometer: Theoretical and practical considerations," *Lab on a Chip*, vol. 4, no. 3, pp. 241–251, 2004.

[33] D. Holmes, D. Pettigrew, C. H. Reccius, J. D. Gwyer, C. Van Berkel, J. Holloway, D. E. Davies, and H. Morgan, "Leukocyte analysis and differentiation using high speed microfluidic single cell impedance cytometry," *Lab on a Chip*, vol. 9, no. 20, pp. 2881–2889, 2009.

[34] E. Rollo, E. Tenaglia, R. Genolet, E. Bianchi, A. Harari, G. Coukos, and C. Guiducci, "Label-free identification of activated T lymphocytes through tridimensional microsensors on chip," *Biosensors and Bioelectronics*, vol. 94, pp. 193–199, aug 2017.

[35] T. Sun and H. Morgan, "Single-cell microfluidic Impedance cytometry: A review," *Microfluidics and Nanofluidics*, vol. 8, no. 4, pp. 423–443, 2010.

[36] J. S. McGrath, C. Honrado, J. H. Moore, S. J. Adair, W. B. Varhue, A. Salahi, V. Farmehini, B. J. Goudreau, S. Nagdas, E. M. Blais, T. W. Bauer, and N. S. Swami, "Electrophysiology-based stratification of pancreatic tumorigenicity by label-free single-cell impedance cytometry," *Analytica Chimica Acta*, vol. 1101, pp. 90–98, 2020.

[37] G. H. Markx, M. S. Talary, and R. Pethig, "Separation of viable and non-viable yeast using dielectrophoresis," *Journal of Biotechnology*, vol. 32, pp. 29–37, jan 1994.

[38] B. H. Lapizco-Encinas, B. A. Simmons, E. B. Cummings, and Y. Fintschenko, "Dielectrophoretic Concentration and Separation of Live and Dead Bacteria in an Array of Insulators," *Analytical Chemistry*, vol. 76, no. 6, pp. 1571–1579, 2004.

[39] H. Li and R. Bashir, "Dielectrophoretic separation and manipulation of live and heat-treated cells of Listeria on microfabricated devices with interdigitated electrodes," *Sensors and Actuators, B: Chemical*, vol. 86, no. 2-3, pp. 215–221, 2002.

[40] G. H. Markx, Y. Huang, X. F. Zhou, and R. Pethig, "Dielectrophoretic characterization and separation of micro-organisms," *Microbiology*, vol. 140, pp. 585–591, mar 1994.

[41] A. Rohani, J. H. Moore, J. A. Kashatus, H. Sesaki, D. F. Kashatus, and N. S. Swami, "Label-Free Quantification of Intracellular Mitochondrial Dynamics Using Dielectrophoresis," *Analytical Chemistry*, vol. 89, no. 11, pp. 5757–5764, 2017.

[42] K. R. Balakrishnan, J. C. Whang, R. Hwang, J. H. Hack, L. A. Godley, and L. L. Sohn, "Nodepore sensing enables label-free surface-marker profiling of single cells," *Analytical Chemistry*, vol. 87, no. 5, pp. 2988–2995, 2015.

[43] J. McGrath, M. Jimenez, and H. Bridle, "Deterministic lateral displacement for particle separation: a review," *Lab Chip*, vol. 14, no. 21, pp. 4139–4158, 2014.

[44] B. H. Wunsch, J. T. Smith, S. M. Gifford, C. Wang, M. Brink, R. L. Bruce, R. H. Austin, G. Stolovitzky, and Y. Astier, "Nanoscale lateral displacement arrays for the separation of exosomes and colloids down to 20nm," *Nature Nanotechnology*, vol. 11, no. 11, pp. 936–940, 2016.

[45] J. P. Beech and J. O. Tegenfeldt, "Tuneable separation in elastomeric microfluidics devices," *Lab on a Chip*, vol. 8, no. 5, pp. 657–659, 2008.

[46] S. Chang and Y.-H. Cho, "A continuous size-dependent particle separator using a negative dielectrophoretic virtual pillar array," *Lab on a Chip*, vol. 8, no. 11, p. 1930, 2008.

[47] J. P. Beech, P. Jönsson, and J. O. Tegenfeldt, "Tipping the balance of deterministic lateral displacement devices using dielectrophoresis," *Lab on a Chip*, vol. 9, no. 18, p. 2698, 2009.

[48] R. Devendra and G. Drazer, "Gravity Driven Deterministic Lateral Displacement for Particle Separation in Microfluidic Devices," *Analytical Chemistry*, vol. 84, pp. 10621–10627, dec 2012.

[49] Siyang Zheng, Raylene Yung, Yu-Chong Tai, and H. Kasdan, "Determinstic lateral displacement mems device for continuous blood cell separation," in *18th IEEE International Conference on Micro Electro Mechanical Systems, 2005. MEMS 2005.*, pp. 851–854, IEEE, 2005.

[50] V. Calero, P. Garcia-Sanchez, C. Honrado, A. Ramos, and H. Morgan, "AC electrokinetic biased deterministic lateral displacement for tunable particle separation," *Lab on a Chip*, vol. 19, no. 8, pp. 1386–1396, 2019.

[51] D. D. Carlo and L. P. Lee, "Dynamic Single-Cell Analysis for Quantitative Biology," *Analytical Chemistry*, vol. 78, pp. 7918–7925, dec 2006.

[52] S. Yilmaz and A. K. Singh, "Single cell genome sequencing," *Current Opinion in Biotechnology*, vol. 23, pp. 437–443, jun 2012.

[53] S. Lindström and H. Andersson-Svahn, "Overview of single-cell analyses: microdevices and applications," *Lab on a Chip*, vol. 10, no. 207890, pp. 3663–3672, 2010.

[54] S. Lindström and H. Andersson-Svahn, "Miniaturization of biological assays - Overview on microwell devices for single-cell analyses," *Biochimica et Biophysica Acta - General Subjects*, vol. 1810, no. 3, pp. 308–316, 2011.

[55] E. Ostuni, C. S. Chen, D. E. Ingber, and G. M. Whitesides, "Selective deposition of proteins and cells in arrays of microwells," *Langmuir*, vol. 17, no. 9, pp. 2828–2834, 2001.

[56] D. R. Walt, "Imaging optical sensor arrays," *Current Opinion in Chemical Biology*, vol. 6, no. 5, pp. 689–695, 2002.

[57] H. Yamamoto, K. Okano, T. Demura, Y. Hosokawa, H. Masuhara, T. Tanii, and S. Nakamura, "In-situ guidance of individual neuronal processes by wet femtosecond-laser processing of self-assembled monolayers," *Applied Physics Letters*, vol. 99, no. 16, pp. 16–19, 2011.

[58] H. Kaji, K. Tsukidate, T. Matsue, and M. Nishizawa, "In Situ Control of Cellular Growth and Migration on Substrates Using Microelectrodes," *Journal of the American Chemical Society*, vol. 126, pp. 15026–15027, nov 2004.

[59] C. S. Chen, M. Mrksich, S. Huang, G. M. Whitesides, and D. E. Ingber, "Geometric control of cell life and death.," *Science*, vol. 276, no. 5317, pp. 1425–8, 1997.

[60] R. S. Ashton, J. Peltier, C. A. Fasano, A. O'Neill, J. Leonard, S. Temple, D. V. Schaffer, and R. S. Kane, "High-Throughput Screening of Gene Function in Stem Cells Using Clonal Microarrays," *Stem Cells*, vol. 25, no. 11, pp. 2928–2935, 2007.

[61] D. G. Grier, "A revolution in optical manipulation," *Nature*, vol. 424, no. 6950, pp. 810–816, 2003.

[62] A. Valero, F. Merino, F. Wolbers, R. Luttge, I. Vermes, H. Andersson, and A. van den Berg, "Apoptotic cell death dynamics of HL60 cells studied using a microfluidic cell trap device.," *Lab on a chip*, vol. 5, no. 1, pp. 49–55, 2005.

[63] a. D. Goater and R. Pethig, "Electrorotation and dielectrophoresis.," *Parasitology*, vol. 117 Suppl, pp. S177–S189, 1998.

[64] J. Lu, C. A. Barrios, A. R. Dickson, J. L. Nourse, A. P. Lee, and L. A. Flanagan, "Advancing practical usage of microtechnology: a study of the functional consequences of dielectrophoresis on neural stem cells," *Integrative Biology*, vol. 4, no. 10, p. 1223, 2012.

[65] M. A. Unger, M. A. Unger, H.-p. Chou, T. Thorsen, A. Scherer, and S. R. Quake, "Monolithic Microfabricated Valves and Pumps by Multilayer Soft Lithography," *Science (New York, N.Y.)*, vol. 113, no. 2000, pp. 113–116, 2013.

[66] S. Köster, F. E. Angilè, H. Duan, J. J. Agresti, A. Wintner, C. Schmitz, A. C. Rowat, C. a. Merten, D. Pisignano, A. D. Griffiths, and D. a. Weitz, "Drop-based microfluidic devices for encapsulation of single cells.," *Lab on a chip*, vol. 8, no. 7, pp. 1110–1115, 2008.

[67] H. N. Joensson and H. Andersson Svahn, "Droplet microfluidics-A tool for single-cell analysis," *Angewandte Chemie - International Edition*, vol. 51, no. 49, pp. 12176–12192, 2012.

[68] B. M. Taff and J. Voldman, "A Scalable Addressable Positive-Dielectrophoretic Cell-Sorting Array," *Analytical Chemistry*, vol. 77, pp. 7976–7983, dec 2005.

[69] J. Voldman, M. L. Gray, M. Toner, and M. A. Schmidt, "A Microfabrication-Based Dynamic Array Cytometer," *Analytical Chemistry*, vol. 74, pp. 3984–3990, aug 2002.

[70] N. Manaresi, G. Medoro, M. Tartagni, L. Altomare, and R. Guerrieri, "At the Interface between Technology and Biology," in *32nd European Solid-State Device Research Conference*, pp. 31–36, IEEE, 2002.

[71] J. B. Beusink, A. M. Lokate, G. A. Besselink, G. J. Pruijn, and R. B. Schasfoort, "Angle-scanning SPR imaging for detection of biomolecular interactions on microarrays," *Biosensors and Bioelectronics*, vol. 23, no. 6, pp. 839–844, 2008.

[72] J. Homola, H. Vaisocherová, J. Dostálek, and M. Piliarik, "Multi-analyte surface plasmon resonance biosensing," *Methods*, vol. 37, no. 1, pp. 26–36, 2005.

[73] R. B. Schasfoort, F. Abali, I. Stojanovic, G. Vidarsson, and L. W. Terstappen, "Trends in SPR cytometry: Advances in label-free detection of cell parameters," *Biosensors*, vol. 8, no. 4, pp. 1–11, 2018.

[74] Y. Ren, Y. Ji, L. Teng, and H. Zhang, "Using Raman spectroscopy and chemometrics to identify the growth phase of Lactobacillus casei Zhang during batch culture at the single-cell level," *Microbial Cell Factories*, vol. 16, no. 1, pp. 1–10, 2017.

[75] S. Casabella, P. Scully, N. Goddard, and P. Gardner, "Automated analysis of single cells using Laser Tweezers Raman Spectroscopy," *The Analyst*, vol. 141, no. 2, pp. 689–696, 2016.

[76] K. Aljakouch, T. Lechtonen, H. K. Yosef, M. K. Hammoud, W. Alsaidi, C. Kötting, C. Mügge, R. Kourist, S. F. El-Mashtoly, and K. Gerwert, "Raman Microspectroscopic Evidence for the Metabolism of a Tyrosine Kinase Inhibitor, Neratinib, in Cancer Cells," *Angewandte Chemie - International Edition*, vol. 57, no. 24, pp. 7250–7254, 2018.

[77] B. Kang, M. M. Afifi, L. A. Austin, and M. A. El-Sayed, "Exploiting the nanoparticle plasmon effect: Observing drug delivery dynamics in single cells via Raman/fluorescence imaging spectroscopy," *ACS Nano*, vol. 7, no. 8, pp. 7420–7427, 2013.

[78] Q. Huang, S. Mao, M. Khan, and J. M. Lin, "Single-cell assay on microfluidic devices," *Analyst*, vol. 144, no. 3, pp. 808–823, 2019.

[79] H. Koo, I. Park, Y. Lee, H. J. Kim, J. H. Jung, J. H. Lee, Y. Kim, J. H. Kim, and J. W. Park, "Visualization and Quantification of MicroRNA in a Single Cell Using Atomic Force Microscopy," *Journal of the American Chemical Society*, vol. 138, no. 36, pp. 11664–11671, 2016.

[80] F. S. Ruggeri, A.-L. Mahul-Mellier, S. Kasas, H. A. Lashuel, G. Longo, and G. Dietler, "Amyloid single-cell cytotoxicity assays by nanomotion detection," *Cell Death Discovery*, vol. 3, no. April, p. 17053, 2017.

[81] O. Guillaume-Gentil, R. V. Grindberg, R. Kooger, L. Dorwling-Carter, V. Martinez, D. Ossola, M. Pilhofer, T. Zambelli, and J. A. Vorholt, "Tunable Single-Cell Extraction for Molecular Analyses," *Cell*, vol. 166, no. 2, pp. 506–516, 2016.

[82] N. Cermak, S. Olcum, F. F. Delgado, S. C. Wasserman, K. R. Payer, M. A. Murakami, S. M. Knudsen, R. J. Kimmerling, M. M. Stevens, Y. Kikuchi, A. Sandikci, M. Ogawa, V. Agache, F. Baléras, D. M. Weinstock, and S. R. Manalis, "High-throughput measurement of single-cell growth rates using serial microfluidic mass sensor arrays," *Nature Biotechnology*, vol. 34, no. 10, pp. 1052–1059, 2016.

[83] M. A. Stockslager, S. Olcum, S. M. Knudsen, R. J. Kimmerling, N. Cermak, K. R. Payer, V. Agache, and S. R. Manalis, "Rapid and high-precision sizing of single particles using parallel suspended microchannel resonator arrays and deconvolution," *Review of Scientific Instruments*, vol. 90, p. 085004, aug 2019.

[84] R. a. Hoffman and W. B. Britt, "Flow-system measurement of cell impedance properties.," *Journal of Histochemistry & Cytochemistry*, vol. 27, pp. 234–240, jan 1979.

[85] R. Pethig and G. H. Markx, "Applications of dielectrophoresis in biotechnology," *Trends in Biotechnology*, vol. 15, no. 10, pp. 426–432, 1997.

[86] U. D. Larsen, G. Blankenstein, and J. Branebjerg, "Microchip coulter particle counter," *International Conference on Solid-State Sensors and Actuators, Proceedings*, vol. 2, pp. 1319–1322, 1997.

[87] K. C. Cheung, M. D. Berardino, G. Schade-Kampmann, M. Hebeisen, A. Pierzchalski, J. Bocsi, A. Mittag, and A. Tárnok, "Microfluidic impedance-based flow cytometry," *Cytometry Part A*, vol. 77, no. 7, pp. 648–666, 2010.

[88] S.-I. Han, Y.-D. Joo, and K.-H. Han, "An electrorotation technique for measuring the dielectric properties of cells with simultaneous use of negative quadrupolar dielectrophoresis and electrorotation," *The Analyst*, vol. 138, no. 5, p. 1529, 2013.

[89] Y. Huang, X.-B. Wang, R. Holzel, F. F. Becker, and P. R. C. Gascoyne, "Electrorotational studies of the cytoplasmic dielectric properties of Friend murine erythroleukaemia cells," *Physics in Medicine and Biology*, vol. 40, no. 11, pp. 1789–1806, 1995.

[90] P. Gascoyne, F. Becker, and X.-B. Wang, "Numerical analysis of the influence of experimental conditions on the accuracy of dielectric parameters derived from electrorotation measurements," *Bioelectrochemistry and Bioenergetics*, vol. 36, pp. 115–125, mar 1995.

[91] M. Schaeper, R. Schmidt, R. Kostbade, N. Damaschke, and J. Gimsa, "Optical high-resolution analysis of rotational movement: testing circular spatial filter velocimetry (CSFV) with rotating biological cells," *Journal of Physics D: Applied Physics*, vol. 49, no. 26, p. 265402, 2016.

[92] C. I. Trainito, O. Français, and B. Le Pioufle, "Monitoring the permeabilization of a single cell in a microfluidic device, through the estimation of its dielectric properties based on combined dielectrophoresis and electrorotation in situ experiments," *Electrophoresis*, vol. 36, no. 9-10, pp. 1115–1122, 2015.

[93] M. Cristofanilli, G. De Gasperis, L. Zhang, M. C. Hung, P. R. Gascoyne, and G. N. Hortobagyi, "Automated electrorotation to reveal dielectric variations related to HER-2/neu overexpression in MCF-7 sublines," *Clinical Cancer Research*, vol. 8, no. 2, pp. 615–619, 2002.

[94] A. Rohani, W. Varhue, Y.-H. Su, and N. S. Swami, "Electrical tweezer for highly parallelized electrorotation measurements over a wide frequency bandwidth," *ELECTROPHORESIS*, vol. 35, pp. 1795–1802, jul 2014.

[95] A. El Hasni, C. Schmitz, K. Bui-Göbbels, P. Bräunig, W. Jahnen-Dechent, and U. Schnakenberg, "Electrical impedance spectroscopy of single cells in hydrodynamic traps," *Sensors and Actuators, B: Chemical*, vol. 248, pp. 419–429, 2017.

[96] L. S. Jang and M. H. Wang, "Microfluidic device for cell capture and impedance measurement," *Biomedical Microdevices*, vol. 9, no. 5, pp. 737–743, 2007.

[97] S. Z. Hua and T. Pennell, "A microfluidic chip for real-time studies of the volume of single cells," *Lab on a Chip*, vol. 9, no. 2, pp. 251–256, 2009.

[98] D. Malleo, J. T. Nevill, L. P. Lee, and H. Morgan, "Continuous differential impedance spectroscopy of single cells," *Microfluidics and Nanofluidics*, vol. 9, no. 2-3, pp. 191–198, 2010.

[99] Z. Zhu, O. Frey, F. Franke, N. Haandbæk, and A. Hierlemann, "Real-time monitoring of immobilized single yeast cells through multifrequency electrical impedance spectroscopy," *Analytical and Bioanalytical Chemistry*, vol. 406, no. 27, pp. 7015–7025, 2014.

[100] Z. Zhu, O. Frey, N. Haandbaek, F. Franke, F. Rudolf, and A. Hierlemann, "Time-lapse electrical impedance spectroscopy for monitoring the cell cycle of single immobilized S. pombe cells," *Scientific Reports*, vol. 5, no. October, pp. 1–14, 2015.

[101] Y. Zhou, S. Basu, E. Laue, and A. A. Seshia, "Single cell studies of mouse embryonic stem cell (mESC) differentiation by electrical impedance measurements in a microfluidic device," *Biosensors and Bioelectronics*, vol. 81, pp. 249–258, 2016.

[102] F. David, M. Hebeisen, G. Schade, E. Franco-Lara, and M. Di Berardino, "Viability and membrane potential analysis of Bacillus megaterium cells by impedance flow cytometry," *Biotechnology and Bioengineering*, vol. 109, no. 2, pp. 483–492, 2012.

[103] G. Mernier, N. Piacentini, R. Tornay, N. Buffi, and P. Renaud, "Cell viability assessment by flow cytometry using yeast as cell model," *Sensors and Actuators, B: Chemical*, vol. 154, no. 2, pp. 160–163, 2011.

[104] R. Sharma, T. Blackburn, W. Hu, K. Wiltberger, and O. D. Velev, "On-chip microelectrode impedance analysis of mammalian cell viability during biomanufacturing," *Biomicrofluidics*, vol. 8, no. 5, 2014.

[105] J. Kirkegaard, C. H. Clausen, R. Rodriguez-Trujillo, and W. E. Svendsen, "Study of paclitaxel-treated HeLa cells by differential electrical impedance flow cytometry," *Biosensors*, vol. 4, no. 3, pp. 257–272, 2014.

[106] C. Küttel, E. Nascimento, N. Demierre, T. Silva, T. Braschler, P. Renaud, and A. G. Oliva, "Label-free detection of Babesia bovis infected red blood cells using impedance spectroscopy on a microfabricated flow cytometer," *Acta Tropica*, vol. 102, no. 1, pp. 63–68, 2007.

[107] K. Solly, X. Wang, X. Xu, B. Strulovici, and W. Zheng, "Application of real-time cell electronic sensing (RT-CES) technology to cell-based assays," *Assay and Drug Development Technologies*, vol. 2, no. 4, pp. 363–372, 2004.

[108] J. Z. Xing, L. Zhu, J. A. Jackson, S. Gabos, X. J. Sun, X. B. Wang, and X. Xu, "Dynamic monitoring of cytotoxicity on microelectronic sensors," *Chemical Research in Toxicology*, vol. 18, no. 2, pp. 154–161, 2005.

[109] H. Morgan, T. Sun, D. Holmes, S. Gawad, and N. G. Green, "Single cell dielectric spectroscopy," *J. Phys. D: Appl. Phys*, vol. 40, pp. 61–70, 2007.

[110] K. Cheung, S. Gawad, and P. Renaud, "Impedance spectroscopy flow cytometry: On-chip label-free cell differentiation," *Cytometry Part A*, vol. 65, no. 2, pp. 124–132, 2005.

[111] L. Wu, L. Y. Lanry Yung, and K. M. Lim, "Dielectrophoretic capture voltage spectrum for measurement of dielectric properties and separation of cancer cells," *Biomicrofluidics*, vol. 6, no. 1, pp. 1–10, 2012.

[112] D. M. Vykoukal, P. R. C. Gascoyne, and J. Vykoukal, "Dielectric characterization of complete mononuclear and polymorphonuclear blood cell subpopulations for label-free discrimination.," *Integrative biology : quantitative biosciences from nano to macro*, vol. 1, no. 7, pp. 477–84, 2009.

[113] L. M. Broche, F. H. Labeed, and M. P. Hughes, "Extraction of dielectric properties of multiple populations from dielectrophoretic collection spectrum data.," *Physics in medicine and biology*, vol. 50, no. 10, pp. 2267–74, 2005.

[114] A. Rohani, J. H. Moore, Y. H. Su, V. Stagnaro, C. Warren, and N. S. Swami, "Single-cell electro-phenotyping for rapid assessment of Clostridium difficile heterogeneity under vancomycin treatment at sub-MIC (minimum inhibitory concentration) levels," *Sensors and Actuators, B: Chemical*, vol. 276, no. August, pp. 472–480, 2018.

[115] H. A. Pohl and J. S. Crane, "Dielectrophoresis of cells.," *Biophysical journal*, vol. 11, no. 9, pp. 711–27, 1971.

[116] H. A. Pohl, K. Pollock, and J. S. Crane, "Dielectrophoretic force: A comparison of theory and experiment," *Journal of Biological Physics*, vol. 6, no. 3-4, pp. 133–160, 1978.

[117] Y. Zheng, J. Nguyen, Y. Wei, and Y. Sun, "Recent advances in microfluidic techniques for single-cell biophysical characterization," *Lab on a Chip*, vol. 13, no. 13, p. 2464, 2013.

[118] X.-B. Wang, Y. Huang, P. R. Gascoyne, F. F. Becker, R. Hölzel, and R. Pethig, "Changes in Friend murine erythroleukaemia cell membranes during induced differentiation determined by electrorotation," *Biochimica et Biophysica Acta (BBA) - Biomembranes*, vol. 1193, pp. 330–344, aug 1994.

[119] Y. Huang, X.-B. Wang, P. R. Gascoyne, and F. F. Becker, "Membrane dielectric responses of human T-lymphocytes following mitogenic stimulation," *Biochimica et Biophysica Acta (BBA) - Biomembranes*, vol. 1417, pp. 51–62, feb 1999.

[120] X. Wang, F. F. Becker, and P. R. C. Gascoyne, "Membrane dielectric changes indicate induced apoptosis in HL-60 cells more sensitively than surface phosphatidylserine expression or DNA fragmentation," *Biochimica et Biophysica Acta - Biomembranes*, vol. 1564, no. 2, pp. 412–420, 2002.

[121] Y. Huang, X.-B. Wang, F. F. Becker, and P. R. Gascoyne, "Membrane changes associated with the temperature-sensitive P85gag-mos-dependent transformation of rat kidney cells as determined by dielectrophoresis and electrorotation," *Biochimica et Biophysica Acta (BBA) - Biomembranes*, vol. 1282, pp. 76–84, jun 1996.

[122] Y. Huang, X.-B. Wang, R. Holzel, F. F. Becker, and P. R. C. Gascoyne, "Electrorotational studies of the cytoplasmic dielectric properties of Friend murine erythroleukaemia cells," *Physics in Medicine and Biology*, vol. 40, pp. 1789–1806, nov 1995.

[123] G. D. Gasperis, X. Wang, J. Yang, F. F. Becker, and P. R. C. Gascoyne, "Automated electrorotation: dielectric characterization of living cells by real-time motion estimation," *Measurement Science and Technology*, vol. 9, pp. 518–529, mar 1998.

[124] C. Reichle, T. Schnelle, T. Müller, T. Leya, and G. Fuhr, "A new microsystem for automated electrorotation measurements using laser tweezers," *Biochimica et Biophysica Acta (BBA) - Bioenergetics*, vol. 1459, pp. 218–229, jul 2000.

[125] M. P. Hughes, "Computer-aided analysis of conditions for optimizing practical electrorotation," *Physics in Medicine and Biology*, vol. 43, no. 12, pp. 3639–3648, 1998.

[126] C. Reichle, T. Müller, T. Schnelle, and G. Fuhr, "Electro-rotation in octopole micro cages," *Journal of Physics D: Applied Physics*, vol. 32, no. 16, pp. 2128–2135, 1999.

[127] C. F. Gonzalez and V. T. Remcho, "Harnessing dielectric forces for separations of cells, fine particles and macromolecules," *Journal of Chromatography A*, vol. 1079, no. 1-2 SPEC. ISS., pp. 59–68, 2005.

[128] A. Rohani, B. J. Sanghavi, A. Salahi, K. T. Liao, C. F. Chou, and N. S. Swami, "Frequency-selective electrokinetic enrichment of biomolecules in physiological media based on electrical double-layer polarization," *Nanoscale*, vol. 9, no. 33, pp. 12124–12131, 2017.

[129] J. H. Moore, W. B. Varhue, Y.-H. Su, S. S. Linton, V. Farmehini, T. E. Fox, G. L. Matters, M. Kester, and N. S. Swami, "Conductance-Based Biophysical Distinction and Microfluidic Enrichment of Nanovesicles Derived from Pancreatic Tumor Cells of Varying Invasiveness," *Analytical Chemistry*, vol. 91, pp. 10424–10431, aug 2019.

[130] J. Cottet, A. Kehren, S. Lasli, H. van Lintel, F. Buret, M. Frénéa-Robin, and P. Renaud, "Dielectrophoresis-assisted creation of cell aggregates under flow conditions using planar electrodes," *Electrophoresis*, vol. 40, no. 10, pp. 1498–1509, 2019.

[131] V. Calero, P. Garcia-Sanchez, C. M. Fernandes Honrado, A. Ramos, and H. Morgan, "AC electrokinetic biased Deterministic Lateral Displacement for tunable particle separation," *Lab on a Chip*, 2019.

[132] R. Martinez-Duarte, "Microfabrication technologies in dielectrophoresis applications-A review," *Electrophoresis*, vol. 33, no. 21, pp. 3110–3132, 2012.

[133] J. Voldman, M. Toner, M. L. Gray, and M. A. Schmidt, "Design and analysis of extruded quadrupolar dielectrophoretic traps," *Journal of Electrostatics*, vol. 57, no. 1, pp. 69–90, 2003.

[134] L. Wang, L. Flanagan, and A. P. Lee, "Side-wall vertical electrodes for lateral field microfluidic applications," *Journal of Microelectromechanical Systems*, vol. 16, no. 2, pp. 454–461, 2007.

[135] Chunlei Wang, Guangyao Jia, L. Taherabadi, and M. Madou, "A novel method for the fabrication of high-aspect ratio C-MEMS structures," *Journal of Microelectromechanical Systems*, vol. 14, pp. 348–358, apr 2005.

[136] S. Rajaraman, S. O. Choi, R. H. Shafer, J. D. Ross, J. Vukasinovic, Y. Choi, S. P. Deweerth, A. Glezer, and M. G. Allen, "Microfabrication technologies for a coupled three-dimensional microelectrode, microfluidic array," *Journal of Micromechanics and Microengineering*, vol. 17, no. 1, pp. 163–171, 2007.

[137] J.-W. Choi, S. Rosset, M. Niklaus, J. R. Adleman, H. Shea, and D. Psaltis, "3-Dimensional Electrode Patterning Within a Microfluidic Channel Using Metal Ion Implantation," *Lab on a Chip*, vol. 10, no. 6, p. 783, 2010.

[138] J. Xu, D. Wu, Y. Hanada, C. Chen, S. Wu, Y. Cheng, K. Sugioka, and K. Midorikawa, "Electrofluidics fabricated by space-selective metallization in glass microfluidic structures using femtosecond laser direct writing," *Lab on a Chip*, vol. 13, no. 23, p. 4608, 2013.

[139] S. C. Kilchenmann, E. Rollo, E. Bianchi, and C. Guiducci, "Metal-coated silicon micropillars for freestanding 3D-electrode arrays in microchannels," *Sensors and Actuators B: Chemical*, vol. 185, pp. 713–719, aug 2013.

[140] I. Doh and Y.-H. Cho, "A continuous cell separation chip using hydrodynamic dielectrophoresis (DEP) process," *Sensors and Actuators A: Physical*, vol. 121, pp. 59–65, may 2005.

[141] H. A. Pohl, "The motion and precipitation of suspensoids in divergent electric fields," *Journal of Applied Physics*, vol. 22, no. 7, pp. 869–871, 1951.

[142] R. Pethig, *Dielectrophoresis*. Chichester, UK: John Wiley & Sons, Ltd, apr 2017.

[143] T. B. Jones, *Electromechanics of Particles*. Cambridge: Cambridge University Press, 1995.

[144] H. Fricke and H. J. Curtis, "The determination of surface conductance from measurements on suspensions of spherical particles," *Journal of Physical Chemistry*, vol. 40, no. 6, pp. 715–722, 1936.

[145] G. Schwarz, "A theory of the low-frequency dielectric dispersion of colloidal particles in electrolyte solution," *Journal of Physical Chemistry*, vol. 66, no. 12, pp. 2636–2642, 1962.

[146] M. P. Hughes, *Nanoelectromechanics in engineering and biology*. CRC Press LLC, 2002.

[147] J. Voldman, "Dielectrophoretic Traps for Cell Manipulation," in *BioMEMS and Biomedical Nanotechnology*, pp. 159–186, Boston, MA: Springer US, 2006.

[148] H. Li, Y. Zheng, D. Akin, and R. Bashir, "Characterization and modeling of a microfluidic dielectrophoresis filter for biological species," *Journal of Microelectromechanical Systems*, vol. 14, no. 1, pp. 103–112, 2005.

[149] M. A. Comino, "Arrays of 3D microelectrodes for single-cell trapping and electrorotation," tech. rep., Politecnico di Torino, 2016.

[150] K. Keim, A. Gonçalves, and C. Guiducci, "Trapping of Single-Cells Within 3D Electrokinetic Cages," in *Proceedings of the 2018 COMSOL Conference in Lausanne*, (Lausanne), 2018.

[151] K. Keim, M. Z. Rashed, S. C. Kilchenmann, A. Delattre, A. F. Gonçalves, P. Éry, and C. Guiducci, "On-chip technology for single-cell arraying, electrorotation-based analysis and selective release," *ELECTROPHORESIS*, vol. 40, p. elps.201900097, jun 2019.

[152] K. Keim, P. Maoddi, S. Kilchenmann, M. Comino, and C. Guiduccci, "Lab-on-a-Chip Platform for Single-Cell Electrorotation Using 3D Electrodes," in *21st International Conference on Miniaturized Systems for Chemistry and Life Sciences*, (Savannah, Georgia, USA), pp. 932–934, 2017.

[153] K. Keim, P. Éry, A. Delattre, and C. Guiducci, "3D electrode arrays for trapping, analysis and selectrive release of single cells using DEP," in *22rd International Conference on Miniaturized Systems for Chemistry and Life Sciences*, pp. 2394–2397, 2018.

[154] T. B. Jones, "Basic Theory of Dielectrophoresis and Electrorotation," *IEE Engineering in Medicine and Biology Magazine*, no. December, pp. 33–42, 2003.

[155] U. Lei, C. Y. Yang, and K. C. Wu, "Viscous torque on a sphere under arbitrary rotation," *Applied Physics Letters*, vol. 89, no. 18, pp. 1–4, 2006.

[156] K. Keim, M. Z. Rashed, and C. Guiducci, "OBSERVATION OF MEMBRANE CHANGES AND VIABILITY OF CELLS IN A PARALLEL ELECTROROTATION PLATFORM," in *23rd International Conference on Miniaturized Systems for Chemistry and Life Sciences*, no. October, (Basel), pp. 1011–1013, 2019.

[157] J. P. Beech, K. Keim, B. D. Ho, C. Guiducci, and J. O. Tegenfeldt, "Active Posts in Deterministic Lateral Displacement Devices," *Advanced Materials Technologies*, vol. 4, p. 1900339, sep 2019.

[158] J. Cummings, P. S. Aisen, B. Dubois, L. Frölich, C. R. Jack, R. W. Jones, J. C. Morris, J. Raskin, S. A. Dowsett, and P. Scheltens, "Drug development in Alzheimer's disease: The path to 2025," *Alzheimer's Research and Therapy*, vol. 8, no. 1, pp. 1–12, 2016.

[159] J. Hardy and D. J. Selkoe, "The amyloid hypothesis of Alzheimer's disease: Progress and problems on the road to therapeutics," *Science*, vol. 297, no. 5580, pp. 353–356, 2002.

[160] I. Benilova, E. Karran, and B. De Strooper, "The toxic Aβ oligomer and Alzheimer's disease: an emperor in need of clothes," *Nature Neuroscience*, vol. 15, pp. 349–357, mar 2012.

Kevin Keim

Date of birth: 14.12.1989 (Heppenheim, Germany)
Telephone: +41 78 686 56 55
Email: kevin.keim@gmx.de

Research contributions and affiliations

Since 09/2016 — Doctoral Assistant, **École Polytechnique Fédérale de Lausanne, Switzerland; Laboratory of Life Sciences Electronics**

-Based on finite elements simulations, I designed, fabricated and investigated a parallelized system for single-cell analysis on my own cell cultures. Using advanced instrumentation control, I invented and realized a mechanism for in flow elecrorotation and selective single-cell trapping and release.

-In our laboratory, I am responsible for the IT management. I directly supervised six students in bachelor and master careers. I am in charge of the ordinary coordination of our collaborations with the Tegenfeldt lab (Lund University) and the Flanagan lab (University of California, Irvine).

-I created and organized the exercise session for the course EE295 "Systèmes électriques et électroniques I". During the semester I teach a class of up to 30 students.

02/2019 – 04/2019 — Visiting PhD Student, **Massachusetts General Hospital / Harvard Medical School, Boston USA**
Prof. Mehmet Toners lab

-Established and improved an experimental protocol for cluster destroyer experiments.

11/2014 – 11/2015 — Master Thesis, **Technical University of Munich, Germany, Department of Electrical Engineering, Chair for Molecular Electronics**

-Starting from the drawing table, I developed a fabrication process for nano gaps to measure lateral electric current through self-assembled monolayers.

06/2013 – 09/2013 — Bachelor Thesis, **École Polytechnique fédérale de Lausanne, Switzerland Laboratory of Semiconductor Materials**

-Fabricated and investigated magnetic nanotube devices in liquid helium.

10/2011 — Internship, **Daimler AG, Mannheim,**
Competence Center for Emission-free Mobility

Academic education

01/2018 – 09/2020 — MBA program, **Collège des Ingénieurs, Paris, Munich, Turin**

09/2016 – 03/2020 — Ph.D. program in Microsystems and Microelectronics, **École Polytechnique Fédérale de Lausanne, Switzerland**

10/2013 – 06/2016 — M.Sc. Physics, **Technical University of Munich, Germany**

- Overall average grade: 1.5 (best possible grade 1.0)

2016 — Semester abroad, **Nanyang Technological University, Singapore**

10/2010 – 09/2013 — B.Sc. Physics, **Technical University of Munich, Germany**

- Overall average grade: 1.8 (best possible grade 1.0)

2012	Semester abroad, **École Polytechnique, Paris, France**
08/2000 – 06/2009	Abitur, **Altes Kurfürstliches Gymnasium, Bensheim, Germany** • Overall average grade: 1.4 (best possible grade 1.0)
08/2006 – 06/2007	Diploma, **Fountain Lake High School, Hot Springs, AR, USA**

Publications

Journal papers

"On-chip technology for single-cell arraying, electrorotation-based analysis and selective release", K. Keim, M. Z. Rashed, S. C. Kilchenmann, A. Delattre, A. Gonçalves, P. Éry, C. Guiducci; Electrophoresis, vol. 40, no.14, pp. 1830-1838, 2019

"Active Posts in Deterministic Lateral Displacement Devices";
J. P. Beech, K. Keim, B. D. Ho, C. Guiducci, J. O. Tegenfeldt; Advanced Materials Technologies, vol. 4, p.1900339, 2019

"Selective Retrieval of Individual Cells from Microfluidic Arrays Combining Dielectrophoretic Force and Directed Hydrodynamic Flow", P.-E. Thiriet, J. Pezoldt, G. Gambardella, K. Keim, B. Deplancke, C. Guiducci; micromachines, vol. 11, no. 3, p. 322, 2020

"In-flow measurement of cell-cell adhesion using oscillatory inertial microfluidics", B. R. Mutlu, T. Dubash, C. Dietsche, A. Mishra, A. Ozbey, K. Keim, J. Edd, D. Haber, S. Maheswaran, M. Toner; Lab on a Chip (submitted)

Conference proceedings

"Observation of membrane changes and viability of cells in a parallelized electrorotation platform";
K. Keim, M. Z. Rashed, C. Guiducci; MicroTAS, Basel, Switzerland, 2019

"Parallel electrorotation and cell handling in individual dielectric micro cages";
K. Keim, M. Z. Rashed, C. Guiducci; MicroTAS, Basel, Switzerland, 2019

"The separation of nano-sized particles in micro-scale post arrays";
J. P. Beech, K. Keim, B. D. Ho, C. Guiducci, J. O. Tegenfeldt; MicroTAS, Basel, Switzerland, 2019

„Biophysics of Circulating Tumor Cell Clusters",
B. R. Mutlu, T. Dubash, C. Dietsche, A. Mishra, K. Keim, J. Edd, D. Haber, S. Maheswaran, M. Toner; MicroTAS, Basel, Switzerland, 2019

"Arrayed label-free single-cell analysis in flow by electrorotation";
K. Keim, P. Éry, A. Delattre, A. Gonçalves, C. Guiducci; EMBS MNMC, Kauai, USA, 2018

"3D electrode arrays for trapping, analysis and selective release of single cells using DEP";
K. Keim, P. Éry, A. Delattre, C. Guiducci; MicroTAS, Kaohsiung, Taiwan, 2018

"Tunable separation and DNA manipulation in metal coated pillar arrays";
J. P. Beech, K. Keim, B. D. Ho, O. Ström, C. Guiducci, J. O. Tegenfeldt; MicroTAS, Kaohsiung, Taiwan, 2018

"Analysis of cell trapping within dielectrophoretic traps, build out of 3D electrodes";
K. Keim, A. Gonçalves, C. Guiducci; COMSOL Conference, Lausanne, Switzerland, 2018

"Lab-on-a-Chip Platform for Single-Cell Electrorotation Using 3D Electrodes";
K. Keim, P. Maoddi, S. Kilchenmann, M. Comino, C. Guiducci; MicroTAS, Savannah, USA, 2017

"A nanogap electrode platform for organic monolayer-film devices";
S. Pfaehler, K. Keim, R. Csiki, Q. Nguyen, K.-C. Liao, M. Stutzmann, J. Schwartz, A. Cattani-Scholz, M. Tornow; IEEE Nano, Sendai, Japan, 2016, pp. 842-844

"Horizontal γ-PNA immobilization through organophosphonate interfacial chemistry";
A. De, K. Keim, A. Cattani-Scholz, M. Tornow; IEEE Nano, Rome, Italy, 2015, pp. 1568-1571

Conference abstracts

"Simultaneous use of metal coated three-dimensional SU-8 pillars as passive posts and electrodes";
K. Keim, M. Z. Rashed, J. P. Beech, W. Lahbichi, T. Ryser, G. Porro, P. Thiriet, J. Tegenfeldt, C. Guiducci; Dielectrophoresis, Flagstaff AK, USA, 2020 (accepted)

"Electrorotation for single cell analysis of membrane damage induced by toxins mimicking the neurodegenerative effect of amyloid beta in the Alzheimer's disease";
T. Ryser, K. Keim, M. Z. Rashed, W. Lahbichi, A.-L. Mahul-Mellier, H. Lashuel, C. Guiducci; Dielectrophoresis, Flagstaff AK, USA, 2020 (accepted)

"Deterministic lateral displacement platforms, composed of arrayed three-dimensional electrodes for tunable particle sorting";
G. Porro , K. Keim, G. Cappai, J. P. Beech, J. O. Tegenfeldt, C. Guiducci; Dielectrophoresis, Flagstaff AK, USA, 2020 (accepted)

"Selective DEP-based retrieval of single cells from microfluidic arrays and analysis of their transcriptome";
G P.-E. Thiriet, J. Pezoldt, G. Gambardella, K. Keim, B. Deplancke, C. Guiducci; Dielectrophoresis, Flagstaff AK, USA, 2020 (accepted)

"Parallelized Electrorotation in single cell DEP micro cages";
K. Keim, M. Z. Rashed, C. Guiducci; 13th Symposium on Electrokinetics (ELKIN), Boston, USA, 2019

"Arrayed label-free single-cell analysis by electrorotation";
K. Keim, P. Éry, A. Delattre, C. Guiducci; EMBS MNMC, Kauai, USA, 2018

"Integrated 3-D Electrodes for Selective Cell Release in Hydrodynamic Traps";
P.-E. Thiriet, K. Keim, C. Guiducci; EMBS MNMC, Kauai, USA, 2018

"Single-cell sized electrokinetic 3D structures in microfluidic chambers";
K. Keim, J. Beech, P. Thiriet, B. Ho, J. Tegenfeldt, C. Guiducci; Dielectrophoresis, Surrey, UK, 2018

Scholarships and prizes

2018	Best Poster Award Institute of Physics Dielectrophoresis 2018 conference, Surrey, UK
2017	Best Poster Award at Nano & Micro Systems 11th international school, Freiburg, D
2017	Winner of the "Picture of the Month" concours (February), CMi, EPFL
2013 – 2016	Member of the TUM Junge Akademie (top 3% of TUM students)
2016	Prize for Engagement for Student at the TUM Physics Department
2010 – 2015	Scholarship of the Konrad-Adenauer-Stiftung (300 € per month)
2014	Explained a Citron battery to Children on TV (CheXperiment, ARD & ZDF)

Extracurricular activities

Since 2018	Pre-selecting scholars for the Konrad-Adenauer-Stiftung based on resumes
2017 – 2019	Vice-President and treasurer of the Consulting Society at EPFL (Organization of case study trainings for students and establishing contacts to consulting companies for workshops)
2013 – 2015	Voting member of the Physics Department Faculty Council (TUM)
2011 – 2015	Mentor for international students (TUM)
2011 – 2015	Physics student representative (TUM)
2014	"TUM Campus Run" organization team member (Organized a sport event with 200 participants)

Lausanne, March 22nd, 2020